Path-line Oriented Visualization of Dynamical Flow Fields

Kuangyu Shi

Max-Planck-Institut für Informatik
Saarbrücken, Germany

Dissertation zur Erlangung des Grades
Doktor der Ingenieurwissenschaften (Dr.-Ing)
der Naturwissenschaftlich-Technischen Fakultät I
der Universität des Saarlandes

Eingereicht am 27. Juni 2008 in Saarbrücken durch

Kuangyu Shi
MPI Informatik
Campus E1 4
66 123 Saarbrücken

skyshi@mpi-sb.mpg.de

Betreuender Hochschullehrer – Supervisor
Prof. Dr. Hans-Peter Seidel, Max-Planck-Institut für Informatik, Germany

Gutachter – Reviewers
Prof. Dr. Holger Theisel, Otto-von-Guericke-Universität Magdeburg, Germany
Prof. Dr. Hans-Peter Seidel, Max-Planck-Institut für Informatik, Germany

Wissenschaftlicher Begleiter – Scientific Tutor
Prof. Dr. Joachim Weickert, Universität des Saarlandes, Saarbrücken, Germany

Dekan – Dean
Prof. Dr. Joachim Weickert, Universität des Saarlandes, Saarbrücken, Germany

Datum des Kolloquiums – Date of Defense
10. Dezember 2008 – December 10th, 2008

Abstract

An effective visual representation of dynamical flow behavior is still a challenging problem of modern flow visualization. Path-lines are important characteristic curves of dynamical flow fields. In this thesis, we focus on the visual analysis of path-line behaviors and uncover the dynamical nature of a flow field. We propose a topological segmentation of periodic 2D time-dependent vector fields based on asymptotic path-line behaviors. A flow domain is classified into different areas based on the converging or diverging path-line behaviors relating to the identified critical path-lines. We also offer an alternative algorithm to extract the separation surfaces of the path-line oriented topological structure. For the interactive visual analysis of fluid motion, we propose an information visualization based approach to explore the dynamical flow behaviors. Attributes associated with path-lines are identified and analyzed and the interesting features or structures are extracted and visualized with human interaction. We also investigate the property transport phenomenon and propose an approach to visualize the finite-time transport structures of property advection which is similar to carry out a line integral convolution over physical properties along path-lines. We demonstrate our approaches on a number of applications and present some interesting results.

Acknowledgements

I always feel lucky to carry out my PhD study in Max-Planck Institute für Informatik. It is really an ideal research place with plenty of active genius researchers and scholars. The friendly, charming and harmonic international atmosphere here impressed me so deeply. At the end of my PhD study, it is obligated for me to write down my grateful feeling from my heart.

I would like to express my deepest gratitude to my advisor Prof. Dr. Holger Theisel for his careful and patient supervision. I really appreciate his trust and encouragements, which gave me strength and faith to further my scientific journey. I also want to thank Prof. Dr. Hans-Peter Seidel for his constant supports during my study.

Special appreciation should be given to Dr. Tino Weinkauf and Prof. Dr. Helwig Hauser. Their warm heart and clever suggestions helped me a lot for my research.

Many special thanks is further given to all the colleagues in our department. It is a creative team with fruitful discussions and always inspiring valuable thoughts and new ideas. Particularly, I am grateful to Ms. Sabine Budde and Ms. Conny Liegl, who helped me a lot and gave me a family-like feeling thousands miles away from my hometown.

I would like also to thank all friends here for their friendship which have colored my life in Saarbrücken tremendously. In particular, I wish to thank Zhao Dong and Tongbo Chen for their kind help on my works.

Finally, I am so grateful to my wife Bing Zhu, her love is always the backbone of my life. I feel also indebted to my little daughter Yifan Shi. She is the most beautiful present to my life though I wasn't able to stay with her most of the time during this work. I must thank my mother-in-law who takes care of Yifan carefully for us. I am also grateful to my parents for their selfless love and support.

Saarbrücken, June. 26th, 2008
Kuangyu Shi

Contents

Chapter 1

Introduction

The insight into a complex physical phenomenon is always improved if a pattern produced by or related to this phenomenon can be observed by visual inspection. Insights from different viewpoints present different information, thus contribute different understandings of the complex phenomenon. In fluid analysis, it is critically important to see the patterns underlying a flow process. With the development of flow visualization technologies, new features and patterns become visible which significantly expands the vision to the complex fluid phenomenon.

Flow visualization is an important subfield of scientific visualization. Many promising techniques have been developed recently to illustrate a flowing fluid phenomenon. However, when dealing with a dynamical flow fields, the increasing size, complexity as well as the dimensionality of the underlying space-time domain makes the analysis and the visual representation challenging and partially unsolved. In particular, it has still proved to be inherently difficult to actually comprehend the important characteristics of the time-dependent fluid flow process. An effective visual analysis of dynamical flow field is still a challenging problem in scientific visualization.

Path-lines are important characteristic curves of dynamical flow fields which naturally describe the paths of fluid elements over time in the flow. Hence, the analysis of the dynamic behavior of flow fields is strongly related to the analysis of the behavior of the path-lines. Path-line oriented features or patterns deliver significant different information from classical methods and contribute a new and deep understanding of the dynamic nature of unsteady flow phenomenon.

In this thesis, we focus on the visualization of dynamical flow fields and present

a set of path-line oriented flow visualization algorithms to visually explore the dynamical behavior of a flow process. We try to integrate our works into the framework of classical fluid analysis and organize this thesis in the follow structure:

Chapter 2 recalls the background of general fluid analysis and discusses some common concepts of fluid phenomena, which are used throughout this thesis. The methodologies of fluid analysis and their relations are also discussed.

Chapter 3 goes through the well-applied flow visualization techniques from the viewpoints of fluid analysis. Special attention is payed on the visualization techniques for dynamical flow field are especially .

Chapter 4 presents a work of path-line oriented topology based on the assumption of periodic 2D time-dependent vector fields. The topological structures of asymptotic behavior of path-lines is introduced. The further solution of separation surface extraction is also discussed. These works have been published in [STW*06, STW*07].

Chapter 5 introduces an information visualization based algorithm to visually analyze path-line behaviors. A number of local and global attributes of path-lines are discussed and analyzed by the state-of-the-art information visualization approaches in the sense of a set of linked views. The interactive exploration of intricate 4D flow structures is proposed. This work has been published in [STH*07].

Chapter 6 investigates the fluid transport phenomenon and proposes an approach to visualize the finite-time transport structures through applying a transport filter on correlated physical property fields. For advection behavior, the transport filter is equivalent to a path-line integral convolution. The transport structures for fluid advection is visualized through applying the advection filter, i. e. convoluting the property field along path-lines. This work has been published in [STW*08a, STW*08b].

Chapter 7 draws conclusions and discusses the future works of the path-line oriented flow visualization techniques.

Chapter 2

Background of Fluid Analysis

Fluid analysis is an classical field of scientific and engineering research. It covers a rich variety of applications such as in automotive industry, aerodynamics, turbomachinery design, weather simulation, climate modeling or medical applications. With the experimental support, theoretical fluid analysis has achieved enormous success during last centuries. Meanwhile, the experimental methodology has also been improved significantly.

With the evolving of computer technology, the fluid analysis is no longer restricted to thinking and experiments. Computational fluid dynamics (CFD) has extended the abilities of scientists and engineers by creating simulations of dynamic behavior of fluid flows under a wide range of conditions. The result of this analysis is usually a 2D or 3D grid of data, which may be uniformly or non-uniformly spaced. The goal is then to analyze this flow data field to identify features such as topologies, vortices, turbulence, and other forms of structure. Computer aided flow visualization is a highlight in fluid analysis which has equipped the fluid analysts with extra powerful eyes, especially when dealing with the simulated data. The insights into complex fluid phenomena have become deeper and deeper.

2.1 Fluid Description

Theoretical fluid analysis has been one of the major topics of physics, applied mathematics and engineering over the last hundred years. Starting with the explanations of aerofoil theory, the study of fluids continues today with looking at

how internal and surface waves, shock waves, turbulent fluid flow and the occurrence of chaos can be described mathematically. At the same time, it is critically important for engineers to understand fluid phenomena properly. However it is not always easy to comprehend these complex phenomena. There are many terms and mathematical methods which are different from normal physics. Although the basic concepts of velocity, mass, linear momentum, forces, etc., are the ground elements, the slippery nature of fluids means that applying those basic concepts sometimes may be special. So for the accurate analysis of a fluid behavior, it is necessary to have a precise description. Some of this will be discussed here.

2.1.1 Flow properties

In order to describe fluid flows, we need to be able to deal with characteristic fluid properties which are different at different locations and times [Oer02]. Mathematically it is modeled with variables that describe the physical state of a fluid usually as functions of spatial-temporal position. The mathematical model built in fluid dynamics is based on the *continuum hypothesis*: in a spatial-temporal domain $D \subset \mathbb{R}^3 \times \mathbb{R}$, fluid properties assigned to any spatial-temporal position $(\mathbf{x},t)$ vary continuously and may be taken as constant across sufficiently small volumes. The continuum hypothesis implies that fluid properties are differentiable and fluid dynamics can be formulated as a classical field theory. The fluid properties are represented in either scalar-valued or vector-valued fields.

- *Density* of a fluid is the amount of mass per unit volume. For a given position $\mathbf{x}$ and t, it can be defined as

$$\rho(\mathbf{x},t) = \lim_{\Delta V \to 0} \frac{\Delta m}{\Delta V}$$

  where Δm is the mass of the small volume ΔV.

- *Velocity* of a fluid is a vector which specifies the flow motion for a fluid element at a given point $\mathbf{x}$ and time t. The main task of fluid dynamics is to identify the fluid velocity $\mathbf{v}(\mathbf{x},t)$ from the equations of fluid motion for known forces.

- *Pressure* of a fluid is a force per unit area in the normal direction. In general, fluids exert forces in both normal and tangential directions on surfaces with which they are in contact. Pressure of a fluid consider the forces only in normal direction. For a given position $\mathbf{x}$ and t, it can be defined as

$$p(\mathbf{x},t) = \lim_{\Delta A \to 0} \frac{\Delta F_{\mathbf{n}}}{\Delta A}$$

where $F_{\mathbf{n}}$ is the force in the normal direction $\mathbf{n}$ on a small surface ΔA.

- *Temperature* is a measure of the internal energy of the fluid, i.e., the energy associated with the thermal motions of the molecules making up the fluid.

The above discussed properties are typical physical properties of a fluid. More physical properties can be also identified from combination of these properties. For fluids, there exist also *transport properties* such as *viscosity* (see section 2.3.2) which distinguish the motion characteristics of flowing fluids.

2.1.2 Lagrangian and Eulerian perspective

In the study of fluid motion there are two ways to describe what is happening. The first is known as the *Lagrangian perspective* which follows the history of individual fluid particles. The alternative is the *Eulerian perspective* which concentrates on the flow behavior at a fixed spatial point.

Eulerian perspective

In the Eulerian perspective a fixed reference frame is employed relative to which a fluid is in motion. Time and spatial position in this reference frame $(\mathbf{x},t)$ are used as independent variables. The fluid properties such as mass density, pressure and flow velocity which describe the physical state of the fluid flow in question are dependent variables, they are functions of the independent variables. Thus their derivatives are partial with respect to $(\mathbf{x},t)$. For example, the flow velocity at a spatial position $\mathbf{x}$ and time t is given by $\mathbf{v}(\mathbf{x},t)$ and the corresponding acceleration at this position and time is then

$$\mathbf{a} = \left.\frac{\partial \mathbf{v}(\mathbf{x},t)}{\partial t}\right|_{\mathbf{x}} \tag{2.1}$$

where the time derivative is for the same position.

Lagrangian perspective

In the Lagrangian perspective the fluid is described in terms of its constituent fluid elements. Different fluid elements have different labels, e.g. their spatial positions at a certain fixed time t_0 are $\mathbf{x}_0$. The independent variables are thus $(\mathbf{x}_0,t_0)$ and the particle position $\mathbf{x}(\mathbf{x}_0,t)$ is a dependent variable. One can then ask about the rate of change in time in a reference frame co-moving with the fluid element, and

this then depends on time and particle label, i.e. which particular fluid element is being followed.

For example, if a fluid element has some velocity $\mathbf{v}(\mathbf{x}_0, t)$, then the acceleration it feels will be

$$\mathbf{a} = \left.\frac{D\mathbf{v}(\mathbf{x}_0, t)}{Dt}\right|_{\mathbf{x}_0} \tag{2.2}$$

where the notation signifies that $\mathbf{x}_0$ is kept constant, i.e. the time derivative is for the same fluid element. D/Dt emphasize the fact that the derivative is taken following a fluid element.

The Lagrangian and Eulerian reference frames are related by the *substantial derivative*. For any fluid property $f(\mathbf{x}, t)$ in a flow field with velocity $\mathbf{v}$, the substantial derivative is given by

$$\frac{Df}{Dt} = \frac{\partial f}{\partial t} + \mathbf{v} \cdot \nabla f \tag{2.3}$$

2.1.3 Steady and unsteady flow

Steady and unsteady flow is one of the most important distinctions which is often easy to recognize. If the fluid parameters are functions of space but not functions of time, then the flow is taken as steady. Mathematically this is expressed by partial derivatives with respect to time of any fluid parameter vanishes. Otherwise, it is called unsteady. Whether a particular flow is steady or unsteady, may depend on the chosen frame of reference. For instance, laminar flow over a sphere is steady in the frame of reference that is stationary with respect to the sphere while in other reference frames, it is unsteady.

Real physical flows always exhibit some degree of unsteadiness. But in many situations the time dependence may be sufficiently weak to justify a steady-state analysis.

2.1.4 Compressibility

In fluid analysis, compressibility is a measure of the relative volume change of a fluid as a response to a pressure or temperature change. All fluids are compressible to some extent, that is changes in pressure or temperature will result in changes in density. However, in many situations the changes in pressure and temperature are sufficiently small that the changes in density are negligible. In

this case the flow can be modeled as an incompressible flow. Otherwise the more general compressible flow equations must be used.

In Lagrangian perspective, an incompressible flow follows

$$\frac{D\rho}{Dt} = 0 \tag{2.4}$$

After substituting in the Equation 2.3 and applying the continuity equation (Equation 2.14), this can be derived to the following form

$$\nabla \cdot \mathbf{v} = 0 \tag{2.5}$$

which is the incompressibility condition and it is widely applicable to fluids.

2.2 Fluid Kinematics

The kinematics of a flow describe the motion of the fluid without taking into account of the forces that cause this motion. The motion of a fluid can be described by a velocity field which is a *vector field* $\mathbf{v}$ on some open set $D \subset \mathbb{R}^m \times \mathbb{R}$. It is a function that associates a vector $\mathbf{v}(\mathbf{x},t)$ to each point in spatial-temporal domain D

$$\mathbf{v} : D \longrightarrow \mathbb{R}^n$$

For 2D vector field, it is expressed as

$$\mathbf{v}(\mathbf{x},t) = \begin{cases} u(x,y,t) \\ v(x,y,t) \end{cases}$$

And for 3D vector field, it is expressed as

$$\mathbf{v}(\mathbf{x},t) = \begin{cases} u(x,y,z,t) \\ v(x,y,z,t) \\ w(x,y,z,t) \end{cases}$$

2.2.1 Characteristic curves

Classical observations of fluid motion are characterized by some characteristic curves. Specified fluid elements of a fluid are swept along with the mean flow and their trajectories sketch the characteristic curves of the fluid motion. Streamline, path-line and streak-line are three important characteristic curves of flow visualization.

Streamline

Streamlines are curves tangential to the instantaneous direction of the flow velocity in all points of the flow field. For a given flow, at an instant of time t_c, there is at every point $\mathbf{x} = (x,y,z)$ a velocity vector $\mathbf{v}(\mathbf{x},t_c) = (u,v,w)$. Let $d\mathbf{s} = (dx,dy,dz)$ be an element of arc length along a streamline, then by definition

$$\frac{dx}{u} = \frac{dy}{v} = \frac{dz}{w} \tag{2.6}$$

along the streamline. Streamlines can't cross and no fluid is flowing across a streamline at the instant considered. Streamlines display a snapshot of the entire flow field at a single instant. For a time-dependent flow, the streamline pattern changes with time. Streamlines can be visualized by seeding the fluid with small particles (see section 2.4) and photographing the flow field with an appropriate and known exposure time, so that each particle appears as a streak in the picture. The magnitude and direction of velocity in selected points of the flow field can be obtained and the streamlines can be found by drawing the curves tangential to the particle streaks.

Path-line

A path-line of a given flow, is the curve that an individual fluid element traverses in the flow field as a function of time. Mathematically, a path-line $\mathbf{p}(t)$ can be written in the following form,

$$\frac{d\mathbf{p}(t)}{dt} = \mathbf{v}(\mathbf{p}(t),t) \tag{2.7}$$

A path-line contains the integrated time history of the motion of one single fluid element. It can be visualized if one takes a long-time exposure record of the motion of one foreign particle, which has been introduced into the flow.

Streak-line

A streak-line is the locus of all fluid elements that have previously passed through a particular, fixed point of the flow field. It can be visualized by continuously injecting dye, or smoke, or another appropriate material into the flow from selected positions. Compared with path-lines, streak-lines corresponds to continuous injection of material particles and instantaneous observation of them, whereas path-lines are formed by instantaneous injection and continuous observation.

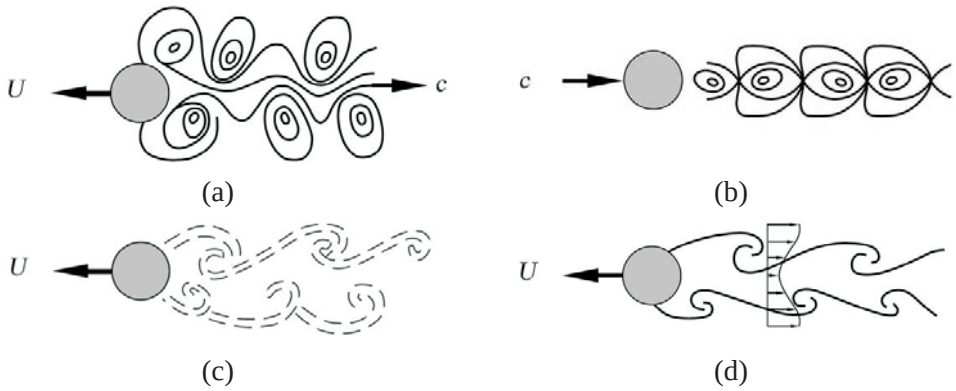

Figure 2.1: Characteristic curves of a Von Kármán vortex street [Oer02]:(a) Streamlines with observer at rest; (b) Streamlines with with observer; (c) Path-lines; (d) Streak-lines

For steady fluid, these three characteristic curves coincide. But in a flow, which explicitly depends on time, the three types of curves are different from one another. Figure 2.1 shows an example of these characteristic curves of an unsteady flow, which is named as Von Kármán vortex street [Oer02].

Besides, *material line element* is another concept often used in fluid analysis. It is a small line element marked in the fluid, i.e., made up of fluid elements, moving with the flow.

2.2.2 Flow topology

The analysis of the topology of a flow serves to provide an understanding of the *critical points*, or *singularities* that are produced by the velocity vector field and their relations to each other [Oer02]. In a critical point the magnitude of the velocity vanishes and in these points no direction is associated with the streamlines according to equation 2.6. There are various types of critical points, which can be characterized according to the behavior of nearby streamlines. Figure 2.2 shows an example of three typical critical points of a fluid flow, which are called source, sink and center. For a vector field, which can be approximated by a series of expansion about a critical point, closer investigation of the surrounding space of the critical point is carried out to classify the behavior.

Consider a steady 2D velocity vector field $\mathbf{v}$, which is assumed to be continuous

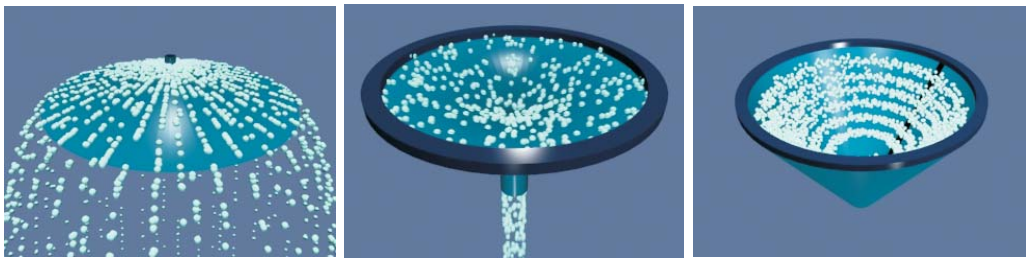

(a) (b) (c)

Figure 2.2: An example of critical points of particles and the flow from lecture notes http://web.mit.edu/8.02t/www/: (a) Source; (b) Sink; (c) Center.

and differentiable. Then the partial derivatives of $\mathbf{v}$ can be written as

$$\mathbf{v}_x(x,y) = \begin{pmatrix} u_x(x,y) \\ v_x(x,y) \end{pmatrix} \quad ; \quad \mathbf{v}_y(x,y) = \begin{pmatrix} u_y(x,y) \\ v_y(x,y) \end{pmatrix}$$

The Jacobian matrix $J_\mathbf{v}$ is a 2×2 matrix which is defined in every point of the domain of the vector field by

$$J_\mathbf{v}(x,y) = \begin{pmatrix} u_x(x,y) & u_y(x,y) \\ v_x(x,y) & v_y(x,y) \end{pmatrix}$$

The determinant of $J_\mathbf{v}$ is called Jacobian of $\mathbf{v}$.

A critical point $\mathbf{x}_o$ in the vector field $\mathbf{v}$ is called a first order critical point if and only if the Jacobian does not vanish in $\mathbf{x}_o$; otherwise the critical point is called higher order critical point.

For first order critical point, it can be classified by the eigenvalues of the Jacobian matrix [HH89].

Figure 2.3 shows how the eigenvalues classify a critical point as an attracting node, a repelling node, an attracting focus, a repelling focus, a center or a saddle, where R_1 and R_2 denote the real parts of the eigenvalues of the Jacobian matrix; I_1 and I_2 denote the corresponding imaginary parts. A positive or negative real part of an eigenvalue indicates an attracting or repelling nature; respectively, the imaginary part denotes circulation around the critical point.

Among these points, the saddle points are distinct, in which only four streamlines actually end at the point itself. At the saddle point, these curves are tangent to the two eigenvectors of the Jacobian matrix, which act as the *separatrices* of the saddle point. The outgoing and incoming separatrices are parallel to the eigenvectors with positive and negative eigenvalues respectively.

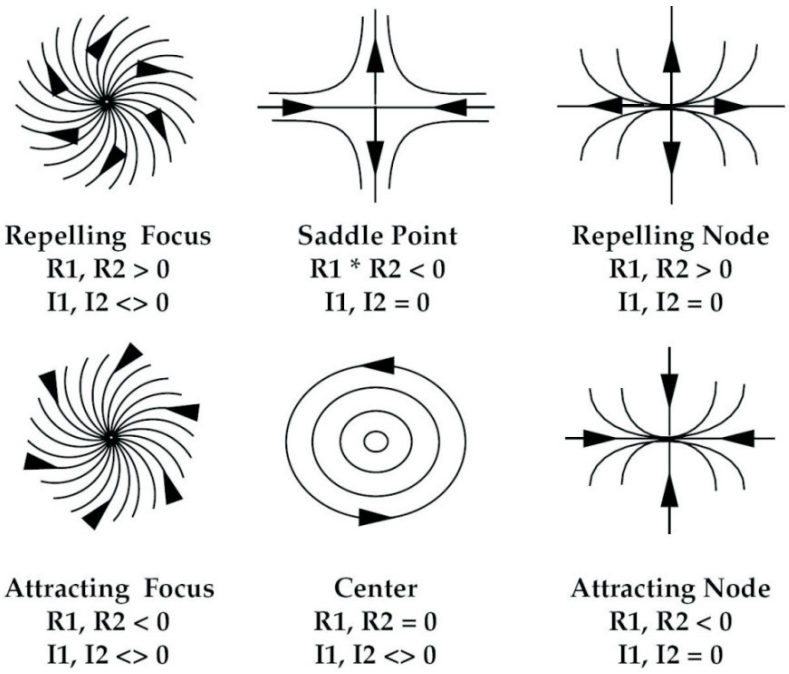

Figure 2.3: First order classification criteria for critical points [HH89, PVH*03].

2.2.3 Vortex kinematics

Vortex is a classical topic in fluid analysis, however an accepted definition of vortex is still lacking [JH95]. A spinning flow with circular streamlines is known as a vortex as shown in Figure 2.4. The fluid pressure in a vortex is lowest in the center where the speed is greatest, and rises progressively with distance from the center. Vortices contain a lot of energy in the circular motion of the fluid. In an ideal fluid this energy can never be dissipated and the vortex would persist forever. However, real fluids exhibit viscosity and this dissipates energy very slowly from the core of the vortex.

Vorticity is a mathematical concept used in fluid analysis. It can be related to the local angular rate of rotation in a fluid. It is a vector-valued function of position and time defined as

$$\omega = \nabla \times \mathbf{v} \tag{2.8}$$

The vorticity at a point is a measure of the local rotation. For the large scale rotational properties of a flow, the concept *circulation* is introduced. The circulation Γ around a closed contour C is defined as the line integral of the tangential component of the velocity

$$\Gamma = \oint_C \mathbf{v} \cdot dl \tag{2.9}$$

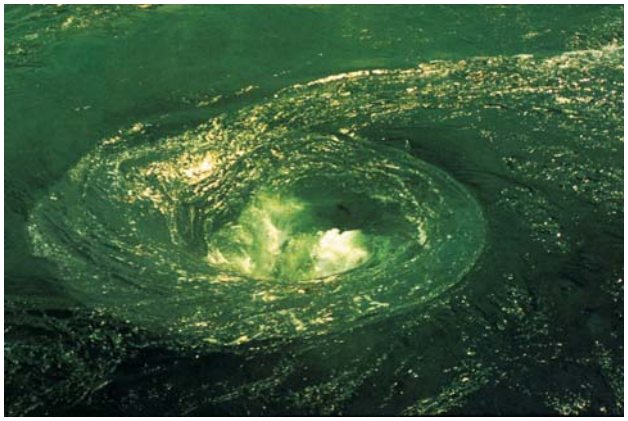

Figure 2.4: A vortex in water. WL| Delft Hydraulics [PVH*03].

From the Stokes' integral theorem [KC04], the circulation becomes

$$\Gamma = \iint_S (\nabla \times \mathbf{v}) \cdot dA = \iint_S \omega \cdot dA \tag{2.10}$$

where S is an arbitrary surface entirely in the fluid that spans C.

A *vortex line* is a curve in the fluid such that its tangent at any point parallels to the local vorticity [Bat67]. The core of every vortex can be considered to contain a certain vortex line, and every fluid element in the vortex can be considered to be circulating around the vortex line. Vortex lines passing through any closed curve form a tubular surface, which is called a *vortex tube*.

There are two basic vortex flows. One is *rotational vortex*, whose tangential velocity is

$$\mathbf{v}_\theta = \frac{1}{2}\omega r \tag{2.11}$$

The vorticity of an element is everywhere equal to ω and it rotates as a solid body with no shear. The other type is *irrotational vortex*, whose tangential velocity is

$$\mathbf{v}_\theta = \frac{\Gamma}{2\pi r} \tag{2.12}$$

For irrotational vortex, the vorticity is 0 everywhere except at the origin where the vorticity is infinite.

In an inviscid, *barotropic* flow with conservative body forces, the circulation around a closed curve moving with the fluids remains constant with time. Barotropic here means that the fluid density is a function of pressure alone such as incompressible or isentropic. This statement is known as *Kelvin's Circulation Theorem*.

Kelvin's theorem essentially states that irrotational flows remain irrotational at all times. With the same conditions, *Helmholtz Vortex Theorem* made the further statements

- Vortex lines are material lines moving with the fluid.
- The strength of a vortex tube, which is the circulation, is constant along its length
- A vortex line can not end within the fluid. It must either end at a solid boundary or form a closed loop (a *vortex ring*).
- Strength of a vortex tube remains constant in time

2.3 Fluid Dynamics

Fluid dynamics presents the basic development of fluid principles and their applications in solving problems concerning of fluid motion. It carries out a systematic study of the theoretical, empirical and semi-empirical laws, derived from fundamental physics and flow measurement. The solution of a fluid dynamics problem typically involves calculation of various properties of the fluid as functions of space and time.

2.3.1 Fundamental principles

Within the continuum framework (see section 2.1.1), classical physical theories can be applied to fluid analysis. The foundational principles of fluid dynamics are the conservation laws [KC04], i.e. conservation of mass, momentum and energy.

The mathematical expressions of these fundamental principles can be stated in either differential form or integral form and both forms can be derived from each other.

Conservation of mass

Consider a volume V fixed in space as shown in Figure 2.5, the rate of increase of mass inside the volume must equal to the rate through the boundary A, therefore,

$$\int_V \frac{\partial \rho}{\partial t} dV = -\int_A \rho \mathbf{v} \cdot dA \tag{2.13}$$

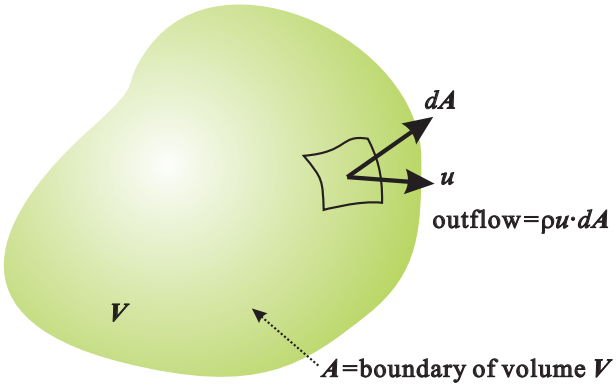

Figure 2.5: Mass conservation of a volume fixed in space.

By means of the divergence theorem [KC04], the surface integral can be transformed to a volume integral and the divergence form is obtained as follows,

$$\frac{\partial \rho}{\partial t} + \nabla \cdot (\rho \mathbf{v}) = 0 \tag{2.14}$$

which is called *continuity equation*.

Conservation of momentum

The study of fluid motion is determined by the *Newton's Second Law of Motion* which relates the acceleration of the motion of a fluid to the forces that are generating the motion. The idea is the physical principle that the linear momentum of any particular fluid element is conserved.

For any deformable continuous medium the *stress tensor* τ_{ij} encodes the transfer rate of linear momentum across contact surfaces between neighboring volume elements which is due to molecular motions within the medium. One example on the surface with normal $\mathbf{n}_1$ is shown on Figure 2.6a.

Consider the motion of a infinitesimal fluid element shown in Figure 2.6b, Newton's law requires that the force on the element must equal mass times the acceleration of the element. With ρg_i as the body force per unit volume, the Newton's law gives

$$\rho \frac{Dv_i}{Dt} = \rho g_i + \frac{\partial \tau_{ij}}{\partial x_j} \tag{2.15}$$

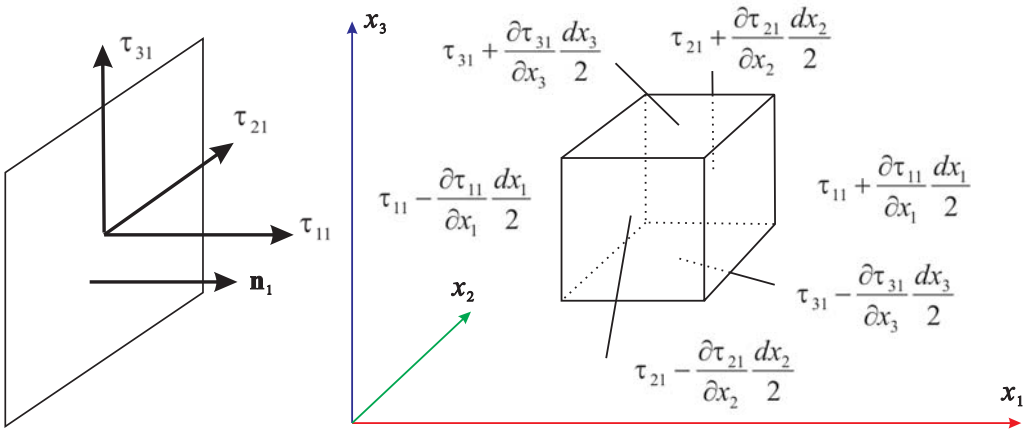

(a) (b)

Figure 2.6: (a)Stress tensor on one surface of an element;(b) Surface stresses on an element moving with the flow, only stresses in the x_1 direction are labeled.

This is the equation of motion relating acceleration to the net force at a point and describes how linear momentum is transferred between neighboring volume elements. It is usually called *Cauchy's Equation of Motion*.

Conservation of energy

In physics, the conservation of energy states that the total amount of energy in any isolated system remains constant but can't be recreated, although it may change forms. The equation for the kinetic energy of a fluid can be obtained from the momentum equation,

$$\rho \frac{D}{Dt}(\frac{1}{2}v_i^2) = \rho g_i v_i + v_i \frac{\partial \tau_{ij}}{\partial x_j} \tag{2.16}$$

which is not a sperate principle. In flows with temperature variations, an independent equation needs to be considered. Let **q** be the heat flux vector per unit area and e the *internal energy* per unit mass, the *First Law of Thermodynamics* states that the rate of change of stored energy equals the sum of rate of work done and rate of heat addition to a material volume, that is,

$$\rho \frac{D}{Dt}(e + \frac{1}{2}v_i^2) = \rho g_i v_i + \frac{\partial(\tau_{ij} v_i)}{\partial x_j} - \frac{\partial q_i}{\partial x_i} \tag{2.17}$$

Besides the first law of thermodynamics, the *Second Law of Thermodynamics* states that the real phenomena can only proceed in a direction in which the "dis-

order" of an isolated system increases. Disorder of a system is measured of the degree of uniformity of macroscopic properties in the system and it is usually called *entropy*.

2.3.2 Viscous effects

The characteristic that distinguishes a fluid from a solid is its continually deforms under an applied shear stress. For a fluid, the transport of momentum constitutes internal friction, and the fluid exhibiting internal friction is said to be *viscous* [Bat67]. *Viscosity* is a measure of the resistance of a fluid to being deformed by shear stress.

The *Newton's Law of Friction* states that the magnitude of the shear stress τ along a surface element is proportional to the velocity gradient across the element

$$\tau = \mu \frac{d\mathbf{v}}{dy} \tag{2.18}$$

where the constant of proportionality μ is known as *dynamic viscosity*, which is a strong function of temperature T. In many situations, the ratio of the viscous force to the inertial force is concerned. The inertial force is characterized by the fluid density ρ and the ratio is defined as follows

$$\nu = \frac{\mu}{\rho} \tag{2.19}$$

which is called *kinematic viscosity*. Fluids, either liquids or gases, which satisfy Newton's Law of Friction are known as *Newtonian fluids*. Non-Newtonian fluids exhibit a more complicated relationship between shear stress and velocity gradient than simple linearity. For ideal fluids, they support no shearing stress and flow without energy dissipation. Fluids without viscous effects are called *inviscid fluids*.

2.3.3 Navier-Stokes Equation

The relation between the stress and deformation in a fluid is called a *constitutive equation*. Without body force, a stress tensor is symmetric and can always be resolved into the sum of two symmetric tensors. One is a *hydrostatic stress tensor* which involves only tension and compression and the other is a *deviatoric stress tensor* which involves shear stress [KC04]. In the case of a fluid, *Pascal's Law* shows that the hydrostatic stress is the same in all directions and can be expressed

by the scalar property pressure p. The deviatoric stress tensor is related to velocity gradients $\partial v_i/\partial x_j$ and for an incompressible fluid, the constitutive equation can be expressed as following

$$\tau_{ij} = -p\delta_{ij} + \mu(\frac{\partial v_i}{\partial x_j} + \frac{\partial v_j}{\partial x_i}) \tag{2.20}$$

where p here is only interpreted as the mean pressure. For a compressible fluid, a thermodynamic pressure need to be derived and the constitutive equation becomes

$$\tau_{ij} = -(p + \frac{2}{3}\mu\nabla\cdot\mathbf{v})\delta_{ij} + \mu(\frac{\partial v_i}{\partial x_j} + \frac{\partial v_j}{\partial x_i}) \tag{2.21}$$

The equation of motion for a Newtonian fluid is obtained by substituting the constitutive equation (Equation 2.20) into Cauchy's equation (Equation 2.15) to obtain

$$\rho\frac{Dv_i}{Dt} = -\frac{\partial p}{\partial x_i} + \rho g_i + \frac{\partial}{\partial x_j}\Big[\mu(\frac{\partial v_i}{\partial x_j} + \frac{\partial v_j}{\partial x_i}) - \frac{2}{3}\mu(\nabla\cdot\mathbf{v})\delta_{ij}\Big] \tag{2.22}$$

which is a general form of the *Navier-Stokes Equation*. For incompressible fluids $\nabla\cdot\mathbf{v} = 0$ and using vector notation, the Navier-Stokes Equation reduces to

$$\rho\frac{D\mathbf{v}}{Dt} = -\nabla p + \rho\mathbf{g} + \mu\nabla^2\mathbf{v} \tag{2.23}$$

For inviscid fluid, we obtain the *Euler Equation*

$$\rho\frac{D\mathbf{v}}{Dt} = -\nabla p + \rho\mathbf{g} \tag{2.24}$$

2.3.4 Similarity and dimensionless parameter

Two flows having different values of length scales, flow speeds, or fluid properties can apparently be different but still share some similarity. This have been widely used in experimental fluid mechanics. There are generally three kinds of similarity, the geometric similarity, the kinematic similarity and the dynamic similarity. Dimensional analysis is used to check the similarities [KC04]. According to the *Buckingham π-theorem* of dimensional analysis, the functional dependence between n variables can be reduced to $n-r$ independent dimensionless variables, where r is the rank of the dimensional matrix. For the experiment purposes, different systems which share the same description by dimensionless quantity are equivalent. Dimensionless parameters are important to characterize the dynamic similarity and are essential in fluid dynamics analysis. Several significant common dimensionless parameters are sketched here.

Reynolds Number

The *Reynolds Number* is the ratio of inertia force to viscous force:

$$Re = \frac{Ul}{\nu} \tag{2.25}$$

where U is the mean fluid velocity and l is the characteristic length.

Reynolds Number is used to identify and predict different flow regimes, such as laminar or turbulent flow. Laminar flow occurs at low Reynolds numbers, where viscous forces are dominant, and is characterized by smooth, constant fluid motion, while turbulent flow, on the other hand, occurs at high Reynolds numbers and is dominated by inertial forces, which tend to produce random eddies, vortices and other flow fluctuations.

Mach Number

The *Mach Number* is the ratio of inertia force to compressibility force:

$$M = \frac{U}{c} \tag{2.26}$$

where c is the speed of sound.

Mach Number is a requirement for the dynamic similarity of compressible flows. Compressibility effects can be neglected if $M < 0.3$. Flows in which $M < 1$ are called *subsonic*, whereas flows in which $M > 1$ are called *supersonic*.

Pressure Coefficient

The *Pressure Coefficient* is the ratio of pressure force to inertial force:

$$C_p = \frac{p - p_\infty}{\frac{1}{2}\rho \mathbf{v}_\infty^2} \tag{2.27}$$

where p is the pressure at the point of measure, p_∞ is the free-stream pressure which is remote from any disturbance, and $\mathbf{v}_\infty$ is the free-stream fluid velocity or the velocity of the body through the fluid. $C_p = 0$ indicates the pressure is the same as the free stream pressure while $C_p = 1$ indicates the pressure is stagnation pressure and the point is a stagnation point. In the fluid flow field around a body there will be points having positive pressure coefficients up to one, and negative pressure coefficients, including coefficients less than minus one, but nowhere will the coefficient exceed plus one because the highest pressure that can be achieved is the stagnation pressure.

Drag Coefficient

Drag Coefficient is a dimensionless quantity that describes the aerodynamic drag caused by fluid flow. For a specified object, the Drag Coefficient C_d can be derived by integrating the distribution of corresponding Pressure Coefficients:

$$C_d = \frac{1}{2}\int_0^{2\pi} C_p(\theta) cos\theta d\theta \tag{2.28}$$

Drag Coefficient is widely applied in aerodynamics, the drag force of an object can be calculated in the following way,

$$F = \frac{1}{2} C_d \rho \mathbf{v}^2 A \tag{2.29}$$

where A is the projected frontal area.

2.3.5 Laminar and turbulent flow

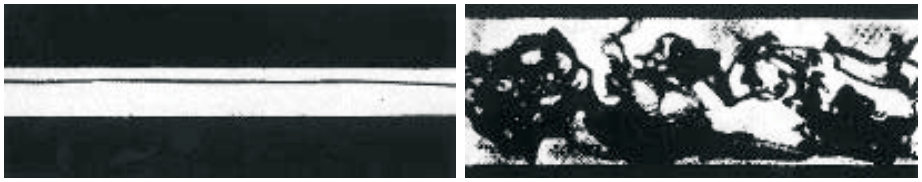

(a) (b)

Figure 2.7: Laminar and turbulent flow in a pipe [Oer02]: (a) Steady laminar; (b) Turbulent.

The distinction between laminar and turbulent is one of the most important points for the analysis of fluids. Figure 2.7 shows the fluid flowing through a pipe with a dye injected at the inlet. The dye filament is straight and smooth in Figure 2.7a for low speeds and it breaks off and disperse almost uniformly in Figure 2.7b when the flow speed is high enough. The first case is laminar flow which occurs when a fluid flows in parallel layers, with no disruption between the layers while the second case is turbulent flow which is dominated by recirculation, eddies, and apparent randomness. In fluid dynamics, laminar flow is a flow regime characterized by high momentum diffusion, low momentum convection, pressure and velocity independent from time and turbulent flow is fluid characterized by irregular, chaotic movements of fluid particles. This includes low momentum diffusion, high momentum convection, and rapid variation of pressure and velocity

in space and time. The Reynolds Number characterizes whether flow conditions lead to laminar or turbulent flow (see section 2.3.4).

The transport properties of turbulence are dominated by the advection of infinitesimal fluid elements, it is natural to resort to the Lagrangian viewpoint, following the motion of the fluid elements [Oer02]. Turbulence have a well-documented tendency to form *coherent structures*. The remarkable feature of the coherent structures observed in both numerical and experimental work is their long lifetimes. Much energy has been put into identifying coherence in vortical structures, determining their stability properties, and analyzing the dynamics of vortex interactions including merging.

2.4 Experimental Fluid Analysis

Experimental analysis is one fundamental way to understand the complex fluid phenomena, which serves as foundation of theoretical fluid analysis. They are usually carried out in wind pipes, tanks, tunnels and so on. Fluid motion can be measured and then analyzed manually or with computer support (see section 2.5). One intuitive way is to directly visualize the fluid motion during the experiments.

2.4.1 Experimental visualization techniques

A proper visualization technique is usually the determinant factor for the experimental fluid analysis. During the development of fluid analysis there has been evidence of a rapidly growing interest in the methods of flow visualization [Mer74]. To getting insights into a fluid phenomenon, it is essentially important to understanding the dynamical features, which appear as special patterns during the fluid transport. However, most fluids are transparent, thus their flow patterns are invisible to human perception. Flow visualization is the art of making underlying patterns in liquids and gases visible. The study dates back at least to the Renaissance, when Leonardo Da Vinci sketched images of fine particles of sand and wood shavings which had been dropped into flowing liquids. Since then, laboratory flow visualization has become more and more exact, with careful control of the particulate size and distribution. Advances in photography has also helped extend the understanding of how fluids flow under various circumstances.

Generally, experimental fluid visualization can be distinguished into the following three basic groups of methods [Mer74, Dyk82].

(a) (b) (c)

Figure 2.8: Experimental flow visualization techniques, three examples: (a) Smoke lines around a road vehicle in a full-scale wind tunnel [Huc94]; (b) Shadow graph of an airplane model in free flight at $M = 1.1$ [Dyk82]; (c) Laminar flow around a metallic profile. The model is placed between two rod electrodes [Mer74].

Foreign material methods: This group comprises all techniques by which a foreign material is added to the flowing fluid and makes the particle, path or surface visible. Dye, smoke, or tufts is injected into liquids or gases to visualize flow dynamics. A problem with injecting material is that the injection process and the injected material may influence the flow. Using electrolytic techniques for generating hydrogen bubbles within the flow decreases these problems to a certain extent. Also photochemical methods are used, for instance, generating dye within the flow using a laser beam. The foreign material methods give excellent results in stationary flows, but the errors can be enormous for unsteady flows. The methods also fail to give precise results, if thermodynamic state of the fluid varies in such as compressible fluid. An example of the foreign material method can be seen in Figure 2.8a, where the air flow around full-scale vehicle has been visualized by means of smoke.

Optical methods: The refractive index of a fluid medium is a function of the fluid density. Compressible flows can be made visible by means of certain optical methods that are sensitive to changes of the index of refraction in the field under investigation. For the group of optical flow visualization methods, a light beam transmitted through a flow field with varying density is affected with respect to its optical phase and its intensity remains unchanged. An optical device behind the flow field provides in a recording plane a nonuniform illumination due to the phase changes. From the pattern in the recording plane, one can concludes the corresponding density variation in the flow field. Optical methods achieves less disturbance of the original flow. An example of the optical method can be seen in Figure 2.8b, where shadows in the image denote shock waves during the flight of the airplane model.

Energy methods: Energy in the form of either heat or electric discharge are introduced into the flowing fluid as foreign substance. Heat can be applied to flows to artificially increase the density variation. Electrons shooting into the flow volume is used to excite gas molecules. The investigated fluid elements are marked by their increased energy level and they can be discriminated from the rest of the fluid directly or by an optical visualization method. These methods are often applied to flow with low average density level and the density changes can be too weak to be detected by an optical method. This group of visualization methods is suitable for rarefied or low-density gas flows, which one often distinguishes from the ordinary incompressible and compressible flows. It is not a nondisturbing method either, since it affects, more or less, the original flow according to the amount of released energy. An example of the energy method can be seen in Figure 2.8c, where a metallic model is placed between two rod electrodes and the velocity profile is visualized by spark tracer techniques [Mer74].

Although experimental methods have advantages, they influence the flow themselves. They are usually time consuming and very expensive and only a limited set of flow properties can be visualized using experimental techniques.

2.5 Computer Aided Fluid Analysis

As the evolving of computer technology, the field of fluid analysis is extending. With high computation power and efficient algorithms, the fluid phenomena can be simulated. The visual depth of the complex phenomena has also been increased with high-performance computer graphical techniques.

2.5.1 Computational fluid dynamics

Computational fluid dynamics (CFD) is a science that uses numerical methods and algorithms to produce quantitative predictions of fluid-flow phenomena based on those conservation laws governing fluid motion. These predictions normally occur under those conditions defined in terms of flow geometry, the physical properties of a fluid, and the boundary and initial conditions of a flow field. The prediction generally concerns sets of values of the flow properties, for example, velocity, pressure, or temperature at selected points in spatial-temporal domain. It may also evaluate the overall behavior of the flow, such as the flow rate or the hydrodynamic force acting on an object in the flow. However, even with simplified equations and high-speed supercomputers, only approximate solutions can be achieved in many

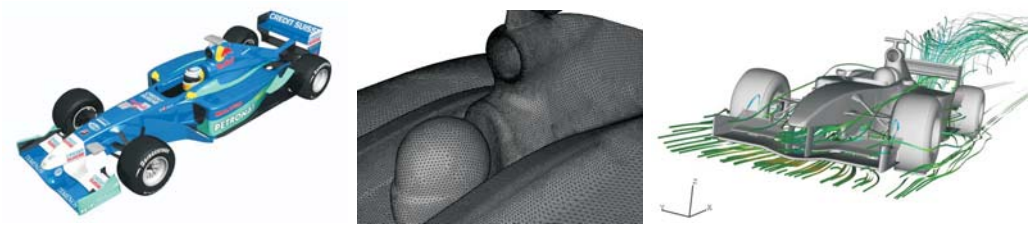

(a) (b) (c)

Figure 2.9: A CFD example for the Red Bull Sauber C-20 F1 racing car using CFD software *Fluent* [Flu02]: (a) A model of the car; (b) The surface mesh in the cockpit area; (c) Path lines around the vehicle.

cases. Techniques for accurate and quick simulation of complex scenarios such as transonic or turbulent flows are an ongoing area of research [And95].

The basis of CFD problems are partial differential equations (PDE) which represent conservation laws for the mass, momentum and energy, i. e. the Navier-Stokes equations for single-phase fluid flow. CFD is the art of replacing such PDE systems by a set of algebraic equations which can be solved using digital computers.

In order to study the behavior of certain object under a fluid flow environment, a model with geometrical similarity to the original object are constructed using computer graphics techniques. Figure 2.9a shows a geometrical model of the Red Bull Sauber C-20 F1 racing car [Flu02]. Material properties and boundary conditions are necessary to be specified before applying the CFD approaches.

The fundamental consideration in CFD is how to treat a continuous fluid in a discrete environment on a computer. One method is to discretize the spatial domain into small cells to form a volume mesh or grid, and then apply a suitable algorithm to solve the equations of motion. The cells can be either irregular or regular and the distinguishing characteristic of the former is that each cell must be stored separately in memory. Figure 2.9b shows an example of surface mesh of the racing car on the driver's helmet and cockpit area. From the surface meshes, the volume can be divided further into prismatic cells. After meshing the investigating space, the governing equations are discretized correspondingly and solved for each elements. *Finite difference*, *finite element* and *finite volume* are three common discretization methods for CFD computation. The stability of the chosen discretization is generally established numerically rather than analytically as with simple linear problems.

Laminar flows can be directly solved by the Navier-Stokes equations. It is also possible to solve turbulent flows directly when all of the relevant length scales can

be resolved by the cell. In general however, the range of length scales appropriate to the problem is larger than even today's massively parallel computers can model. In these cases, turbulent flow simulations require the introduction of a turbulence model. This means that it is required for a turbulent flow regime to take this into account by modifying the Navier-Stokes equations. In many instances, other equations are solved simultaneously with the Navier-Stokes equations. These other equations can include those describing species concentration, chemical reactions, heat transfer, etc. More advanced codes allow the simulation of more complex cases involving multi-phase flows, non-Newtonian fluids, or chemically reacting flows.

It is also necessary to do the validation after the CFD process to ensure that the CFD code produces reasonable results for a certain range of flow problems. It is usually done by comparing the results with available experimental data to check if the reality is represented accurately enough. Sensitivity analysis and a parametric study are carried out to assess the inherent uncertainty due to the insufficient understanding of physical processes.

2.5.2 Computer graphics flow visualization

Visualization is an important subfield of research and development in computer science. As the development of CFD and measurement technology, a complex fluid phenomenon can be recorded as a set of data. Flow visualization is no longer restricted in experiments. *Computer graphics flow visualization* has become one important topic for fluid analysis. The heart of this process is the translation of physical to visual variables. Computer graphics flow visualization is not satisfied with only visualizing standard patterns of experimental flow visualization. Important patterns or features, which is of great concern in fluid mechanics but difficult for the implementation of experimental visualization, can be also visualized using computer graphics techniques. Even more, new vision of fluid phenomena pushes the development of theoretical fluid analysis. One example using computer graphics flow visualization can be seen in Figure 2.9c, where selected path-lines around the car are rendered.

Figure 2.10 shows the pipeline for the process of computer graphics flow visualization [PvW93, The01].

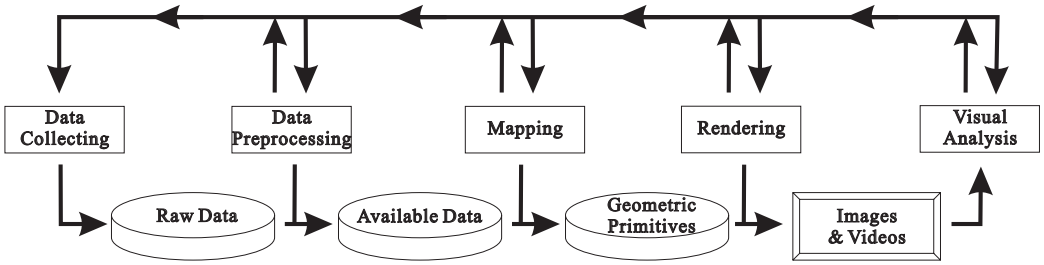

Figure 2.10: A pipeline model of the visualization process.

Data collecting

The data of computer graphics flow visualization are collected from the fluid production by measurement or numerical simulations. The measurement can be carried out directly, or can be derived from analysis of images obtained with experimental visualization techniques, using image processing techniques [Yan89]. Numerical flow simulations often produce velocity fields, sometimes combined with scalar data such as pressure, temperature, or density. The collecting data are usually raw data and most data sets we considered here comes from CFD simulations.

Data preprocessing

The data preprocessing includes modification or selection of the data, to reduce the amount or improve the information content of the data. Examples are domain transformations, sectioning, thinning, interpolation, sampling, and noise filtering. After data preparing, the data are available for the further processing of visualization approaches. The following enumerates several typical data preparing techniques.

Filtering: Measured data usually contain noise which may disturb visualization. The collected data can be viewed as a sampling from a continuous signal. In terms of signal processing, the source signal may contain too many high frequency components, caused by measurement noise and peaks. Filtering can be applied to remove these spurious high frequencies.

Data reduction: It is necessary to reduce the amount of data to be visualized, and to concentrate on the most interesting parts or features of the data. Subsampling is usually applied to reduce the data amount. Also, a part may be cut out

by clipping the data against a given volume. More sophisticated reduction can be done by calculating some interesting properties for each cell, and only visualizing cells with a high value of this property. Measures for this may be local extreme values of a quantity, or large gradients, such as sudden changes in velocity. The computed gradients can be treated as a scalar field, and volume rendering may be applied for visualization. A group of reduction techniques is the extraction of specific flow features or patterns, such as flow field topology or vortex cores which will be discussed in chapter 3

Interpolation: Flow quantities are usually given only at discrete points and for other points values must be obtained by interpolation. Interpolations may be of zero, first, or higher order, depending on the accuracy required.

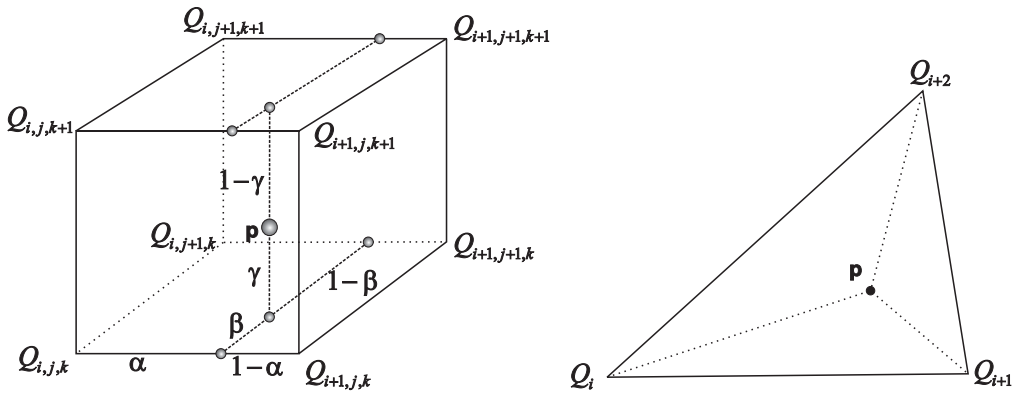

Figure 2.11: Interpolation: (a) Piecewise trilinear interpolation for regular grids; (b) 2D barycentric interpolation.

For data defined on regular grids, the piecewise trilinear (bilinear) interpolation algorithm is popular for the calculation of the values of non-grid points in 3D (2D) space. For given regular orthogonal grids in 3D space, each grid point $\mathbf{x}_{i,j,k} = (x,y,z)_{i,j,k}$ is specified with a fluid quantity $Q_{i,j,k}$ in either scalar, vector or tensor form, where (i,j,k) is the integer indices of the grid points. Any point $\mathbf{p}$ in the computational space can be calculated by the quantity values of the eight neighbor grid points surrounding it as shown in Figure 2.11a with the following formula,

$$\begin{aligned} Q_{\mathbf{p}} \;=\; & (1-\alpha)(1-\beta)(1-\gamma)Q_{i,j,k} + \alpha\beta\gamma Q_{i+1,j+1,k+1} + \\ & \alpha(1-\beta)(1-\gamma)Q_{i+1,j,k} + (1-\alpha)\beta\gamma Q_{i,j+1,k+1} + \\ & (1-\alpha)\beta(1-\gamma)Q_{i,j+1,k} + \alpha(1-\beta)\gamma Q_{i+1,j,k+1} + \\ & (1-\alpha)(1-\beta)\gamma Q_{i,j,k+1} + \alpha\beta(1-\gamma)Q_{i+1,j+1,k} \end{aligned} \tag{2.30}$$

where $\alpha = (x_{\mathbf{p}} - x_{i,j,k})/(x_{i+1,j,k} - x_{i,j,k})$, $\beta = (y_{\mathbf{p}} - y_{i,j,k})/(y_{i,j+1,k} - y_{i,j,k})$ and $\gamma = (z_{\mathbf{p}} - z_{i,j,k})/(z_{i,j,k+1} - z_{i,j,k})$.

For irregular grid points, *Delaunay triangulation* is applied to divide a 2D (3D) space into triangle (tetrahedron) cells [CLRS01]. 2D (3D) *barycentric interpolation* is carried out within each cell. For a 2D triangle mesh after Delaunay triangulation, each node $\mathbf{x}_i$ is specified with a fluid quantity Q_i in either scalar, vector or tensor form, where i is the integer index of the nodes. Any point $\mathbf{p}$ in the computational space can be calculated by the quantity values of the three neighbor nodes surrounding it as shown in Figure 2.11b with the following formula,

$$Q_{\mathbf{p}} = \frac{Q_i S_{\triangle \mathbf{p}\mathbf{x}_{i+2}\mathbf{x}_{i+1}} + Q_{i+1} S_{\triangle \mathbf{p}\mathbf{x}_{i+2}\mathbf{x}_i} + Q_{i+2} S_{\triangle \mathbf{p}\mathbf{x}_i\mathbf{x}_{i+1}}}{S_{\triangle \mathbf{x}_i\mathbf{x}_{i+1}\mathbf{x}_{i+2}}} \tag{2.31}$$

Mapping

The mapping processing translates the physical data to suitable visual primitives and attributes. This is the central part of the computer graphics flow visualization process. The conceptual mapping involves the art of a visualization: to determine what we want to see, and how to visualize it. Abstract physical quantities are cast into a visual domain of shapes, light, color, and other optical properties. Some classical visualization mappings of flow data will be discussed in chapter 3.

Rendering

The geometric primitives have to be painted onto the 2D screen. This issue is not a specific problem in visualization. Instead, standard approaches of Computer Graphics can be applied here [FvDFH96]. The resulting images or videos can now be visually analyzed by the scientists. Typical operations here are viewing transformations, lighting calculations, hidden surface removal, scan conversion, and filtering (anti-aliasing and motion blur).

The visualization process is an iterative process as shown in Figure 2.10. Analyzing the resulting images or videos, the fluid scientists may decide to go back in the visualization pipeline and change parameters in one of the upper steps. This way the new visualization may give better results to the analyst who can repeat these iterative steps as often as necessary. Of course, iterations to higher levels are possible at virtually every step of the visualization pipeline.

2.6 Conclusion

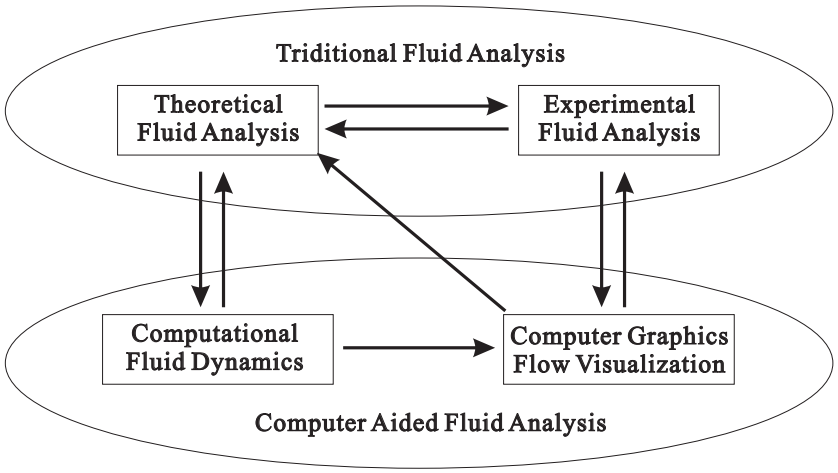

Figure 2.12: Methodology of fluid analysis.

Fluid analysis is one important topic for modern scientific and engineering research. For most of last few centuries there were two approaches to the study of fluid motion: theoretical and experimental. Many contributions to our understanding of fluid behavior were made by both of these methods. But today, because of the power of modern digital computers, there is yet a third way to study fluid behaviors: computational fluid dynamics as well as computer graphics flow visualization. In modern industrial practice computer aided fluid analysis has been used more for fluid flow analysis than either theoretical or experimental ones. Most of what can be done theoretically has already been done, and experiments are generally difficult and expensive. The computer aided fluid analysis has made a revolution of the methodology of fluid analysis as shown in Figure 2.12. It broads the vision of fluid research and pushes the development of fluid mechanics. As computing costs have continued to decrease, computer aided fluid analysis has also moved to the forefront in engineering analysis of fluid flow. Through out this thesis, we will focus on the computer graphics flow visualization which serves as a bridge between CFD and classical fluid analysis and enhances the understanding of the complex fluid phenomena. For simplification, the terminology ”flow visualization” in the following chapters only refers to ”computer graphics flow visualization”.

Chapter 3

Flow Visualization Techniques

Flow visualization is an important topic in scientific visualization and has been an active research field for many years. It has significantly different characteristics for different data and different user goals. From its very beginning, flow visualization had to face the problem of treating large and complex data. A variety of techniques have been developed for computing expressive visual representations for flow fields.

Flow visualization techniques can be classified in different ways. It can be classified into steady flow oriented techniques and time-dependent flow oriented techniques. It can be distinguished as 2D and 3D methods based on the spatial characteristics of flow data. By the involving scope of computation, flow visualization techniques can be categorized into elementary methods, local methods and global methods. Elementary methods show the properties of selected points while local methods show properties of the flow field around certain selected points. The global methods show global properties of the flow field. One classification scheme distinguishes flow visualization techniques into point-based, characteristic curve based and feature based groups by the relationship between a flow field and its associated visual representations [HJ05]. The categorization of direct flow visualization, texture-based flow visualization, geometric flow visualization and feature based flow visualization is also one popular classification for flow visualization techniques [PVH*03].

In this chapter, we will go through the common flow visualization techniques from the perspective of fluid analysis. Ordinary methods visualize the flow properties and patterns which are well explored in experimental flow visualization. Further techniques such as feature based techniques, information visualization based

techniques utilize the computation and analysis abilities of modern information technology. We will also pay special attentions to the visualization techniques of dynamic flow fields.

3.1 Ordinary Flow Visualization Methods

Flow visualization rooted from the experimental flow analysis techniques. On early days of flow visualization, people use computer techniques to generate the pictures similar to laboratory experiments. The properties or curves, which are well explored in experiments, contribute one part of important materials of modern flow visualization. The improvement and development of these algorithms are still an active field of flow visualization research.

3.1.1 Fluid property visualization

Fluid flow can be described by many different properties. Scientists and engineers usually concern the properties either scalars or vectors of certain locations or the distribution of such properties.

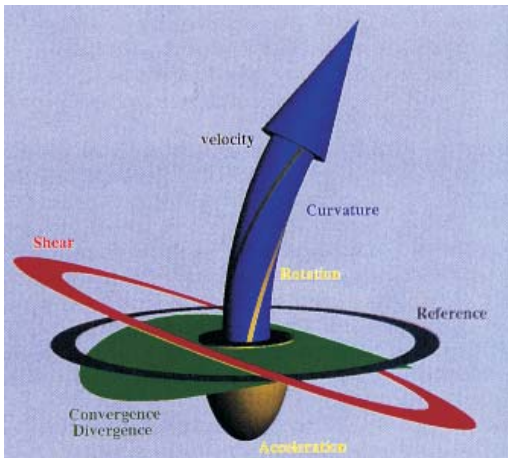

Figure 3.1: Local flow probe [dLvW93].

Local properties can be directly represented by icons or glyphs. One approach represents local flow properties derived from the Jacobian matrix by a local flow probe [dLvW93]. Direction, orientation, velocity, acceleration, curvature, rotation, shear, and convergence/divergence of the flow near a special state of interest

are mapped to distinct geometrical properties of a rather complex glyph as shown in Figure 3.1. Advanced visualization techniques on the basis of icons are presented in [PWPS95].

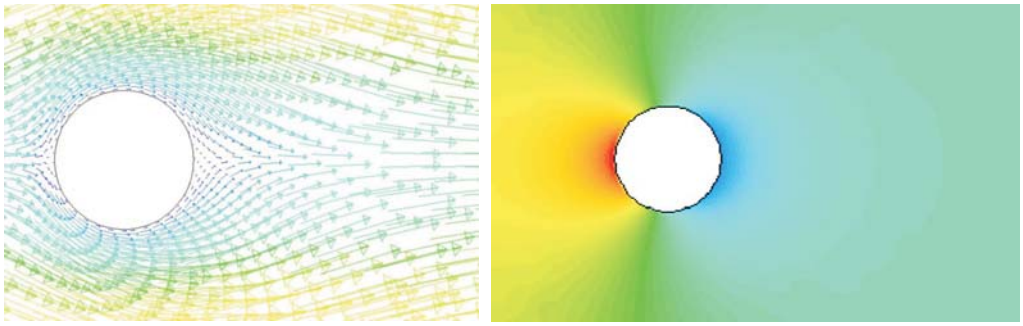

(a) (b)

Figure 3.2: Fluid property visualization of a 2D flow past a cylinder by André Bakker (http://www.bakker.org): (a) Vector plot of velocity field; (b) A color coding of pressure distribution.

The distribution of local properties can be visualized by *arrow plots* for vector properties and *color coding* or *volume rendering* for scalar properties [HLD*02]. Arrow plots give a natural vector visualization which map a arrow glyph to each sample point in the field. Usually a regular placement of arrows is used. Figure 3.2a shows an arrow plot visualization of velocity field of a 2D flow past a circular cylinder. Color coding is a common flow visualization technique to map scalar attributes such as velocity magnitude, pressure or temperature to color. The color scale which is used for mapping must be chosen carefully with respect to perceptual differentiation. Figure 3.2b shows a color coding of the corresponding pressure field of the 2D cylinder flow. Volume rendering is a natural extension of color coding to 3D. Special rendering techniques need to be carried out due to occlusion problems [FvDFH96].

3.1.2 Characteristic curve visualization

Characteristic curves are a group of standard characteristics for fluid analysis (see subsection 2.2.1). They are widely applied in fluid experiments and developed as an important topic in flow visualization.

Characteristic curves can be directly visualized through the curve geometries by integrating the corresponding velocity vector fields [HLD*02, SML98]. For an steady flow field, if flow vectors are integrated for a very short time, *streamlets*

are generated. Even though short, streamlets already communicate temporal evolution along the flow. If longer integration is performed *streamlines* are generated. For an unsteady flow field, a *path-line* is visualized by tracing a particle in the fluid flow while a *streak-line* is visualized by tracing a set of particles that have previously passed through a unique point in the domain. A *time-line* can be also visualized by joining the positions of particles released at the same instant time from different insertion points [NHM97].

One important topic of characteristic curve visualization is the optimization of curve distribution. Evenly distributed seed points do not result in evenly spaced characteristic curves. Special strategies need to be considered for the seed locations. Iteratively methods are usually taken to incrementally optimize the curve placements [TB96, VKP00]. Initial collections can be created by placing the characteristic curves either on a regular grid or in some random fashion. The initial placements are optimized gradually by applying several modification such as moving, inserting, deleting, lengthening, shortening, combining on the distributed curves. Certain energy functions based either on space uniformity or flow features are defined to control the modification process. The iterative procedure terminates either when the energy reaches a threshold or when available changes become rare. The final results usually appear to be independent the initialization methods and converge to the desiring placements of the characteristic curves.

3.1.3 Texture based techniques

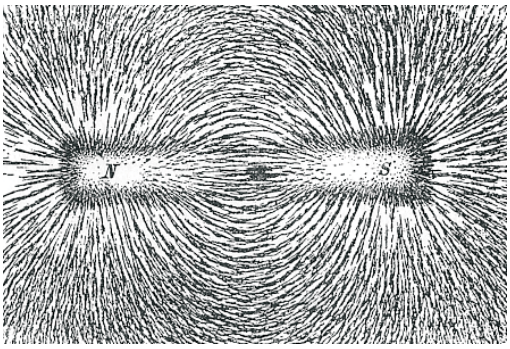

Figure 3.3: Field lines of a magnetic field shown by iron filings around a bar of permanent magnet [BD14].

Characteristic curves are usually invisible to human perceptions. In physics, field lines of a magnetic field are visualized by sprinkling iron scraps into the field as shown in Figure 3.3. It is natural to extend this technique to flow visualization. Textures are filtered along flow fields and characteristic curves are visualized

through the filtered results [LHD*04]. *Line Integral Convolution* (LIC) [CL93] and *spot noise* [vW91] are techniques which map a fluid velocity field into a scalar field which emphasizes the recognition of the behaviors of characteristic curves. They provide full spatial coverage of the vector field and show as many characteristic curves as possible without overlaying them.

The idea of spot noise is to transform a distribution of intensity functions, or spots, in the vector field, into the direction of the flow. Each spot represents a particle moving over a short period of time and results in a streak in the direction of the flow at the position of the spot. One example of spot noise method can be seen in Figure 3.5a.

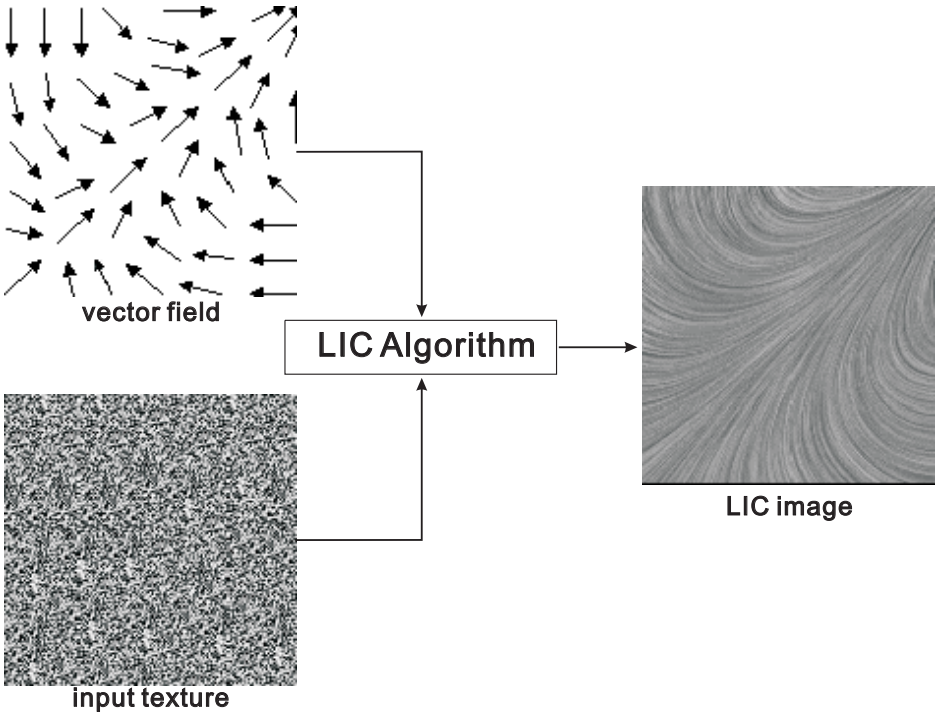

Figure 3.4: The procedure of LIC algorithm.

LIC is one standard technique in flow visualization [CL93]. It imitates the motion blur of substance advection in a fluid whose results describe the substance concentration due to transport behavior of the fluid [SJM96]. LIC uses a noisy input texture and convolutes this into the flow direction. This way the resulting texture changes its color only slightly in flow direction while rapid changes appear in the direction perpendicular to the flow. The procedure is illustrated in Figure 3.4. Given a streamline $\mathbf{s}(l)$, LIC consists of calculating the intensity I for

a pixel located at $\mathbf{x}_0 = \mathbf{s}(0)$ by:

$$I(\mathbf{x}_0) = \int_{-L/2}^{L/2} k(l)\, f(\mathbf{s}(l))\, dl \tag{3.1}$$

where $f(\mathbf{x})$ stands for an input noise texture, k denotes the filter kernel, l is an arc length used to parameterize the streamline curve and L represents the filter kernel length. As proposed already by Cabral and Leedom [CL93], a suitable choice for the convolution kernel is usually a Gaussian type kernel. Although the LIC result may look rather blurry, it gives a good impression of the behavior of the vector field. One example of LIC method of a flow past a box can be seen in Figure 3.5b.

Fast LIC algorithms [SH95a] are introduced to speed up the computation significantly. It uses the fact that most of the information computed to obtain the color of a certain point in the vector field can be reused to compute the color of the adjacent points into flow direction. To do this, it applies convolution on all pixels on a particular streamline and stores all pixels for which convolution is carried out. For untouched pixels, it starts a new streamline from there. Thus fast LIC minimizes the computation of redundant streamlines presented in the original method.

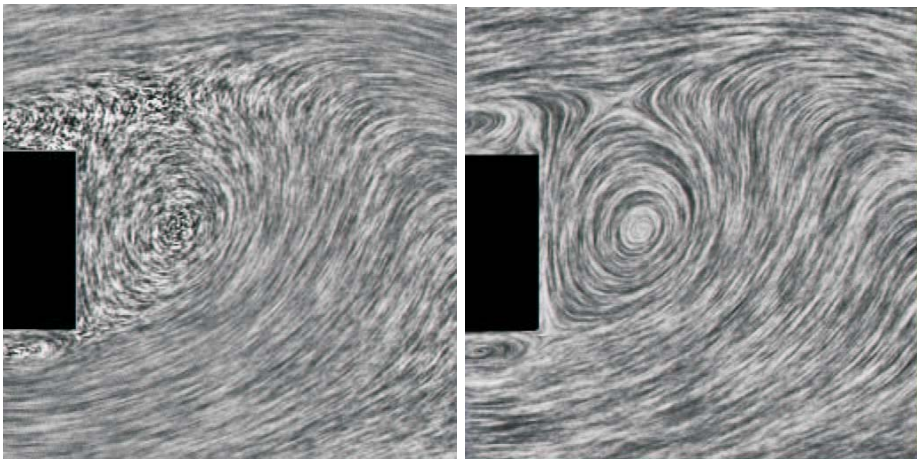

(a) (b)

Figure 3.5: Visualization of flow past a box [LHD*04]: (a) Spot noise method; (b) LIC method.

The difficulty for the extension of LIC to 3D is the efficiency. An efficient 3D LIC algorithm is introduced in [RSHTE99]. The use of transfer functions and geometric clipping objects are essentially important for the perceptual problems associated with 3D. Interactive transfer functions and efficient clipping mechanisms are carried out to substitute the calculation of LIC based on sparse noise textures and display the convenient visual access of interior structures.

3.1.4 PDE based methods

LIC integrates the ordinary differential equation (Equation 2.6) forward and backward in parameterized time at every pixel in the domain. The appropriately Gaussian type kernel is known as the fundamental solution of a heat equation. Thus, line integral convolution is equivalent to solving the heat equation in 1D on a streamline parameterized with respect to arc length. It can be regarded as a discretized streamline diffusion process. For a well posed continuous diffusion problem with similar properties, it leads to some anisotropic diffusion which is controlled by a suitable diffusion matrix.

Anisotropic diffusion is one popular method in image processing [Wei98]. It is also applied to flow visualization to enhance the field line structures along the flow transport [PR99b, BPR00].

For a given vector field $\mathbf{v}(\mathbf{x},t)$, two kinds of diffusion are considered. One is linear diffusion in the direction of the vector field and the other is a Perona Malik type diffusion orthogonal to the field. Then there exists a family of continuous orthogonal mappings $\mathbf{B}(\mathbf{v}) : \Omega \rightarrow SO(n)$ such that $\mathbf{B}(\mathbf{v})\mathbf{v} = \mathbf{e}_0$, where $\{\mathbf{e}_i\}_{i=0,\cdots,n-1}$ is the standard base in $\mathbb{R}^n$. A diffusion matrix $A = A(\mathbf{v}, \nabla\rho_\varepsilon)$ is defined as follows:

$$A(\mathbf{v},d) = \mathbf{B}(\mathbf{v})^T \begin{pmatrix} \alpha(\|\mathbf{v}\|) & \\ & G(d) \end{pmatrix} \mathbf{B}(\mathbf{v})$$

where $\alpha : \mathbb{R}^+ \rightarrow \mathbb{R}^+$ controls the linear diffusion in vector field direction, i.e. along streamlines and edge enhancing diffusion coefficient $G(\cdot)$ acts in the orthogonal directions. Some random noise of an appropriate frequency range is chosen as initial data ρ_0. A visualization of a complex vector field can be achieved by solving the nonlinear parabolic partial differential equation

$$\begin{aligned} \frac{\partial}{\partial t}\rho - div(A(\mathbf{v},\nabla\rho_\varepsilon)\nabla\rho) &= f(\rho) \\ \rho(0,\cdot) &= \rho_0 \end{aligned} \tag{3.2}$$

This obtains a series of images representing the vector field in an intuitive way.

It is expected an almost-everywhere convergence to $\rho(\infty,\cdot) \in \{0,1\}$ due to the choice of the contrast enhancing function $f(\cdot)$.

3.2 Feature Based Flow Visualization Methods

Flow features such as topology, vortex are important characteristics for fluid analysis. For classical flow visualization, feature detection is left to fluid analysts by

investigating the visualization results. Thus it is difficult to treat large and complex data. Feature based flow visualization techniques are promising approaches because of their potential capability to dramatically reduce the complexity of a flow field and extract the important information for fluid analysis [TS03, PVH*03]. Features, such as topologies, vortex structures and shock waves are well extracted and visualized in modern fluid analysis.

3.2.1 Topological methods

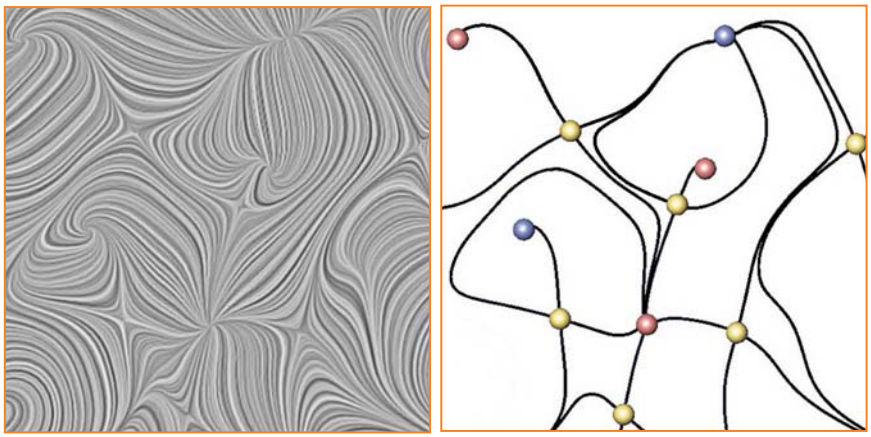

(a) (b)

Figure 3.6: The topological skeleton of a random vector field: (a) A LIC visualization of original field; (b) The corresponding topological skeleton.

Fluid topology are important feature of fluid kinematics (see section 2.2.2). Over the last decade, topological methods have become one standard tool in flow visualization [HH89]. The main idea behind topological methods is to segment a flow field into areas of similar asymptotic behavior. This means to classify each point **x** in the domain with respect to the asymptotic behavior of the characteristic curve through it, i.e., a forward and backward integration starting from **x** with an integration time converging to infinity is considered [PVH*03]. Usually, this integration does not have to be carried out for every point but only for a certain number of starting points of separatrices. The topological segmentation of a flow field is constructed by a *topological skeleton*, which consists of *critical points* and *separatrices*. The separatrices are streamlines distinguishing areas of different flow behavior around a critical point. The topological skeleton is computed in the following step:

- Extracting critical points of a given vector field;

- Classifying the extracted critical points;
- Integrating the separatrices from the saddle critical points.

One example of topological skeleton can be seen in Figure 3.6. Note that in this thesis, a red/ blue/ green/ yellow color coding is used to represent an outflow/ inflow/ center/ saddle flow behavior.

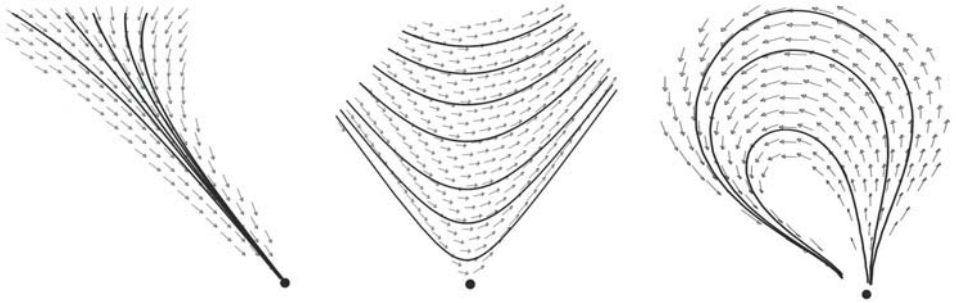

(a) (b) (c)

Figure 3.7: Classification of sectors around a critical point [The01]: (a) A parabolic sector; (b) A hyperbolic sector; (c) An elliptic sector.

Critical points except center and focus have more than one streamline converging to them. The neighborhood separated by two separatrices at a critical point is called a *sector*. All streamlines within the same sector have the same flow behavior. The sectors can be characterized into the following type:

Parabolic sector, shown in Figure 3.7a, where all streamlines originate from the critical point or all streamlines end in the critical point.

Hyperbolic sector, shown in Figure 3.7b, where all streamlines sweep past the critical point, except for two streamlines making the boundaries of the sector. One of these two streamlines ends in the critical point while the other one originates from it.

Elliptic sector, shown in Figure 3.7c, where all streamlines following the arrows begin and end at the critical point.

For 3D vector fields, the topological skeleton contains a number of stream surfaces. These stream surfaces tend to hide each other as well as other topological features and make complex 3D topology visualizations hardly interpretable. *Saddle connectors* are one solution of the occlusion problem [TWHS03]. They represent the separation surfaces as a finite number of stream lines. These stream lines are the intersection curves of the separation surfaces. Saddle connectors start

and end in saddle points of the vector field. Figure 3.8 shows an example of 3D topological skeleton with saddle connectors compared with separation surfaces.

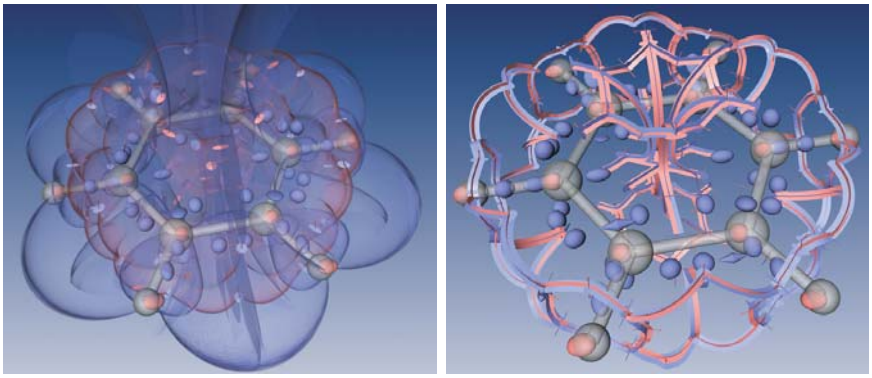

(a) (b)

Figure 3.8: Topological representations of a benzene data set with 184 critical points [TWHS03]: (a) Topological skeleton with separation surfaces; (b) Topological skeleton with saddle connectors.

Topological methods can be also applied to higher order critical points. For 2D vector fields, the procedure is similar. Separatrices start at points with negative index and these points are called higher-order saddles [SHK*97]. For nonlinear behavior, piecewise linear or bilinear interpolation destroys the topology. Clifford algebra is used to compute polynomial approximations in areas with nonlinear behavior [SKMR98]. Topological structures are usually complicated for complex data. A simplification can be made either by discarding small-scale structures [dLvL99] or merging critical points within a prescribed radius into higher order critical points [TSH00].

For 3D higher order critical points, the complete 3D classification of them into areas of similar flow behavior is equivalent to extracting the topological skeleton of an appropriate 2D vector field on a closed convex surface *s*, if each critical point is equipped with an additional bit of information [WTS*05]. An icon is used to replace the topological structures inside *s*. Different levels of topological visualization can be achieved through this simplification. One example can be seen in Figure 3.9 with two different levels of abstraction of the topological representation.

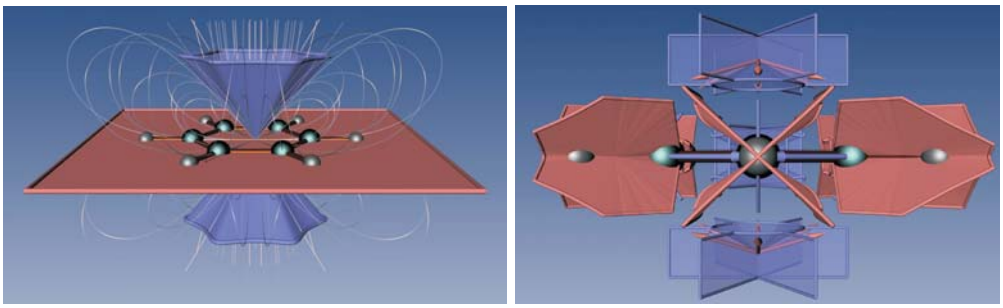

(a) (b)

Figure 3.9: Topological representations of a benzene data set [WTS*05]: (a) High level abstraction of topological representation; (b) Low level abstraction of topological representation.

3.2.2 Vortex extraction method

Among the features of interest, vortices are the most prominent. They play a major role in many research areas due to their wanted or unwanted effects on the flow.

Vortex detection schemes can be classified in two major categories: *vortex region detection* and *vortex core line extraction* [PR99a, PVH*03].

Vortex region detection is based on scalar vortex region quantities that are used to define a vortex as a spatial region where the quantity exhibits a certain value range. The natural method is to find regions with high vorticity (see section 2.2.3). Although a vortex may have a high vorticity magnitude, the converse is not always true [ZBP*91]. *Helicity* is an alternative quantity for vortex region detection [LDS90]. It projects the vorticity onto the velocity $\omega \cdot \mathbf{v}$, which can eliminate the component of vorticity perpendicular to the velocity. Low pressure is another criterion for vortex region detection while swirling flow often swirls around areas of low pressure [Rob91]. λ_2 criterion is one popular technique in vortex region detection [JH95]. Vortex is defined as a region where two eigenvalues of the symmetric matrix $S^2 + \Omega^2$ are negative, where $S = \frac{1}{2}(\nabla \mathbf{v} + \nabla^T \mathbf{v})$ and $\Omega = \frac{1}{2}(\nabla \mathbf{v} - \nabla^T \mathbf{v})$. S and Ω are symmetric and antisymmetric parts of the Jacobian of the vector field. Despite the convincing physical interpretation, the vortex region quantities are of limited applicability in some settings. Isosurfaces or volume rendering are common approaches for visualizing these quantities.

Vortex core line extraction aims at finding line type features that are regarded as centers of vortices. Different approaches exist. One method uses the vortex lines of the vorticity field (see section 2.2.3). Vortex core lines are extracted by seeding vortex lines at critical points with a correction to the pressure minimum in the

plane perpendicular to the vortex core [BS95]. Vortex core line can be also found where vorticity is parallel to velocity and the streamlines of zero torsion [RP96] however in most data sets it does not give the expected features. [SH95b, RP96] consider lines where the flow exhibits a swirling motion around them. They suggest that, in linear vector fields, a vortex core line is located where the Jacobian has one real-valued eigenvector, and this eigenvector is parallel to the flow. While those methods depend on the reference frame, recently a vortex core line extraction method was proposed, which is Galilean invariant, by extracting extremum lines of scalar region quantities [SWH05a], i.e., this method is invariant under adding constant flow fields.

3.2.3 Shock wave extraction method

Shock waves are important features in high speed aerodynamics. Shock waves are characterized by discontinuities in physical flow properties such as pressure, density and velocity. Therefore, shock detection is comparable to edge detection, and similar principles could be used as in image processing [PVH*03, MRV96]. Though physical shocks are very sharp, in numerical simulations, the discontinuities are often smeared over several grid cells, due to errors in the numerical approximation of the fluid dynamics equations. Determining the exact location and structure of shock waves in computed flow solutions is surprisingly difficult.

Shocks are abrupt changes in flow field properties. In particular, the velocity component normal to the shock wave jumps from supersonic to subsonic as flow passes through the shock. Mach Number (see section 2.3.4) is a natural criterion for the detecting of shock waves. All points, where the Mach Number equals one in the flow, are connected. However these results in the sonic surface and does not represent a shock. This can be solved by approximating the density gradient as the shock normal and extracting isosurfaces, whose surface normals corresponds to the density gradient and whose normal Mach Number is equal to one [MRV96, LH99].

Density gradients in the direction of local flow velocity can be used to determine shock locations [PS93]. The first and second derivatives of the density in the direction of the velocity are computed. Zero-level isosurfaces are constructed of the second derivative to find the extrema in the density gradient. Finally, the first derivative is used to select only the maxima, which correspond to shock waves, and discard the minima, which represent expansion waves. This can be done by selecting only positive values of the first derivative. However, a difficulty of this approach is that the second directional derivative equals to one does not necessary mean the shock area and the second derivative also vanishes in smooth regions

with few disturbances, which causes erroneous shock detection. These regions can be excluded by discarding all points where the first derivative is below a certain threshold. The determinant threshold is still difficult for proper visualization of shock waves. An adapted version of this algorithm is presented [MRV96], which uses the normal Mach number to do the exclusion of erroneous shock detection.

3.3 Information Visualization Based Flow Visualization Methods

Information visualization is the art to make the abstract information visible to human perception with the support of computer technologies. The investigated information are mapped to certain geometrical objects and visualized. Practical application of information visualization in computer programs involves selecting, transforming and representing abstract data in a form that facilitates human interaction for exploration and understanding. Important aspects of information visualization are the interactivity and dynamics of visual representation.

The idea of connecting information visualization and scientific visualization approaches is considered to be one of the ”hot topics” in visualization [Joh04, Hau04, Hau06]. The amount of information available to fluid analysts from large-scale simulations, experiments, and data collection is expanded and the variety of information can be overwhelming. The increasing amount and dimensionality of fluid data has made traditional flow visualization methods not well suited for the treatment. It is usually not possible to fully comprehend all the contents of a fluid data set just by looking at one visualization. More advanced analysis technology is necessary so that the full potential of physical information indeed is exploited. With the ability to deal with high-dimensional information, information visualization techniques has become one opportunity for flow visualization.

The highlight of information visualization based flow visualization is the interactive visual analysis which utilizes human-computer interaction to reveal interesting features in the data, based on the interests of the visualization user [DGH03]. Users can interactively specify selected features in the data according to their interests. The brushing mechanism enables the users to interactively mark up interesting data subsets directly in the views. Through this mechanism it is possible that the user can focus on data subsets of special interest. A smooth brush allows for a gradual selection of data subsets so that a smooth transition between selected and not selected data subsets is possible [DH02]. In many cases, users formulate their interest in terms of more than just one attribute. In views which depict the

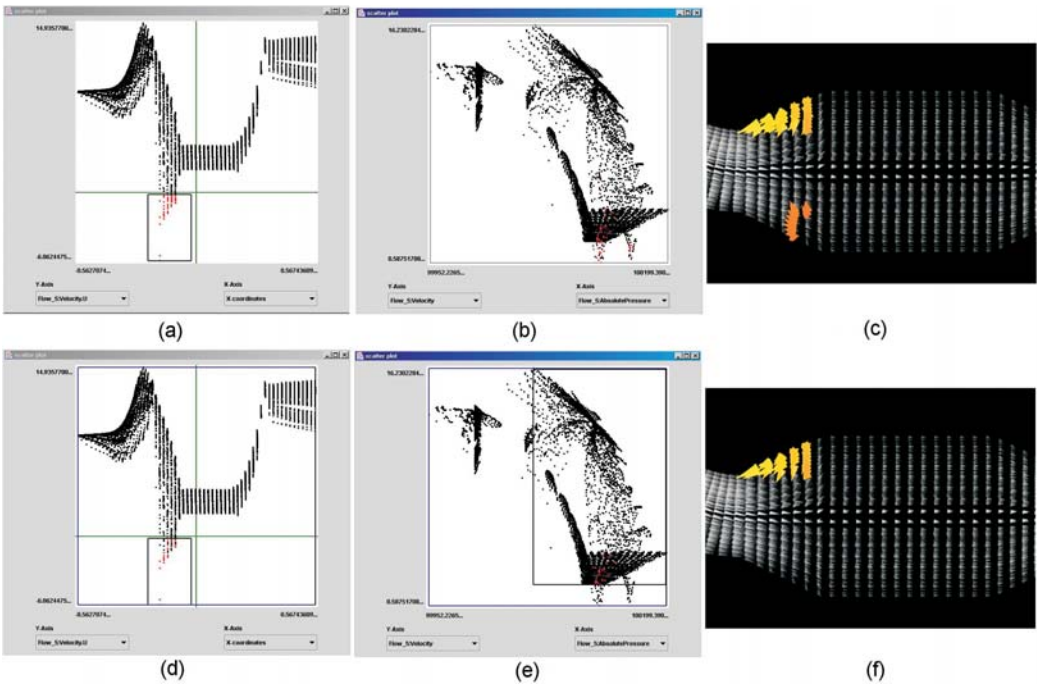

Figure 3.10: Interactive feature specification and refinement of the simulation data of a catalytic converter [DGH03]: First step: (a) Defining back flow region in a catalytic converter in a scatter plot view with the selection of negative x-flow values; (b) Direct linking view of a second scatter plot view for the selected subset; (c) The 3D view. Second step: (e) AND-refinement with a new selection in the second scatter plot view; (d) Back linking of the interaction via feedback visualization to the first scatter plot view; (f) 3D view of the selected back flow region, that exhibits general velocity above a specified threshold.

relations between two or more data attributes, e.g., a scatter plot or the like, also interactive brushing leads to subsetting in relation to the visualized dimensions. Combinations of several brushes through different boolean operations (AND, OR, SUB) in different views are also necessary to capture a specific phenomenon in the flow.

After selecting the interesting subset, a focus+context visualization schema includes both the selected and unselected subset into the visualization pipeline while two different representation forms are applied for the two subsets [Hau04]. The unselected subsets are usually expressed in a reduced visual form, e.g., without being colored and rather transparent. Thereby, it becomes easy to visually relate the selected data subsets to their context. View linking is also of great importance, when brushing is used in conjunction with multiple views. Once a spe-

cific data subset is marked with a brush in one view, all other views of the same data need to be updated instantly. Thereby, visual consistency is maintained between the views. The great potential of this approach is that through the use of multiple linked views, interactive brushing, and focus+context visualization, an explorative analysis of multi-variate features within simulation data is enabled. Figure 3.10 shows an example of focus+context analysis of the simulation data of a catalytic converter [DGH03]. As a first step (first row), all parts of the data, that exhibit back flow, have been selected, defining a feature that spans over two distinct regions in the spatial domain. In the refinement step (second row) a logical AND-combination of the first feature specification with a new selection in a second scatter plot view of the same data is performed. Thereby only those backflow regions of the data are put into focus, which exhibit a general velocity above a specified threshold.

The focus+context analysis can be also extended to time-varying data [DMG*05]. Streamline predicate [SS05] is another information visualization based approach which define, whether a streamline has a given property or not. All streamlines fulfill a streamline predicate are collected in the characteristic set of this predicate.

3.4 Flow Visualization Methods for Dynamical Flow Fields

Due to the complex behavior and particular characteristics of dynamical flow fields, visualization techniques for dynamical flow have achieved special attention within the visualization community. An effective visual analysis of the dynamical behavior of time-dependent flow fields is still a challenging problem in scientific visualization. Although a number of promising approaches has been introduced in recent years, the complexity of dynamical data makes the analysis and the visual representation difficult and partially unsolved. In particular, it also proves to be inherently difficult to actually comprehend the important characteristics of dynamical flow data. Part of the visualization techniques mentioned before in this chapter can be extended to deal with dynamical flow directly. However, special considerations need to be taken for a number of techniques when dealing with time-dependent data set. Particularly, some visualization techniques are specialized only at the dynamical flow behavior. We will discuss some of these algorithms here.

3.4.1 Textured based methods

The wide application of texture based methods comes naturally the demand of an extension to unsteady flow fields. Many approaches have been developed to densely illustrate a dynamical flow field.

An extension of the LIC technique has been contributed to the visualization of unsteady flow fields [FC95]. In contrast with convolving streamlines in the steady flow field, the algorithm convolves forward and backward path-lines originated from each pixel at every time step. An *unsteady flow LIC* (UFLIC) is proposed to efficiently and accurately model the unsteady flow advection [SK97]. A time-accurate value depositing scheme is carried out to accurately model the flow advection, and a successive feed-forward method is applied to maintain the coherence between animation frames. By progressively updating the visualization results in time, UFLIC can produce highly coherent animation frames and accurately trace the dynamic flow movement.

Lagrangian-Eulerian advection (LEA) [JEH01, JEH02] is a hybrid approach which combines the advantages of Lagrangian and Eulerian perspectives. In Lagrangian approach, the trajectory of each particle is computed separately and the time evolution of a collection of particles is displayed by rendering each particle by a glyph, while in Eulerian approach, the property advection equation (see section 6.1) is solved directly and the particle property is viewed as a field which is known for all time at any spatial coordinate. The LEA approach update the coordinates of a dense collection of particles between two successive time steps with a Lagrangian scheme whereas the advection of the particle property is achieved with an Eulerian method. At the beginning of each iteration, a new dense collection of particles is chosen and assigned the property (texture) computed at the end of the previous iteration. LEA does not change the properties of particles along their paths and the particle transport is computed using first order Euler approximation. Weiskopf et al. presented a hardware-based LEA approach which locates the mapping and rendering components of the corresponding visualization pipeline on graphics hardware [WEHE02]. One example of LEA for a shock data set is shown in Figure 3.11a.

Image based flow visualization (IBFV) [vW02, vW03] is another popular extension of texture-based methods to unsteady flow fields. It shows streak-lines of particles injected at various points according to the input structure. IBFV is based on the advection and decay of textures in image space. Each frame of the visualization is defined as a blend between the previous image, warped according to the flow direction, and a number of background images composed of filtered white noise textures. This approach can be mapped directly to standard graph-

ics operations, leading to a fast algorithm. IBFV has also been applied to the visualization of 3D flow [TvW03]. In addition to the noise of original IBFV, empty holes of noise are injected into the 3D fields in order to achieve sparseness and a threshold value is defined to eliminate all close-to-transparent texel values. Weiskopf et at. expanded the range of velocity values of 3D IBFV and advected texel property more than one slice along the z axis of the volume in one animation frame [WE04].

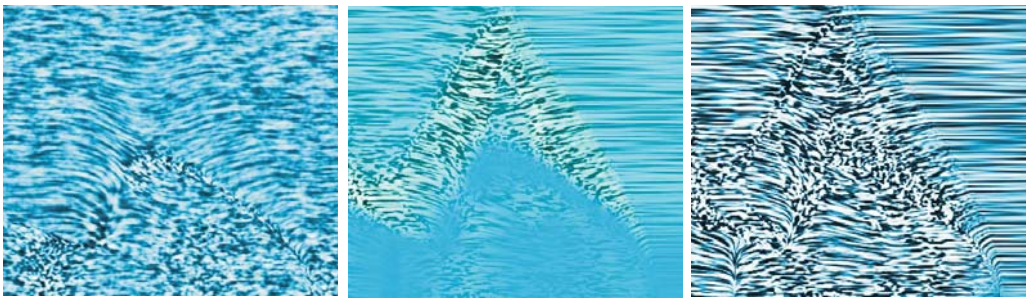

(a) (b) (c)

Figure 3.11: Visualization of a shock data set [WEE03] (a) LEA; (b) UFAC with velocity masking; (c) UFAC without masking.

Laramee et al. presented an approach which generates dense representations of unsteady flow fields on surfaces based on both the LEA and IBFV algorithms [LJH03]. Weiskopf et al. introduced *unsteady flow advection-convolution* (UFAC) as a generic texture-based framework for visualizing 2D time-dependent vector fields [WEE03]. It performs time evolution governed by path-lines, but builds spatial correlation according to instantaneous streamlines whose spatial extent is controlled by the flow unsteadiness. It can be mapped to the SIMD architecture of graphics hardware for an efficient implementation. Space-time coherent dense representations are achieved by a two-step process: construction of continuous trajectories in space-time for temporal coherence, and convolution along another set of paths through the above space-time for spatially correlated patterns. This approach can reproduce other techniques such as LEA, IBFV and UFLIC. One example of UFAC for a shock data set is shown in Figure 3.11b and c.

3.4.2 Streamline oriented topological methods

The main motivation behind topological methods is to segment a vector field into areas of similar flow behavior which is determined by observing the behavior of certain characteristic curves. For time-dependent vector fields, two important

classes of curves exist: streamlines and path-lines. Hence, two different kinds of topologies can be considered: a streamline oriented topology where areas are segmented which show a similar behavior of streamlines, and a path-line oriented topology which does so for path-lines [TWHS04]. Streamline oriented topology of dynamical flow fields can be achieved by tracking the topologies over time, detecting the events and visualizing the evolution of the topologies [TS03].

Critical points are important topological features of a steady vector field. Tracking their locations over time is necessary for capturing the topological behavior of the flow field. To do so, one can either extract and connect the zeros on the faces of an underlying prism cell grid [TSH01, TWSH02], or a feature flow field integration from a number of seed critical points [TS03]. The feature flow field for tracking critical points is a 3D vector field $\mathbf{f}$ which points into the direction where both the direction and magnitude of the vector field remain unchanged. For 2D time-dependent vector field, the feature flow field is defined as follows:

$$\mathbf{f} = \begin{pmatrix} \det(\mathbf{v}_y, \mathbf{v}_t) \\ \det(\mathbf{v}_t, \mathbf{v}_x) \\ \det(\mathbf{v}_x, \mathbf{v}_y) \end{pmatrix} \tag{3.3}$$

The streamline integration of feature flow field starting from a critical point extracts a critical line, which does not depend on the underlying grid.

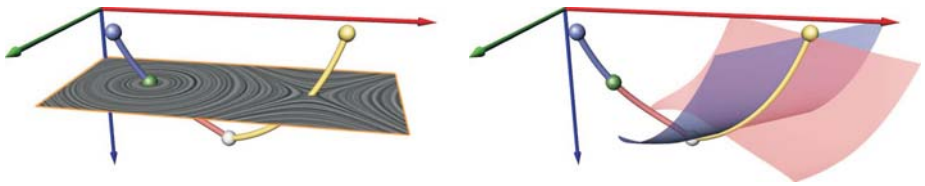

(a) (b)

Figure 3.12: Topological visualization of a simple 2D time-dependent vector field consisting of sink, source, saddle, fold and Hopf bifurcation [TWHS04]: (a) Critical lines and LIC plane through a Hopf bifurcation; (b) Separation surfaces created by the moving saddle.

For the tracked critical points, the local bifurcations are detected here. A *fold bifurcation* appears if at a certain time t a critical point appears and in the same moment splits up to a saddle and source/ sink/ center or vice versa [Bak91]. Another important class of local bifurcations are *Hopf bifurcations* which denote locations where a sink becomes a source or vice versa. Thus, they denote the location of a center, i.e. a critical point with a vanishing divergence and a positive Jacobian. Figure 3.12a shows a simple example of the critical lines and the fold and Hopf

bifurcations. The Hopf bifurcation is shown as a small green sphere and the fold bifurcations are shown as gray sphere.

Note that in all figures throughout this thesis the coordinate system is shown as follows: red/ green/ blue coordinate axes denote the (x, y, z) domain, specially, the blue axis also shows the temporal domain for 2D time-dependent fields.

Part of the topological skeleton of a vector field are the separation curves starting from saddle points. While the saddle moves over time, their sweepings form 4 stream surfaces dividing s into areas of different flow behavior. Figure 3.12b show an example of separation surfaces of a saddle type critical line.

Critical point tracking can be also extended to deal with 3D time-dependent vector field [TS03, GTS04].

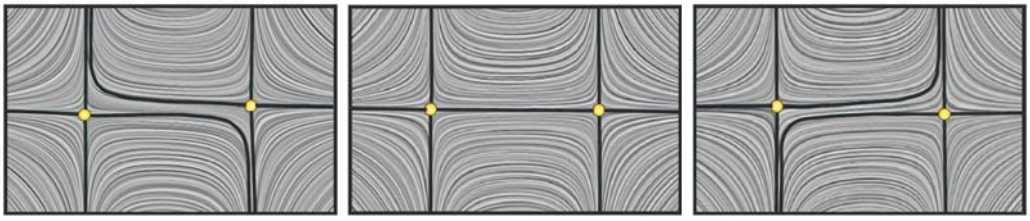

(a) (b) (c)

Figure 3.13: Saddle connection bifurcation [TWHS04]: (a) Shortly before; (b) The event; (c) Shortly after.

Saddle connections are global bifurcations which appear when two separatrices starting from saddle points collapse, i.e. when a separatrix of one saddle ends in another saddle [TWHS04]. Figure 3.13 illustrates an example. A special case of saddle connections is the so-called periodic *blue sky bifurcation* [AS92] where two separatrices of the same saddle collapse. Saddle connections of 2D time-dependent vector fields can be extracted by making an adaption of the saddle connectors approach [TWHS03] which are the intersection curves of the separation surfaces of a 3D vector field starting in the outflow and inflow planes of the saddle points. The basic idea is to numerically integrate two separation surfaces until an intersection is found. After some refinement, a streamline is integrated from the intersection point both in forward and backward direction.

Closed streamlines are another global topological features which evolve over time. Several types can occur: a closed streamline may appear or disappear, or two closed streamlines may collapse and disappear. The last case is called *cyclic fold bifurcation* and is illustrated in Figure 3.14. Closed streamlines can be extracted in different time levels, and corresponding streamlines in adjacent time levels are

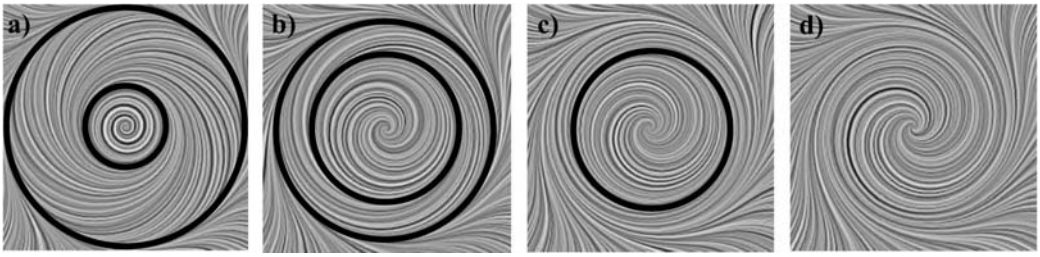

Figure 3.14: Cyclic fold bifurcation [TWHS04]: (a),(b) Two closed streamlines move towards each other; (c) Merge; (d) Disappear.

connected [TSH01]. Following the idea of feature flow fields, closed streamlines can be also tracked by an modification of saddle connector approach [TWHS04].

3.4.3 Path-line oriented topological methods

Constructing a path-line oriented topology means to segment path-lines into regions of different flow behaviors. A path-line oriented segmentation of the flow domain is made based on local properties of path-lines [TWHS04].

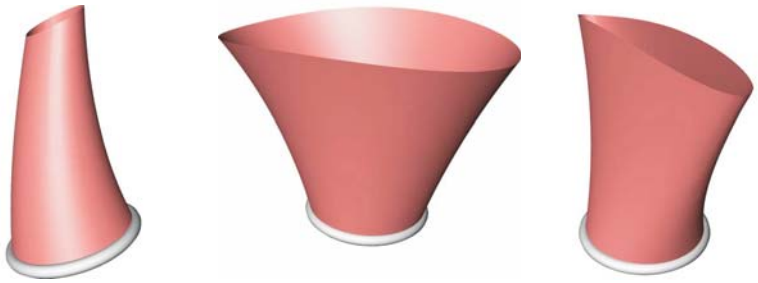

(a) (b) (c)

Figure 3.15: Behavior of path-line starting on a circle $\mathbf{k}$ around $\mathbf{x}_0$ [TWHS04]: (a) Attracting; (b) Repelling; (c) Saddle-like.

A 3D auxiliary vector field $\mathbf{p} = (u, v, 1)^T$ is constructed by adding one additional component 1 and the local properties of $\mathbf{p}$ are exploited to get a segmentation of $\mathbf{p}$. The streamlines of $\mathbf{p}$ correspond to the path-lines of original time-dependent vector field $\mathbf{v}$. Pure directional properties of the streamlines of $\mathbf{p}$ are considered since the topological skeleton depends only on the directions of the streamlines. Thus, the domain can be segmented into areas of attracting, repelling, or saddle like behavior of the streamlines of $\mathbf{p}$. Consider a point $\mathbf{x}_0$ with its corresponding

vector $\mathbf{p}(\mathbf{x}_0)$ defining a streamline l_0 in $\mathbf{p}$ starting at $\mathbf{x}_0$. Considering a small circle $\mathbf{k}_0$ around $\mathbf{x}_0$ in the plane perpendicular to $\mathbf{p}(\mathbf{x}_0)$, there are three possible stable cases for all streamlines l in $\mathbf{p}$ starting in $\mathbf{k}_0$, concerning their convergence/ divergence behavior towards l_0:

- All l converge towards l_0 under forward integration.
- All l move away from l_0 under forward integration.
- Streamlines with both converging and diverging behavior exist (saddle-like behavior).

Figure 3.15 illustrates these three cases.

Contrary to the streamline oriented topology, the path-line oriented topology is not invariant under scalings of $\mathbf{v}$. The path-lines of two vector fields $\mathbf{v}(\mathbf{x},t)$ and $c \cdot \mathbf{v}(\mathbf{x},t)$ with $c > 0$ and $c \neq 1$ differ. The factor c influences the impact of the temporal changes with respect to the spatial changes. For large c, the flow is dominated by the spatial changes. For $c \to +\infty$, the streamlines of $\mathbf{p}$ converge to the streamlines of $\mathbf{v}$.

The path-line oriented topology introduced above uses the concept of topology in a slightly different way than usually done. The classical understanding of topology is to observe how streamlines behave under an integration until infinity, while this method only considers local properties of the path-lines.

3.4.4 Lagrangian coherent structure

Lagrangian coherent structure (LCS) is one highlight in dynamical flow analysis. It depicts the transport barriers of the underlying flow processes. Early works focuse on the study of uniformly hyperbolic path-lines [PH99]. Haller has pioneered the introduction of the FTLE field to characterize LCS [Hal00, HY00, Hal01]. He also proposed to characterize LCSs with the quantities of particle trajectories, i. e. path-lines [Hal01, Hal02]. A finite-time Lyapunov exponent field (FTLE), which is a scalar attribute field of finite-time path-lines, contains information about how much particles separate after a given interval of time. LCSs are extracted from the ridges of the FTLE fields. These structures typically represent separatrices which divide the flow into dynamically distinct regions.

The traditional Lyapunov exponent quantifies the asymptotic behavior of infinitesimally close particles in a dynamical system [Lia66]. The Lyapunov exponent of a finite-time path-line is a finite-time average of the maximum expansion rate for a pair of particles advected in the flow. Consider a perturbed point $\mathbf{x}_0' = \mathbf{x} + \delta\mathbf{x}_0$

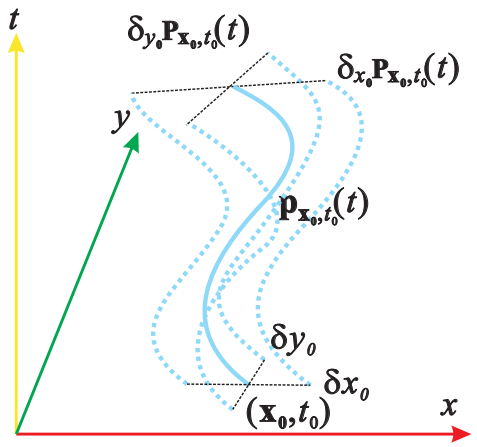

Figure 3.16: Lyapunov exponent of finite-time path-line.

as shown in Fig. 3.16, where $\delta\mathbf{x}_0$ is infinitesimal. After a time interval t, this perturbation becomes $\delta_{\mathbf{x}_0}\mathbf{p}_{\mathbf{x}_0,t_0}(t) = \mathbf{p}_{\mathbf{x}'_0,t_0}(t) - \mathbf{p}_{\mathbf{x}_0,t_0}(t)$. A linear flow map $A = \nabla_{\mathbf{x}_0}\mathbf{p}_{\mathbf{x}_0,t_0}(t)$ is computed to characterize the stretching gradient of the perturbation. The Maximum stretching occurs when $\delta\mathbf{x}_0$ is chosen such that it is aligned with the eigenvector associated with the maximum eigenvalue of A^TA. The maximum stretching is correspondingly the largest eigenvalue of A^TA. Through logarithm and normalization with the absolute advection time t, the definition of FTLE comes to

$$\delta_0^t(\mathbf{x}) = \frac{log(\sqrt{\lambda_{max}(A^TA)})}{t} \tag{3.4}$$

A FTLE field of a dynamical flow provides an effective tool for characterizing LCSs. Large FTLE values for forward advection correspond to unstable manifolds while large FTLE values for backward advection correspond to stable manifolds. For a FTLE field $\delta_{t_0}^t(\mathbf{x})$, LCSs are defined as *ridges* of the field [Hal00]. [SLM05] provided a formal discussion of the theory of FTLE fields and LCSs. [GLT*07] used graphics hardware for the direct visualization of FTLE and [SP07a, GGTH07] have proposed efficient algorithms to compute LCSs. [SP07b] compared the LCSs with the traditional vector field topologies.

3.5 Conclusion

In this chapter, we recalled the common flow visualization techniques from the perspective of fluid analysis. Ordinary methods visualize the flow properties and patterns which are well explored in experimental flow visualization. Feature based

techniques extract the important features for fluid analysts while the information visualization based approaches utilize the expertise support to explore the interesting features. Special attentions were payed to the visualization techniques of dynamic flow fields.

Chapter 4

Path-line Oriented Topological Visualization

The main idea behind topological methods is to segment a vector field into areas of similar asymptotic behavior. This means to classify each point $\mathbf{x}$ in the domain with respect to the asymptotic behavior of the characteristic curve through it, i.e., a forward and backward integration starting from $\mathbf{x}$ with an integration time converging to infinity is considered. Usually, this integration does not have to be carried out for every point but only for a certain number of starting points of separatrices.

For time-dependent vector fields there exists a number of relevant characteristic curves, such as streamlines, path-lines, streak-lines (see section 2.2.1). Among them, streamlines and path-lines have the uniqueness property: through each point in the space-time domain there is exactly one streamline and one path-line passing through. This gives that two different kinds of topologies can be considered: a streamline oriented topology segmenting areas of similar streamline behavior, and a path-line oriented topology which does so for path-lines. Extracting a streamline oriented topology ends up in tracking critical points and considering certain bifurcations. A number of approaches for this exist (see section 3.4.2).

Path-lines are important characteristic curves in time-dependent vector fields because they describe the path of massless particles in a flow. Hence, a path-line oriented segmentation gives a different kind of insight into the vector field data with the streamlines. Unfortunately, path-line oriented topological methods rarely exist because a strong restriction applies: since path-lines move constantly forward in time and real life data sets are usually given only in a fixed time interval,

a path-line integration until infinity cannot be carried out: the integration stops when the maximal time of the given data set is reached. Therefore, a topological segmentation based on the asymptotic behavior of path-lines usually does not exist. The approach in section 3.4.3 [TWHS04] avoid this problem by considering local topological behavior. There, instead of the asymptotic behaviors of path-lines, only their local behavior was considered for segmentation. This segmentation delivers regions of locally attracting, repelling or saddle-like behaviors of path-lines. However, it is not a topological one in the classical sense because it does not incorporate any asymptotic behaviors of path-lines.

In this chapter, we will present an approach to topologically analyzing and visualizing the asymptotic behavior of path-lines [STW*06]. We achieve this by restricting ourselves to *periodic* time-dependent vector fields. We think that this class of vector fields deserves special consideration since many numerical flow simulations are actually periodic (or pseudo-periodic) flows. Examples of the visual analysis of periodic flow fields (but not a topological analysis of path-lines) can be found in [TWHS04, TSW*05].

For periodic vector fields, the time-domain is not restricted to a certain interval but can be extended to any time by periodically repeating the given field. Hence, an analysis of the asymptotic behavior of path-lines becomes possible.

4.1 Streamline and Path-line Oriented Topology

Here, we restrict our consideration to 2D time-dependent flow fields. In section 3.4, the streamline and path-line oriented topology are discussed. We define these problems in a more formalized way for our application in 2D unsteady flow fields. Given is a 2D time-dependent velocity field $\mathbf{v}(\mathbf{x},t)$ in the spacial-temporal domain $D = [x_{min}, x_{max}] \times [y_{min}, y_{max}] \times [t_{min}, t_{max}]$. Then $\mathbf{x}$ describes the spatial component and t is the temporal component. In order to distinguish streamlines and path-lines, we derive two 3D vector fields $\mathbf{s}$ and $\mathbf{p}$ by adding a constant component to $\mathbf{v}$ (see also section 3.4.3):

$$\mathbf{s}(\mathbf{x},t) = \begin{pmatrix} \mathbf{v}(\mathbf{x},t) \\ 0 \end{pmatrix} \quad , \quad \mathbf{p}(\mathbf{x},t) = \begin{pmatrix} \mathbf{v}(\mathbf{x},t) \\ 1 \end{pmatrix}. \tag{4.1}$$

This way the streamlines of $\mathbf{s}$ correspond to the streamlines of $\mathbf{v}$, while the streamlines of $\mathbf{p}$ correspond to the path-lines of $\mathbf{v}$. Therefore, a path-line oriented topological segmentation of $\mathbf{v}$ corresponds to a segmentation of the streamlines of

p. Unfortunately, such a segmentation of **p** cannot be made by applying conventional topological methods of 3D vector fields because an asymptotic analysis of a streamline in **p** is impossible: every streamline integration in **p** is guaranteed to leave the spatial-temporal domain D after a while, making it impossible to consider the asymptotic behavior. This restriction does not hold any more when moving forward to periodic vector fields.

4.2 Periodic Vector Fields

If **v** is a periodic-in-time vector field, it is sufficient to consider one period which can be repeated as often as necessary. We assume that **v** describes one period, which means that $\mathbf{v}(\mathbf{x}, t_{min}) = \mathbf{v}(\mathbf{x}, t_{max})$. Then we can assume **v** to be defined in the whole spatial-temporal domain D by setting

$$\mathbf{v}(\mathbf{x}, t) = \mathbf{v}(\mathbf{x},\ t + k\,\Delta t)$$

where $\Delta t = (t_{max} - t_{min})$ and k is an integer chosen such that $t_{min} \leq t + k\,\Delta t < t_{max}$. In a similar way, **p** is defined over D.

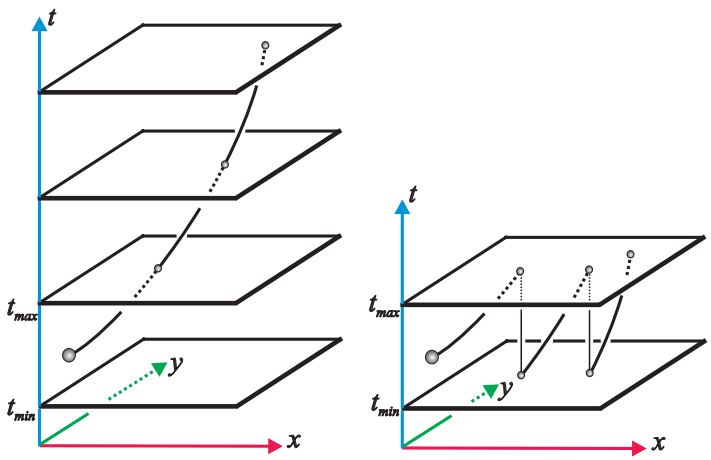

Figure 4.1: Two equivalent approaches of a streamline integration in a periodic field **p**: (a) In the unbounded time-domain; (b) Periodically continued in the time-domain $[t_{min}, t_{max}]$.

In order to integrate a streamline in the periodic field **p** (which corresponds to a path-line of **v**), two equivalent strategies can be applied:

- The integration is done over the unbounded time-domain as illustrated in figure 4.1a.
- If the integration approaches a point $(\mathbf{x}, t_{max})$, it is mapped to $(\mathbf{x}, t_{min})$. From there, the integration is continued until t_{max} is reached again. Figure 4.1b illustrates this.

Our approach to do a topological segmentation of path-lines starts with picking a certain reference time τ with $t_{min} \leq \tau < t_{max}$. We aim at a segmentation of the asymptotic behavior of all path-lines starting at the time τ. To do so, two 2D maps $\mathbf{m}_\tau(\mathbf{x})$ and $\bar{\mathbf{m}}_\tau(\mathbf{x})$ are constructed. For $\mathbf{m}_\tau(\mathbf{x})$, we start a forward integration of $\mathbf{p}$ from $(\mathbf{x}, \tau)$ until one of the following cases occurs:

1. The integration reaches the time level $\tau + \Delta t$, i.e. comes to a certain point $(\mathbf{x}_f, \tau + \Delta t)$. Then we set $\mathbf{m}_\tau(\mathbf{x}) = \mathbf{x}_f$.
2. The integration leaves the spatial domain before reaching the level $\tau + \Delta t$. In this case we mark $\mathbf{m}_\tau(\mathbf{x})$ as undefined.

In a similar way we compute $\bar{\mathbf{m}}_\tau(\mathbf{x})$ by starting a backward integration of $\mathbf{p}$ from $(\mathbf{x}, \tau)$ until the time level $\tau - \Delta t$ is reached at a point $(\mathbf{x}_b, \tau - \Delta t)$, or until the integration leaves the spatial domain. In the first case, we set $\bar{\mathbf{m}}_\tau(\mathbf{x}) = \mathbf{x}_b$, in the second case $\bar{\mathbf{m}}_\tau(\mathbf{x})$ is undefined. Figure 4.2a illustrates the definition of $\mathbf{m}_\tau(\mathbf{x})$ and $\bar{\mathbf{m}}_\tau(\mathbf{x})$.

Instead of the definition of the maps $\mathbf{m}_\tau(\mathbf{x})$ and $\bar{\mathbf{m}}_\tau(\mathbf{x})$ described above, we can also use a vector-oriented description of the map:

$$\mathbf{q}_\tau(\mathbf{x}) = \mathbf{m}_\tau(\mathbf{x}) - \mathbf{x} \quad , \quad \bar{\mathbf{q}}_\tau(\mathbf{x}) = \bar{\mathbf{m}}_\tau(\mathbf{x}) - \mathbf{x} \tag{4.2}$$

Since $\mathbf{m}_\tau(\mathbf{x})$ and $\mathbf{q}_\tau(\mathbf{x})$ can be easily transformed into each other, we will switch between both formulations in order to simplify the notation of our approach. Note that in general $\bar{\mathbf{q}}_\tau \neq -\mathbf{q}_\tau$.

The maps $\mathbf{m}_\tau$ and $\bar{\mathbf{m}}_\tau$ can be interpreted as 2D Poincaré maps [LKG98]. In order to analyze the asymptotic behavior of a path-line starting from $(\mathbf{x}, \tau)$ in forward direction, we do not have to integrate $\mathbf{p}$ any more but can restrict ourselves to a sequence of maps of $\mathbf{m}_\tau(\mathbf{x})$:

$$\mathbf{x}_0 = \mathbf{x} \quad , \quad \mathbf{x}_{i+1} = \mathbf{m}_\tau(\mathbf{x}_i) \tag{4.3}$$

and considering the asymptotic behavior for $i \to \infty$. Figure 4.2b illustrates this. A similar statement holds for the backward integration of $\mathbf{p}$ and a sequence of maps of $\bar{\mathbf{m}}_\tau$. Note that Equation 4.3 is equivalent to a numerical Euler integration of $\mathbf{q}_\tau$ with the step size 1: $\mathbf{x}_{i+1} = \mathbf{x}_i + 1\,\mathbf{q}_\tau(\mathbf{x}_i)$.

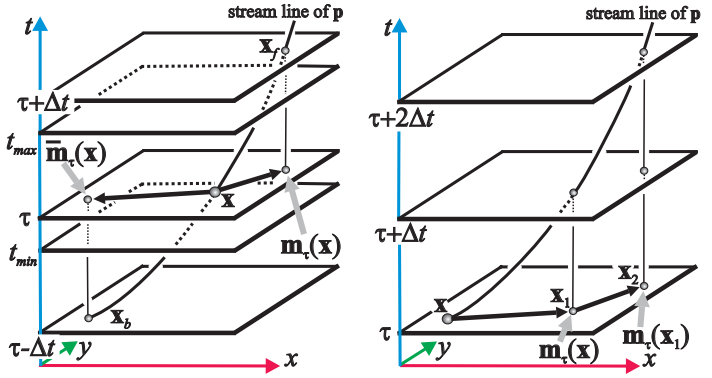

(a) (b)

Figure 4.2: (a) The definition of $\mathbf{m}_\tau(\mathbf{x})$ and $\bar{\mathbf{m}}_\tau(\mathbf{x})$; (b) A continuous forward integration of $\mathbf{p}$ corresponds to a discrete integration of $\mathbf{m}_\tau(\mathbf{x})$.

Both Poincaré maps $\mathbf{m}_\tau$ and $\bar{\mathbf{m}}_\tau$ can be considered as discrete invertible dynamical systems: there are no two distinct points which are mapped to the same point by $\mathbf{m}_\tau$ or $\bar{\mathbf{m}}_\tau$. In other words: $\mathbf{m}_\tau$ and $\bar{\mathbf{m}}_\tau$ are inverse to each other:

$$\bar{\mathbf{m}}_\tau(\mathbf{m}_\tau(\mathbf{x})) = \mathbf{m}_\tau(\bar{\mathbf{m}}_\tau(\mathbf{x})) = \mathbf{x} \tag{4.4}$$

for every $\mathbf{x}$ where both $\mathbf{m}_\tau$ and $\bar{\mathbf{m}}_\tau$ are defined.

A special role in the further analysis of the path-lines play isolated fix points of $\mathbf{m}_\tau$ and $\bar{\mathbf{m}}_\tau$, i.e., points $\mathbf{x}$ with $\mathbf{m}_\tau(\mathbf{x}) = \bar{\mathbf{m}}_\tau(\mathbf{x}) = \mathbf{x}$. (This is equivalent to critical points in $\mathbf{q}_\tau$, $\bar{\mathbf{q}}_\tau$.) The fix points of $\mathbf{m}_\tau$ and $\bar{\mathbf{m}}_\tau$ correspond to certain path-lines which we call *critical path-lines* because they have a well-defined asymptotic behavior: they repeat the same spatial cycle in every time period. Figure 4.3a gives an illustration.

The critical path-lines will be the basis of our topological segmentation: we classify path-lines whether they converge to a critical path-line in forward or backward integration respectively. Similar to critical points of a vector field, critical path-lines can act as sources, sinks, or saddles.

Note that more critical path-lines may occur when considering two or more time periods. Such a critical path-line over n time periods corresponds to a fix point of the map $\mathbf{m}_\tau{}^n$. Figure 4.3b illustrates an example for $n = 2$. However, in our applications we only considered simple (one period) critical path-lines.

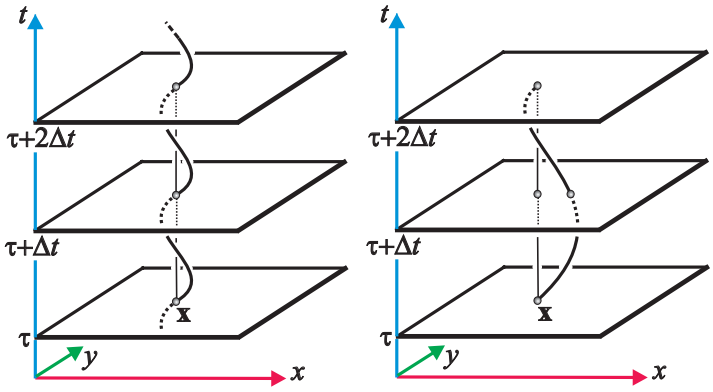

(a) (b)

Figure 4.3: (a) A critical path-line corresponds to fix points in $\mathbf{m}_\tau$, $\bar{\mathbf{m}}_\tau$. (b) Critical path-line over two time periods.

4.3 Topological Segmentation of 2D Poincaré Maps

The segmentation of areas of similar path-line behavior corresponds to the topological segmentation of the 2D Poincaré maps $\mathbf{m}_\tau$ and $\bar{\mathbf{m}}_\tau$ respectively. Critical path-lines in $\mathbf{p}$ correspond to fix points in $\mathbf{m}_\tau$ and $\bar{\mathbf{m}}_\tau$. They may act as sources, sinks or saddle path-lines building α- and ω-basins in D. In this section we show how to find this segmentation by a topological analysis of $\mathbf{m}_\tau$ and $\bar{\mathbf{m}}_\tau$. Since $\mathbf{m}_\tau$ and $\bar{\mathbf{m}}_\tau$ can be considered as discrete dynamical systems, classical topological vector field approaches fail to give the correct segmentation because they reflect continuous dynamical systems. In particular, the following points apply:

1. Although $\mathbf{p}$ is continuous, both $\mathbf{m}_\tau$ and $\bar{\mathbf{m}}_\tau$ may have pseudo-discontinuities, this will be discussed further in section 4.4.1.

2. The classification of the fix points of $\mathbf{m}_\tau$ and $\bar{\mathbf{m}}_\tau$ in sources, sinks and saddles can be obtained by an eigen-analysis of the Jabobians of $\mathbf{m}_\tau$ and $\bar{\mathbf{m}}_\tau$ but differers from the classification for smooth vector fields [Tso92, Löf98].

3. The separating structures of the basins are generally not streamlines of the vector fields $\mathbf{q}_\tau$ and $\bar{\mathbf{q}}_\tau$. Because of this, they can intersect in non-critical points of $\mathbf{q}_\tau$ and $\bar{\mathbf{q}}_\tau$.

Critical points of discrete non-invertible dynamical systems and their corresponding basins have been extracted and visualized in [BMH01, HMBG01], ending up in non-connected or even fractal-shaped basins. However, for our purposes the

approach simplifies because $\mathbf{m}_\tau$ and $\bar{\mathbf{m}}_\tau$ are invertible.

4.3.1 Classifying critical points

The classification of a first order critical point in a discrete dynamical system is well-understood [Tso92, Löf98] and differs from the classification of a continuous system. Given a first order approximation of $\mathbf{m}_\tau$

$$\mathbf{m}_\tau(\mathbf{x}) = \mathbf{J}\,\mathbf{x} \tag{4.5}$$

where $\mathbf{J}$ is the 2×2 Jacobian matrix, $\mathbf{m}_\tau$ has a fix point at $(0,0)$. To capture the asymptotic converging/diverging behavior of the sequence of Equation 4.3 for $i \to \infty$ in a vicinity of $(0,0)$, we consider the eigenvales λ_1, λ_2 and the corresponding eigenvectors $\mathbf{e}_1$, $\mathbf{e}_2$ of $\mathbf{J}$. Based on the eigenvalues, we get the following classification

$$\begin{aligned}
\|\lambda_j\| > 1 &\quad\rightarrow\quad \text{repelling behavior} \\
\|\lambda_j\| < 1 &\quad\rightarrow\quad \text{attracting behavior} \\
\mathrm{Im}(\lambda_j) \neq 0 &\quad\rightarrow\quad \text{rotating behavior} \\
\mathrm{Im}(\lambda_j) = 0\,,\ \mathrm{Re}(\lambda_j) < 0 &\quad\rightarrow\quad \text{alternating behavior} \\
\mathrm{Im}(\lambda_j) = 0\,,\ \mathrm{Re}(\lambda_j) > 0 &\quad\rightarrow\quad \text{non-alternating behavior}
\end{aligned}$$

for $j = 1,2$. Figure 4.4 illustrates some examples of sources and sinks of $\mathbf{m}_\tau$. There, in order to describe the linear approximation $\mathbf{m}_\tau$, we show three points and their assigned vectors $\mathbf{q}_\tau$: the fix point $\mathbf{x}_0$, and two more points $\mathbf{x}_1$, $\mathbf{x}_2$ in the direction of the two eigenvectors of $\mathbf{J}$. The circles around the fix points denote whether the map moves closer or further away from the fix point: if the two arrows of $\mathbf{q}_\tau$ point inside the circle, an attracting behavior of $\mathbf{q}_\tau$ is present.

If $\mathbf{m}_\tau$ is linear as given in Equation 4.5, then $\bar{\mathbf{m}}_\tau$ is linear as well:

$$\bar{\mathbf{m}}_\tau(\mathbf{x}) = \mathbf{J}^{-1}\,\mathbf{x}. \tag{4.6}$$

Since the eigenvalues/eigenvectors of $\mathbf{J}^{-1}$ are $1/\lambda_j$, $\mathbf{e}_j$ for $j = 1,2$, there are the following correlations between $\mathbf{m}_\tau$ and $\bar{\mathbf{m}}_\tau$:

behavior of $\mathbf{m}_\tau$	behavior of $\bar{\mathbf{m}}_\tau$
repelling	attracting
attracting	repelling
saddle	saddle
alternating	alternating
non-alternating	non-alternating
rotating	rotating

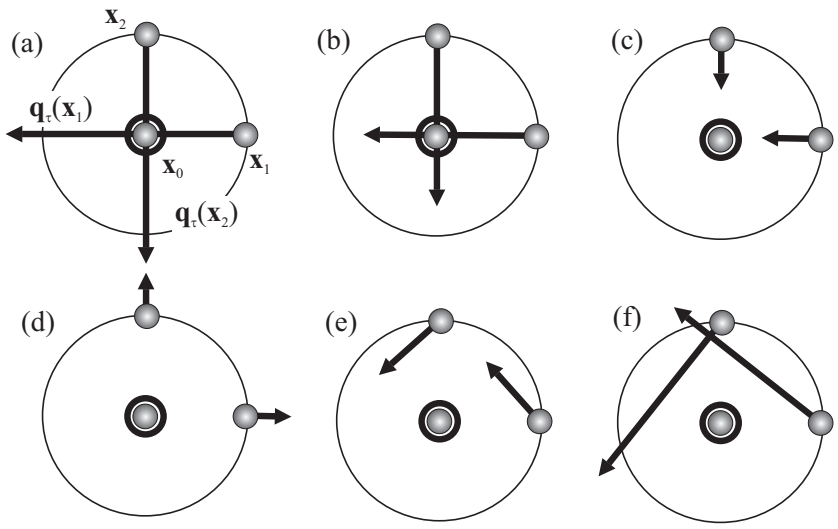

Figure 4.4: Classification of sources/ sinks of $\mathbf{m}_\tau$: (a) repelling/ alternating; (b) attracting/ alternating; (c) attracting/ non-alternating (d) repelling/ non-alternating; (e) attracting/ rotating; (f) repelling/ rotating.

4.3.2 Getting the topological sectors

For continuous dynamical systems, the different basins are separated by streamlines starting from saddle points. However, such a streamline integration does not exist for the discrete systems $\mathbf{m}_\tau$ and $\bar{\mathbf{m}}_\tau$. Therefore we apply a point-wise approach: for every point $\mathbf{x}$ in the spatial domain, we integrate $\mathbf{m}_\tau$ using Equation 4.3 until one of the following conditions is fulfilled:

- $\mathbf{x}_i$ comes close to a fix point of $\mathbf{m}_\tau$;
- $\mathbf{x}_i$ leaves the spatial domain;
- i exceeds a certain threshold of maximal iterations.

In the first case we assume $\mathbf{x}$ to be part of the basin of the fix point. This means that the path-line starting at $(\mathbf{x}, \tau)$ converges to a critical path-line under forward integration. In the second case, the path-line is known to leaving the domain under forward integration. In the last case, $\mathbf{x}$ is marked as unknown because we could not get a statement about the asymptotic behavior of the path-line starting from $(\mathbf{x}, t)$.

4.4 Topological Separation Surface Extraction

The above mentioned topological segmentation classify every point in the spatial-temporal domain according to the asymptotic behavior of path-lines. Sometimes, people are interested in the topological structures of the whole domain. It is time-consuming for the computation of every considered time. The separation surfaces of the general path-line oriented topological structure are desired in these situations.

4.4.1 Difficulties of separation surface extraction

It is not so easy to generate the separation surfaces for the topological structures of periodic 2D time-dependent vector fields. The discrete integration and the pseudo discontinuity of a Poincaré map are two key problems for classical topological method when extracting separation surfaces.

Discrete dynamic systems

Both Poincaré maps $\mathbf{m}_\tau$ and $\bar{\mathbf{m}}_\tau$ can be considered as discrete invertible dynamical systems (see also section 4.3). As shown in Equation 4.3, the integration of Poincaré maps is equivalent to a numerical Euler integration of $\mathbf{q}_\tau$ with step size 1: $\mathbf{x}_{i+1} = \mathbf{x}_i + 1\,\mathbf{q}_\tau(\mathbf{x}_i)$.

For discrete dynamical systems, classical topological vector field approaches fail to give the correct segmentation because they reflect continuous dynamical systems. For continuous dynamical systems, the different basins are separated by streamlines starting from saddle points. However, such a streamline integration does not exist for the discrete systems $\mathbf{m}_\tau$ and $\bar{\mathbf{m}}_\tau$.

Note that the topology of discrete dynamical systems can get a lot more complicated, even for lower dimensions, when compared to the continuous case.

Pseudo discontinuity

Although $\mathbf{v}$ is continuous, both $\mathbf{m}_\tau$ and $\bar{\mathbf{m}}_\tau$ may have pseudo discontinuities, which means that $\mathbf{m}_\tau$ and $\bar{\mathbf{m}}_\tau$ are still continuous mathematically, but they may have areas with tremendous large gradient, which appear as discontinuities for discrete treatment. To see this point, we consider the example of a steady 2D vector field $\mathbf{v}(\mathbf{x}) = \mathbf{v}(\mathbf{x},t)$ which can also be considered as as periodic time-depending

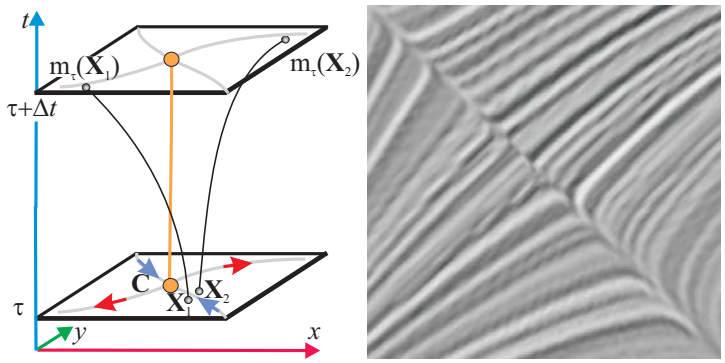

(a) (b)

Figure 4.5: Pseudo discontinuities in $\mathbf{m}_\tau$: (a) If $\mathbf{x}_1$ and $\mathbf{x}_2$ are close but at different sides of a separatrix of $\mathbf{v}(\mathbf{x}) = \mathbf{v}(\mathbf{x},t)$, $\mathbf{m}_\tau$ has too large changes that it is impossible for discrete numerical method to deal with it though it is still continuous; (b) The pseudo discontinuity in corresponding Poincaré map.

vector field. Setting a certain time Δt as period, $\mathbf{m}_\tau(\mathbf{x})$ is obtained by a streamline integration of $\mathbf{v}$ at $\mathbf{x}$ over a time Δt. If $\mathbf{v}$ consists of saddles, its separatrices may induce tremendous changes in $\mathbf{m}_\tau$ so that it appears as discontinuities for normal discrete numerical programs. Figure 4.5 illustrates this.

4.4.2 Image analysis based surface extraction strategy

If we integrate the edges of the segmentation basins obtained from point based method either in forward or backward directions, we could get the separation surfaces for the asymptotic behavior of corresponding path-lines.

For a given periodic 2D time-dependent vector field $\mathbf{v}$, suppose we have extracted the separation surface S and at time τ, we have obtained the basin segmentation using point based method. λ_τ is the intersection curve of S and plane $t = \tau$. It is obvious that λ_τ exactly coincides with the edges of the segmentation basins in τ and λ_τ exactly coincides with $\lambda_{\tau+\Delta t}$. For any point $\mathbf{x}$ in λ_τ, if we integrate a path-line $\mathbf{P}(\mathbf{x})$, we can conclude that $\mathbf{P}(\mathbf{x})$ coincides in S within the domain and $\mathbf{m}_\tau(\mathbf{x})$ coincides $\lambda_{\tau+\Delta t}$ after a period at time $\tau + \Delta t$ if $\mathbf{m}_\tau(\mathbf{x})$ does not leave the domain. Thus, the integration surface of λ_τ coincides with S. Otherwise, $\mathbf{m}_\tau(\mathbf{x})$ would end up either in $basin_1$ or $basin_2$, then $\mathbf{x}$ must also be classified either $basin_1$ or $basin_2$ since it asymptotically converges to critical path-lines either in $basin_1$ or $basin_2$, which results in a contradiction. Note that $\mathbf{m}_\tau(\mathbf{x})$ does not necessary equal to $\mathbf{x}$, though it must locate in λ_τ. Figure 4.6 illustrates this relation.

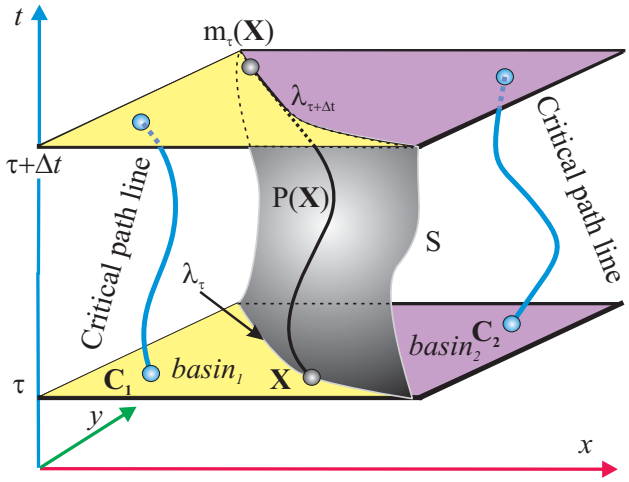

Figure 4.6: The relation between the basin edges and the separation surfaces for asymptotical path-line behavior.

Here the problem of extraction of separation surface turns to the detection of basin edges as seeding curves and the integration of these seeding curves to surfaces.

Seeding curve detection

Here we apply an image analysis approach to detect the basin edges. The basin edges are step discontinuities where the image intensity abruptly changes from one value to another. Many algorithms [GW92, JKS95] have been developed to detect such edges. Wallisch applied an extended marching cube approach to extracting the basin boundaries of 3D dynamical systems [Wal00]. Since we aim at a special problem, we apply one simple algorithm here.

Suppose the basin image is $f(x,y)$ in domain $F = [x_{min}, x_{max}] \times [y_{min}, y_{max}]$, where $f(x,y)$ is the id values for different basins. The gradient at location (x,y) is defined as follows:

$$\nabla f = \begin{pmatrix} G_x \\ G_y \end{pmatrix} = \begin{pmatrix} \frac{\partial f}{\partial x} \\ \frac{\partial f}{\partial y} \end{pmatrix} \tag{4.7}$$

the magnitude of the gradient vector is denoted $g(x,y)$ where

$$g(x,y) = |\nabla f| = \sqrt{{G_x}^2 + {G_y}^2} \tag{4.8}$$

Let $\alpha(x,y)$ represent the direction angle of the gradient vector with respect to the $x-$axis.

$$\alpha(x,y) = arctan(\frac{G_y}{G_x}) \tag{4.9}$$

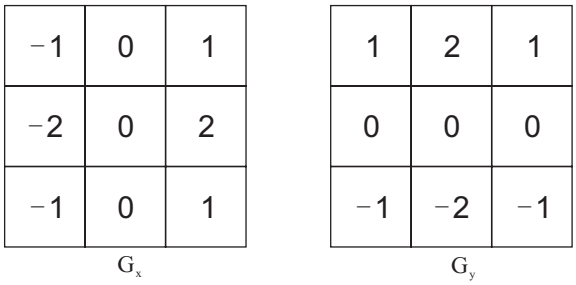

Figure 4.7: Sobel Operator.

The direction of an edge at (x,y) is perpendicular to the direction of the gradient vector. Here, for the discrete case, we use the Sobel operator to calculate the gradient vector as shown in Figure 4.7 [GW92].

We analyze the characteristics of pixels in a small neighborhood (say, 3×3 or 5×5) about every point (x,y) in the basin image. Thus an edge pixel with coordinates (x_0,y_0) in the predefined neighborhood of (x,y) is similar in magnitude to the pixel at (x,y) if

$$|g(x,y)-g(x_0,y_0)|\leq E \tag{4.10}$$

where E is a nonnegative threshold. Similarly (x_0,y_0) has similar direction as (x,y) if

$$|\alpha(x,y)-\alpha(x_0,y_0)|\leq A \tag{4.11}$$

where A is a nonnegative threshold.

A point in the predefined neighborhood of (x,y) is linked to the pixel at (x,y) if both magnitude and direction similarity criteria are satisfied. This process is repeated at every location in the basin image and finally we obtain the edges of the basins.

Step advancing integration with super sampling adjustment

With the detected seeding curve, the classical stream surface integration method is applied to generate the separation surface. However the pseudo discontinuity (see section 4.4.1) makes the integration quite unstable: a small error in the seeding curve may cause large error in the integration.

Here we apply step advancing integration in both forward and backward direction until they meet each other. In each integration step we use super sampling to adjust the result position. Figure 4.8 illustrates this. We divide period Δt into small steps δt, and integrate the surface step by step. For a seeding point $\mathbf{x}$ in

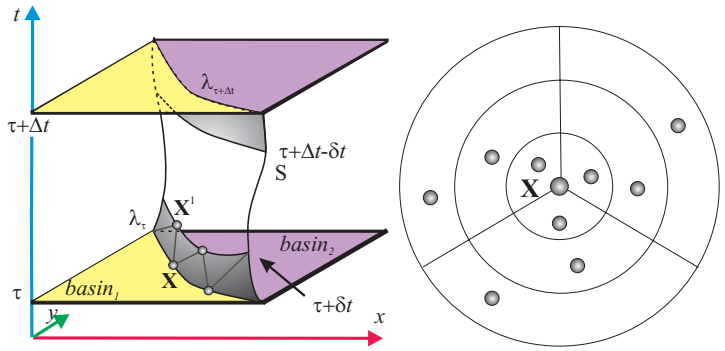

(a) (b)

Figure 4.8: (a) The integration of seeding curves with super sampling in both forward and backward direction until they meet each other; (b) The polar stratified super sampling: $n \times n$ subdivide the circular neighborhood in both radius and angle direction, for each subdivided grid, randomly select a point as sample point.

the seeding curve λ, we consider a small circular neighborhood around it and use polar stratified sampling (as shown in Figure 4.8b) to select the sample points, we integrate all these sample points for δt, and compare the end positions of them to collect the adjusted sampling result $\mathbf{x}^1$. Two strategies can be used to collect the adjusted result: (1) closest point to the neighbor adjusted result; (2) the average of sample end points in the most frequent area. In practice we haven't found significant differences between these two sample collection strategies. With the adjusted sampling result, we can integrate step by step further until the final surface is obtained.

4.5 The Algorithm

In this section we formulate our algorithm to get the path-line oriented topological segmentation of a periodic 2D vector field $\mathbf{v}(\mathbf{x},t)$:

1. Pick a time τ with $t_{min} \leq \tau < t_{max}$ for which we compute the topological segmentation.
2. Compute the Poincaré maps $\mathbf{m}_\tau$ and $\bar{\mathbf{m}}_\tau$, or equivalently, the vector fields $\mathbf{q}_\tau$ and $\bar{\mathbf{q}}_\tau$.
3. Extract the fix points of $\mathbf{m}_\tau$ and $\bar{\mathbf{m}}_\tau$.
4. Classify the fix points of $\mathbf{m}_\tau$ and $\bar{\mathbf{m}}_\tau$.

5. Assign an unique color to each sink of $\mathbf{m}_\tau$ and $\bar{\mathbf{m}}_\tau$.
6. For each $\mathbf{x}$ in the spatial domain: repeatedly apply $\mathbf{m}_\tau$ using Equation 4.3 starting from $\mathbf{x}$ and color code the result:
   - convergence to a sink → assigned color of the sink
   - leaving the spatial domain → color code leaving the domain
   - exceed maximal number of iterations → color code unknown converging behavior
7. Similar to 6 for $\bar{\mathbf{m}}_\tau$.
8. Overlay of the color coding schemes of 6 and 7 gives the complete classification of the asymptotic path-line behavior at the time τ.
9. Alternative to 8, extract the edges of the segmentation basins as seeding curves and integrate them step by step until the separation surfaces of asymptotic path-line behavior for a whole period is obtained.

This algorithm needs some remarks:

To 2 Since $\mathbf{m}_\tau$ and $\bar{\mathbf{m}}_\tau$ are known to have discontinuities, we sampled them in a rather high resolution and represented them as piecewise bilinear fields.

To 3 To extract the fix points of $\mathbf{m}_\tau$ and $\bar{\mathbf{m}}_\tau$, standard methods for piecewise bilinear fields are applied. However, from the set of extracted fix points we have to remove the ones which are located close to lines of discontinuities of $\mathbf{m}_\tau$ and $\bar{\mathbf{m}}_\tau$. We do so by choosing a small enough neighborhood in which we assume the vector field around the critical point to be continuous. Then we can compute the eigenvalues and eigenvectors of the critical point by sampling inside the neighborhood. With these eigenvalues and eigenvectors, we estimate the vector field inside the neighborhood and compare it with the original vector field. If the estimation error exceeds some threshold, it means there is no continuity inside the neighborhood, and the critical point is invalid.

To 4 Inside a cell, the bilinear interpolation of $\mathbf{m}_\tau$ and $\bar{\mathbf{m}}_\tau$ gives the Jacobian of a fix point.

To 5 We used a scheme of random isoluminant colors.

To 6 and 7 The resolution of the sampling for the color coding should not be less than the resolution of $\mathbf{m}_\tau$ and $\bar{\mathbf{m}}_\tau$, in order to deal with the discontinuities of $\mathbf{m}_\tau$ and $\bar{\mathbf{m}}_\tau$.

To 9, The extracted edges may have small jags, before integrating the separation surfaces, we must smooth them. Here we apply the Gaussian filter to smooth the

edges.

4.6 Applications

In this section we apply our technique to a number of test data sets.

A random data set

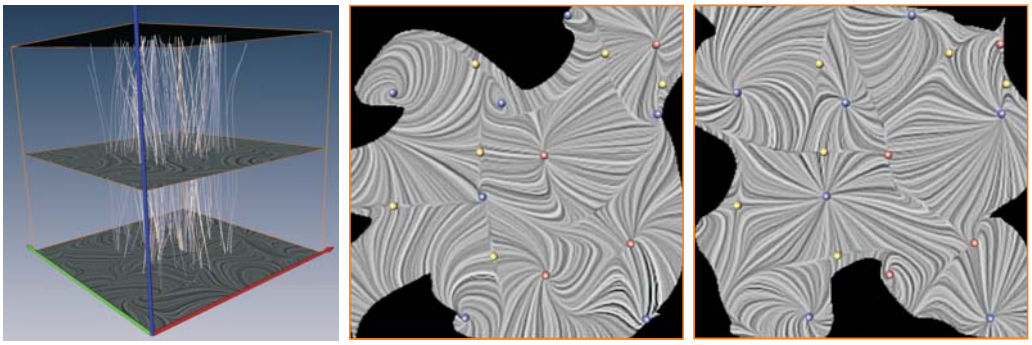

(a) (b) (c)

Figure 4.9: A random data set: (a) The vector field $\mathbf{p}$; (b) $\mathbf{q}_\tau$ at $\tau = t_{min}$; (c) $\bar{\mathbf{q}}_\tau$ at $\tau = t_{min}$.

Figures 4.9–4.11 illustrate our technique at a random vector field. We use random fields as a proof-of-concept because they contain a maximal amount of topological information. The vector field is piecewise trilinear over a $7 \times 7 \times 7$ grid where the time i-th and the $6-i$th time slices coincide for $i = 0,..,2$. Figure 4.9a shows the visualization of $\mathbf{p}$ using LIC planes at three different time slices as well as a number of illuminated streamlines. Figure 4.9b and c show the 2D vector fields $\mathbf{q}_\tau$ and $\bar{\mathbf{q}}_\tau$ which correspond to the Poincaré maps $\mathbf{m}_\tau$ and $\bar{\mathbf{m}}_\tau$ for $\tau = t_{min}$. The LIC images reveal the pseudo discontinuities in the Poincaré maps. However, the LIC images also present information about the streamlines of $\mathbf{q}_\tau$ and $\bar{\mathbf{q}}_\tau$. Since only a discrete integration is carried out, streamlines of $\mathbf{q}_\tau$ and $\bar{\mathbf{q}}_\tau$ do not have a physical interpretation. Figure 4.10a shows the basins of the sinks of $\mathbf{m}_\tau$ and Figure 4.10b does so for the basins of $\bar{\mathbf{m}}_\tau$.

Figure 4.11a shows the detected 7 sink behavior critical path-lines and their corresponding extracted separation surfaces. These critical path-lines are sinks in forward integration of $\mathbf{v}$ (marked with blue points), and all the path-lines in the

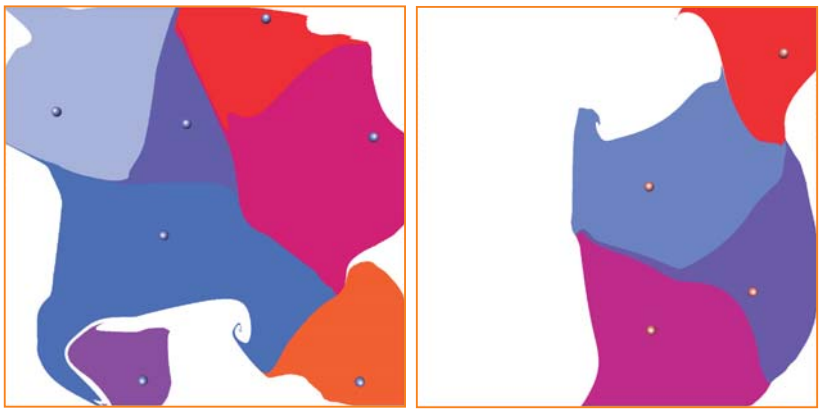

(a) (b)

Figure 4.10: A random data set: (a) Basins of $\mathbf{q}_\tau$ at $\tau = t_{min}$; (b) Basins of $\bar{\mathbf{q}}_\tau$ at $\tau = t_{min}$.

area between the critical path-line and the surrounding separation surface asymptotically converge to the critical path-line when integrated forward. Figure 4.11b shows the detected 4 source behavior critical path-lines and their corresponding extracted separation surfaces. These critical path-lines are sinks in backward integration of $\mathbf{v}$ (marked with red points), and all the path-lines in the area between the critical path-line and the surrounding separation surface asymptotically converge to the critical path-line when integrate backward. The computing time for

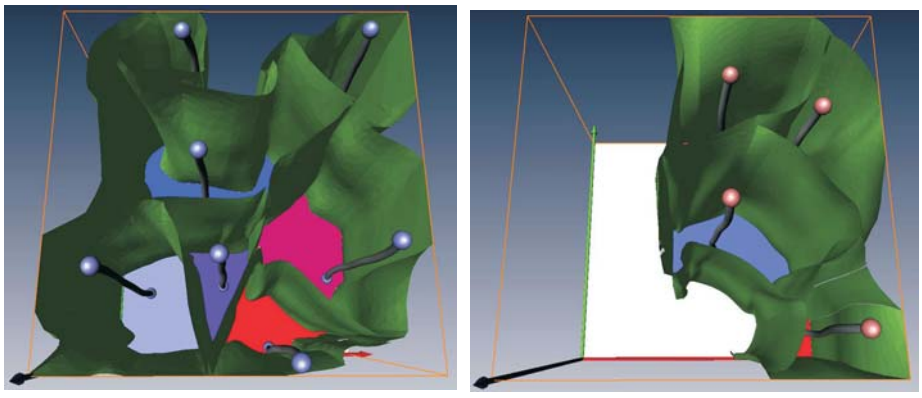

(a) (b)

Figure 4.11: A random data set: (a) The forward converge separation surfaces and the corresponding sink critical path-lines; (b) The backward converge separation surfaces and the corresponding source critical path-lines.

this data set was 10 minutes for the basin generation, several seconds for seeding

curve extraction and 30 minutes for the separation surface integration with 50 integration steps and 8×8 polar stratified super sampling on a Pentium 4 with 3.40 GHz.

ABC flow

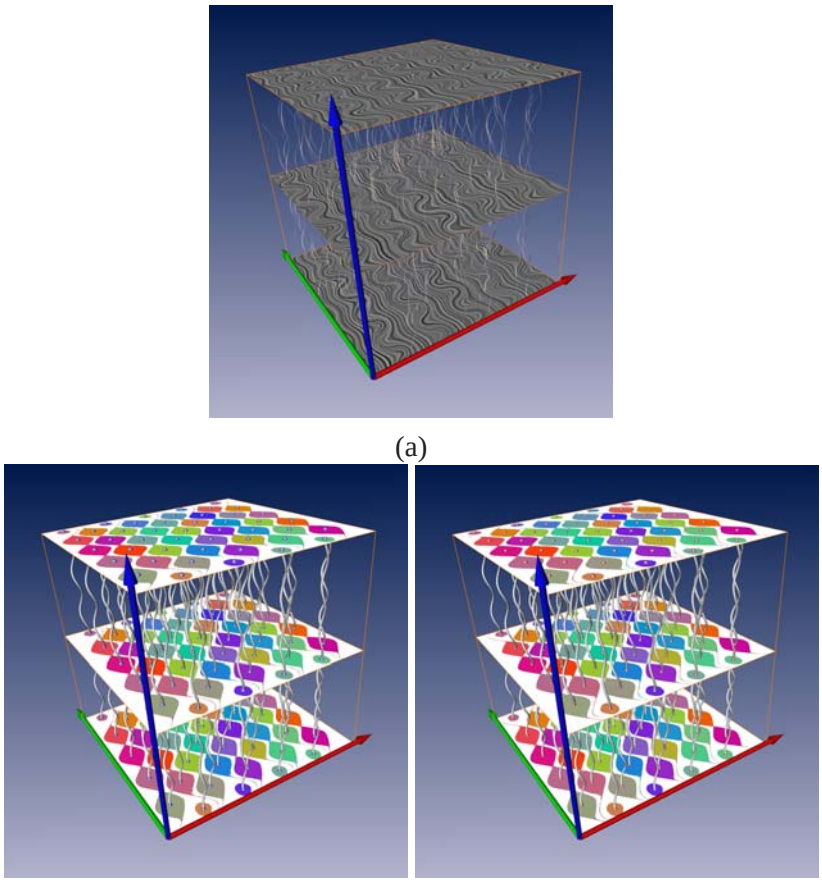

(a) (b) (c)

Figure 4.12: The ABC flow: (a) The vector field; (b) Critical path-lines and basins for forward integration; (c) Critical path-lines and basins for backward integration.

Figures 4.12–4.13 visualize parts of the so-called ABC (Arnold-Beltrami-Childress) flow which is given by

$$\begin{aligned} u(\mathbf{x}) &= A\sin z + C\cos y, \\ v(\mathbf{x}) &= B\sin x + A\cos z, \\ w(\mathbf{x}) &= C\sin y + B\cos x, \end{aligned} \tag{4.12}$$

where we set $A = \sqrt{3}$, $B = \sqrt{2}$ and $C = 1$. For our purpose, we considered a cut through the (x,y)-plane and interpret the z-coordinate as the time dimension:

$$\mathbf{p}(\mathbf{x},t) = \begin{pmatrix} \sqrt{3}\sin t + \cos y \\ \sqrt{2}\sin x + \sqrt{3}\cos t \\ 1 \end{pmatrix} \tag{4.13}$$

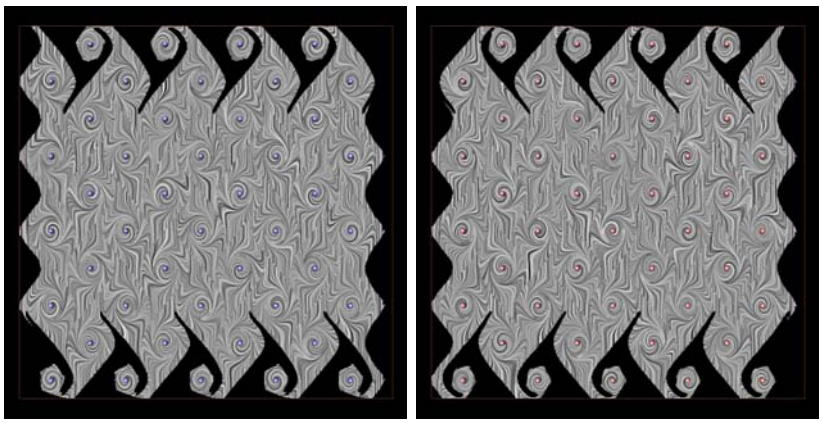

(a) (b)

Figure 4.13: The ABC flow: (a) $\mathbf{q}_\tau$ at $\tau = t_{min}$; (b) $\bar{\mathbf{q}}_\tau$ at $\tau = t_{min}$.

The field is periodic in x,y- and t direction with a period of 2π each. We visualize the behavior of the path-lines in the domain $[0,10\pi] \times [0,10\pi] \times [0,2\pi]$. Figure 4.12a shows the LIC plane and the path-lines. We detected 45 critical path-lines as illustrated in figures 4.12b and c. Figure 4.13 shows the LIC images of $\mathbf{q}_\tau$ and $\bar{\mathbf{q}}_\tau$: the classification gives that all critical points are weak sinks in $\mathbf{q}_\tau$. The norm of the eigenvalues is only slightly smaller than 1, and the basins are computed using 1000 integration steps. For $\bar{\mathbf{q}}_\tau$, all critical points are weak sinks as well, giving very similarly shaped basins as $\mathbf{q}_\tau$ (figure 4.12c). Since this contradicts to the property mentioned in section 4.3.1 (a sink in $\mathbf{q}_\tau$ is a source in $\bar{\mathbf{q}}_\tau$), we conclude that critical points have an unstable center-like behavior: path-lines in a certain neighborhood (color coded in Figures 4.12b and c) asymptotically remain in this neighborhood without converging/ diverging to/ from the critical path-line. Between these neighborhood regions there are regions where the path-lines leave the domain (white areas in Figures 4.12b and c). The computing time for this data set was 10 minutes for the Poincaré maps in a 1000×1000 resolution, and 1 minutes for the basins in a 1000×1000 resolution.

2D cavity flow

Figures 4.14–4.15 show the visualization of a vector field describing the flow at a 2D cavity. This data set was kindly provided by Mo Samimy and Edgar Caraballo (both Ohio State University) [CSJ] as well as Bernd R. Noack (TU Berlin). 1000

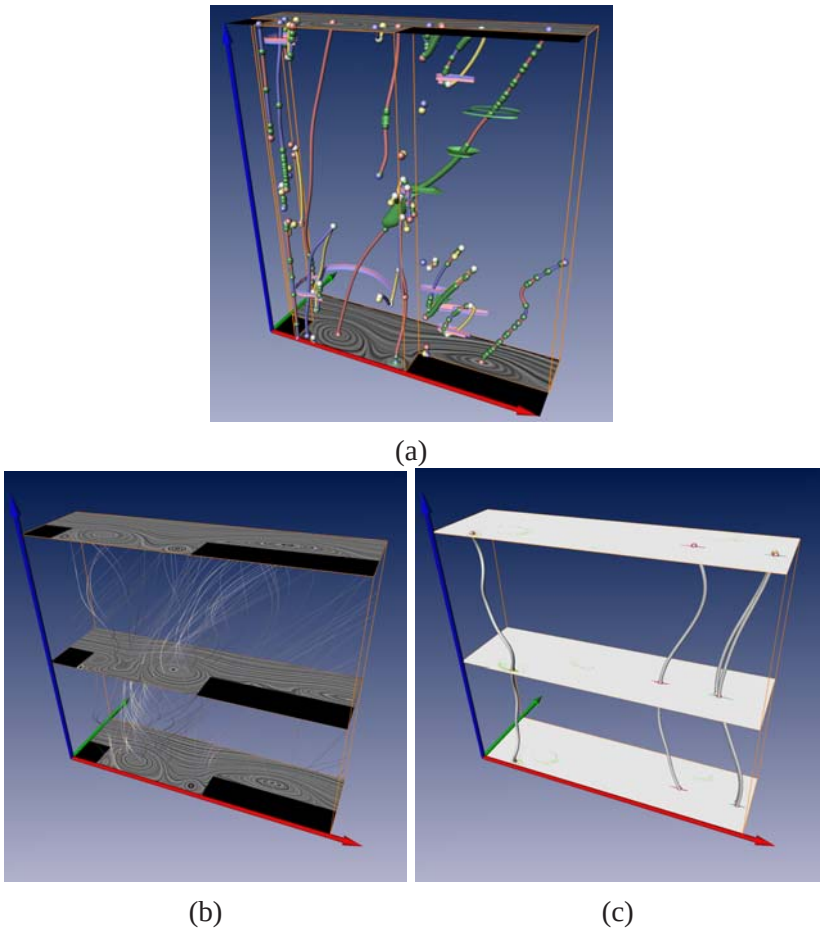

(a)

(b) (c)

Figure 4.14: The cavity flow: (a) Streamline oriented topology [TWHS05]; (b) The vector field **p**; (c) Critical path-lines.

time steps have been simulated using the compressible Navier-Stokes equations. The topological behavior of the streamlines of this data set has been analyzed in [TWHS05]. For this data set it turned out that the period appears every 79 time steps. Figure 4.14b shows **p** is one time period by two LIC planes and illuminated streamlines. Figure 4.14a (from [TWHS05]) shows the streamline oriented topological skeleton. This skeleton has a moderate complexity manifested in a number of moving critical points (represented by the colored lines) and bifurcations. The

topological skeleton of our path-line oriented topology looks more simple: we detected four critical path-lines which are shown in figure 4.14c. One of them is

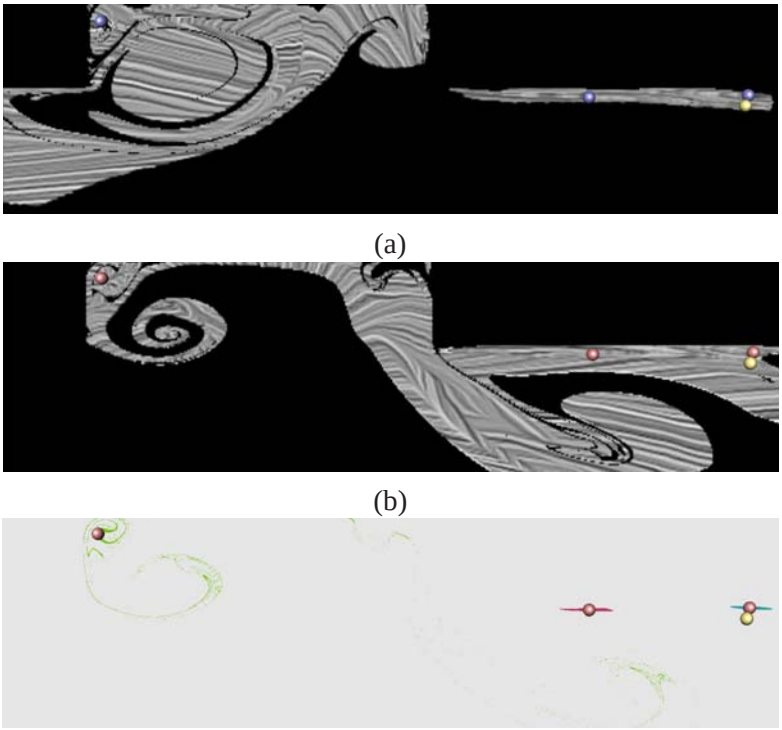

Figure 4.15: The cavity flow: (a) $\mathbf{q}_\tau$ at $\tau = t_{min}$; (b) $\bar{\mathbf{q}}_\tau$ at $\tau = t_{min}$; (c) Critical points and basins of $\bar{\mathbf{q}}_\tau$.

located inside the cavity, while the others are outside. Three critical path-lines are sinks under forward integration and sources under backward integration, the remaining one is a saddle. The total absence of any sinks in forward direction gives the main result of the topological analysis of his data set: every particle (except the ones starting on the critical path-lines) is going to leave the cavity after a certain time. Also, it is possible to show the regions from which a backward integration of $\mathbf{p}$ converges to the critical path-line: they are shown as colored areas in figure 4.15c. This figure clearly shows that the basins can have a rather disconnected structure. The computing time for the cavity data set was 30 minutes for the 3650×1000 Poincaré map, and 5 minutes for the basins in the same resolution. The LIC images of $\mathbf{q}_\tau$ and $\bar{\mathbf{q}}_\tau$ in Figures 4.15a and b illustrate this.

Electrostatic static field of benzene molecule

Figure 4.16 and figure 4.17 visualize the path-line oriented topology of the electrostatic field around a benzene molecule. This data set was calculated on a 101^3 regular grid using the fractional charges method described in [SS96] (discussed also in section 3.2.1). Originally this is a 3D steady gradient field describing the force of the electrostatic potential upon a positive point charge given in a certain location. If such a point charge is situated very close to the molecule, the closest atom will exert the highest force on it, i.e., attract or repel it. The influence of a single atom decreases the farther the point charge is located from the whole molecule. Instead, all atoms have nearly the same influence. One might say that the molecule as a whole is exerting force on a somewhat far located point charge. Thus, it is possible to distinguish between a near and a far field.

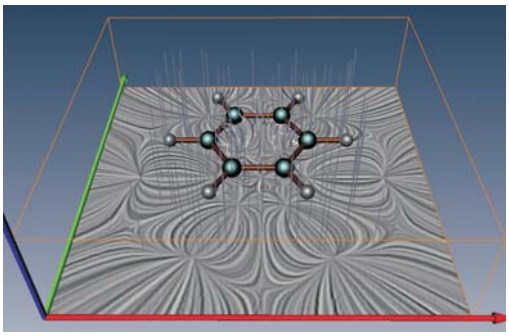

(a)

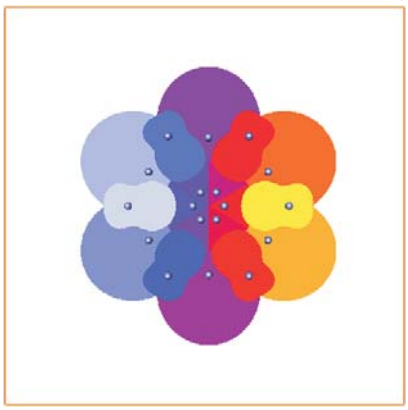

(b)

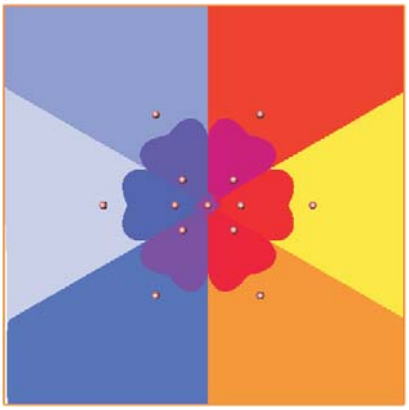

(c)

Figure 4.16: The periodic benzene data set: (a) The visualization of the periodic benzene force field, the benzene molecule and the corresponding path-lines; (b) Basins of $\mathbf{q}_\tau$ at $\tau = t_{min}$; (c) Basins of $\bar{\mathbf{q}}_\tau$ at $\tau = t_{min}$.

Since the behavior of this field is rather complex [TWHS03, WTS*05], we ap-

plied our method to find a simplified visual representation by neglecting the *w*-component of the field and interpreting the *z*-axis as time. This yields inside into the forces induced by the *distribution* of the atoms in the main plane of the molecule: as one moves away from the molecule, the influence of a single atom decreases and therefore the influence of the atom distribution decreases as well. The field can now be interpreted as a 2D periodic vector field, since the 2D forces are the same on both sides of the molecule.

Figure 4.16a elucidates the influence of atom distribution: the trajectories change radically close to the molecule (high influence in near field) while in other areas they are nearly straight (low influence in far field). To get insight into the attracting and repelling behavior, we computed the basins for forward and backward integration (figure 4.16b and c) as well as their corresponding critical path-lines (figures 4.17).

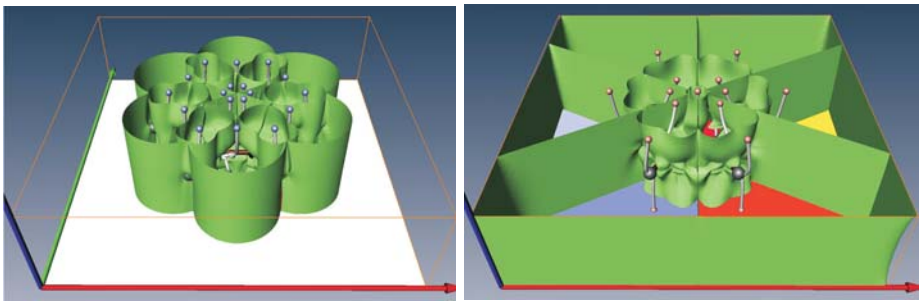

(a) (b)

Figure 4.17: The periodic benzene data set: (a) The forward converge separation surfaces and the corresponding sink critical path-lines for the benzene data set; (b) The backward converge separation surfaces and the corresponding source critical path-lines for the benzene data set.

Figure 4.17a shows the 18 sink behavior critical path-lines and their corresponding extracted separation surfaces for periodic benzene force field. All the point charges in the area between the critical path-line and the surrounding separation surface asymptotically converge to the critical path-line as time goes. Similarly figure 4.17b shows the 13 sink behavior critical path-lines and their corresponding extracted separation surfaces. All the point charges in the area between the critical path-line and the surrounding separation surface asymptotically converge to the critical path-line for backward integration. The computing time for benzene data set was 15 minutes for the basin generation, several seconds for seeding curve extraction and 100 minutes for the separation surface integration with 80 integration steps and 8×8 polar stratified super sampling.

4.7 Conclusion

In this chapter, we presented the following works:

- We introduced an approach to analyzing the asymptotic behavior of path-lines in periodic time-dependent vector fields.
- We defined, extracted, and classified critical path-lines.
- We computed the basins from which the path-lines converge to the critical path-lines in forward or backward integration.
- We presented an image analysis based approach to extracting the separation surfaces from the computed basins.

Our examples show that the path-line oriented topology gives significantly different topological information than the streamline oriented one. The main disadvantage of our approach is that it is limited to periodic vector fields only. In fact, we do not see a way to straightforwardly extend it to non-periodic vector fields. However, we think that due to the number of periodic vector fields obtained from time-dependent numerical flow simulations, this class of vector field data deserves the special consideration.

Chapter 5

Path-line Oriented Information Visualization Approach

In this chapter, we describe an approach to visually analyzing the dynamic behavior of 3D time-dependent flow fields by considering the behavior of the path-lines. Information visualization is an important methodology in modern scientific and engineering research. The integration of flow visualization with information visualization has provided fluid analysts an opportunity to interactively identify the patterns or features of interest (see also section 3.3). The complexity of 3D dynamical flow as well as the dimensionality of the underlying space-time domain makes the classical fluid analysis and flow visualization challenging and partially unsolved. In particular, it inherently difficult to actually comprehend the important characteristics of 3D time-dependent flow data. Interactive analysis with expert support offers an alternative solution for complex dynamical fluid analysis, which is convenient for fluid analysts.

Feature based approaches extract a variety of different features such as topological features, vortical structures, or shock waves (see also section 3.2). They reflect different properties of the flow and therefore focus on the representation of different inherent structures. In fact, not all features may give useful information for every flow data set, and the selection of the relevant features is often left to users in an unsupported way. Moreover, among the features there may be correlations which are either general due to their definition, or they occur in certain areas of particular flows and give relevant information about the behavior of the flow. Therefore we believe that not only the introduction and visualization of new features leads to a deeper understanding of the dynamic behavior of the flow field, but

also an effective analysis of the relations between the features and the applications of these results for a visual representation. We make one step along the recently challenging path towards a better understanding of 3D unsteady flow fields.

Our approach starts with the extraction of a number of properties (scalar values, and time series) at each point of a regular sampling of the 4D space-time domain. Since path-lines are important characteristic curves for unsteady flow fields (see also section 2.2.1) and the analysis of the dynamic behavior of flow fields is strongly related to the analysis of path-lines. We focus on properties describing the behavior of the path-lines, being either classical and well-established values in vector algebra, or properties newly proposed in this chapter. The result of this step is a *path-line attribute data set*: a four-dimensional multivariate data set collecting all computed path-line properties.

The visual analysis of multidimensional multivariate data is a well-researched topic in information visualization. A variety of techniques have been developed to visualizing such data sets making inherent correlations visible. Because of this we attempt to use information visualization approaches to analyzing the path-line attributes data set. The results of this analysis (i.e., selections of path-lines with certain combinations of properties) are then used for a focus+context visualization of either the selected path-lines or the interesting properties. This way the user is able to do a simultaneous exploration in the 4D space-time domain of the flow and in the abstract path-line attribute space. We show that this can give new insight into characteristic substructures of the flow which leads to a better understanding of time-dependent flow fields.

The work closest to ours is the SimVis approach [DGH03, DMG*05] (see section 3.3) which uses approaches of information visualization to analyzing various kinds of simulation data. The main difference to our approach is that SimVis works on multiple scalar data describing certain properties of the simulation. Contrary to this, our approach works on dynamic flow data, focusing on local and global properties of path-lines, i.e. on a multi-variate properties data set, derived from a 3D unsteady flow field. We apply our method to a number of flow data sets and describe how path-line attributes are used for describing characteristic features of these flows.

5.1 Path-line Attributes

Given a 3D time-dependent vector field $\mathbf{v}(\mathbf{x},t)$, $\mathbf{x}$ describes the 3D domain and t is the temporal component. Streamlines and path-lines are generally different

classes of curves (see section 2.2.1). Given a point $(\mathbf{x}_0, t_0)$ in the 3D space-time domain, the streamline starting at $(\mathbf{x}_0, t_0)$ can be written in a parametric form

$$\mathbf{s}_{\mathbf{x}_0,t_0}(t) = \mathbf{x}_0 + \int_0^t \mathbf{v}(\mathbf{s}_{\mathbf{x}_0,t_0}(\tau), t_0)\, d\tau \tag{5.1}$$

while the path-line starting at $(\mathbf{x}, t)$ has the parametric form

$$\mathbf{p}_{\mathbf{x}_0,t_0}(t) = \mathbf{x}_0 + \int_0^t \mathbf{v}(\mathbf{p}_{\mathbf{x}_0,t_0}(\tau), \tau + t_0)\, d\tau. \tag{5.2}$$

To characterize path-lines, we consider two kinds of information: scalar value that describes local or global properties of a path-line, and time series that collects information along a path-line.

5.1.1 Scalar attributes

For scalar attributes, we compute a number of scalar properties of the path-line starting at a given point $(\mathbf{x}_0, t_0)$ which reflect either local or global properties of the path-lines. In the latter case, the value depends on the considered integration time. Since we are interested in the global behavior of the path-lines, the integration time can be chosen rather large (relative to the time interval in which $\mathbf{v}$ is defined). In particular, we compute the following scalar values:

Id	Description
distSE	Relative start end distance
nonStraightV	Non straight velocity
avDir	Average direction
avParticleV	Average particle velocity
lyapunov	Lyapunov exponent
wind	Winding Angle
lad	Local acceleration displacement
curvDiff	Curvature difference
div	Local divergence

We will explain these properties as follows:

- Relative distance between start point and end point *distSE* is the 3D Euclidean distance between the start point and the end point of a path-line relative to the integration time T.

$$distSE = \frac{|\mathbf{p}_{\mathbf{x}_0,t_0}(T) - \mathbf{x}_0|}{T} \tag{5.3}$$

A small *distSE* can be expected to be an indicator of a swirling behavior of a path-line (while rotating back the path-line accumulates less distance from its start point).

- Non straight velocity *nonStraightV* is the difference arc length between the length of real particle path and the distance from start point to end point relative to the integration time T.

$$nonStraightV = \frac{\int_0^T \|\mathbf{v}(\mathbf{p}_{\mathbf{x}_0,t_0}(\tau), \tau + t_0)\| \, d\tau - |\mathbf{p}_{\mathbf{x}_0,t_0}(T) - \mathbf{x}_0|}{T} \tag{5.4}$$

nonStraightV is an important measure of the non straight behavior of a path-line. A small *nonStraightV* indicates straight behavior of a path-line. Particularly, if $nonStraightV = 0$, the corresponding path-line is a straight line between start point and end point. Large *nonStraightV* usually indicates swirling behavior.

- Average direction *avDir* depicts the general trend of a path-line movement. It can be computed as the difference of end and start point of a path-line. Here we map all the tangent vectors along a path-line to a unit sphere and then calculate the average of these mapped vectors as shown in Figure 5.1.

$$avDir = \frac{\mathbf{p}_{\mathbf{x}_0,t_0}(T) - \mathbf{x}_0}{\|\mathbf{p}_{\mathbf{x}_0,t_0}(T) - \mathbf{x}_0\|} \tag{5.5}$$

avDir contains three scalar components separately as scalar property for our analysis.

- Average particle velocity *avParticleV* is computed as the arc length of a path-line relative to the integration time T:

$$avParticleV = \frac{\int_0^T \|\mathbf{v}(\mathbf{p}_{\mathbf{x}_0,t_0}(\tau), \tau + t_0)\| \, d\tau}{T} \tag{5.6}$$

- Lyapunov exponent *lyapunov* is a popular quantity to describe the stability of a dynamical system. Here we consider the largest finite-time Lyapunov exponent (see section 3.4.4) [Hal01]. The linear flow map $A = \nabla_{\mathbf{x}} \mathbf{p}_{\mathbf{x}_0,t_0}(T)$ of the 3D time-dependent vector field is computed, then the largest eigenvalue λ_{max} is computed and normalized by the integration time T.

$$lyapunov = \frac{log(\sqrt{\lambda_{max}(A^T A)})}{T} \tag{5.7}$$

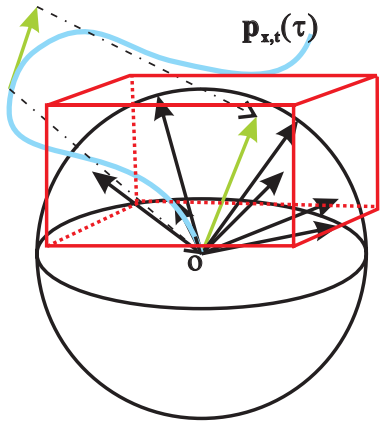

Figure 5.1: Mapping the direction vectors along a path-line to a unit sphere and calculating the bounding box approximation of the opening cone.

- Winding angle *wind* is a measure of how strong a path-line differs from being a straight line. We define it in a discrete form, i.e., on a polygonal approximation $(\mathbf{p}_0, \mathbf{p}_1, ..., \mathbf{p}_n)$ of a path-line obtained from a numerical integration. We consider the angles of the adjacent edges of the polygon:

$$wind = \sum_{i=0}^{n-2} \angle(\ (\mathbf{p}_{i+1} - \mathbf{p}_i), (\mathbf{p}_{i+2} - \mathbf{p}_{i+1})\ ). \tag{5.8}$$

  Figure 5.2a gives an illustration. Note that this measure depends both on the shape and on the parametrization of the path-lines. A larger *wind* can be expected to indicate a swirling behavior.

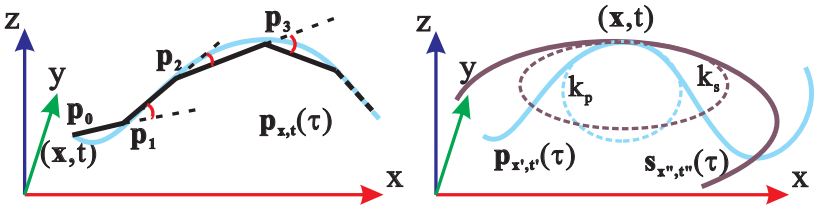

(a) (b)

Figure 5.2: (a) Winding angle along a path-line; (b) Curvature difference between the path-line and streamline pass through a specified point.

- Local acceleration displacement *lad* is a global measure of how strong streamlines and path-lines differ: we observe the streamline and the path-line starting at the same location over some time and consider the Euclidean distances of the end points of the trajectories:

$$lad = \|\mathbf{p}_{\mathbf{x}_0,t_0}(T) - \mathbf{s}_{\mathbf{x}_0,t_0}(T)\| \tag{5.9}$$

Figure 5.3a gives an illustration. A small *lad* denotes quasi-stationary parts of the flow, since there streamlines and path-lines coincide.

- Curvature difference between path-line and streamline *curvDiff*: Given a point $(\mathbf{x}_0, t_0)$, there is exactly one streamline and one path-line passing through it. Both curves coincide in the tangent direction but generally differ in their curvature. The (squared) differences of the curvatures is a measure of how strong streamlines and path-lines differ locally. Given a path-line $\mathbf{p}_{\mathbf{x}_0,t_0}(t)$ in its parametric form (Equation 5.2), we can compute its derivatives as [The98]

$$\frac{\delta\, \mathbf{p}_{\mathbf{x}_0,t_0}}{\delta\, t}(0) = \dot{\mathbf{p}} = \mathbf{v}(\mathbf{x}_0,t_0) \;\;,\;\; \frac{\delta^2\, \mathbf{p}_{\mathbf{x}_0,t_0}}{\delta\, t^2}(0) = \ddot{\mathbf{p}} = \nabla\mathbf{v}\cdot\mathbf{v} + \frac{\delta\mathbf{v}}{\delta t}. \tag{5.10}$$

For a streamline $\mathbf{s}_{\mathbf{x}_0,t_0}(t)$ in parametric form (Equation 5.1), the derivatives are

$$\frac{\delta\, \mathbf{s}_{\mathbf{x}_0,t_0}}{\delta\, t}(0) = \dot{\mathbf{s}} = \mathbf{v}(\mathbf{x}_0,t_0) \;\;,\;\; \frac{\delta^2\, \mathbf{s}_{\mathbf{x}_0,t_0}}{\delta\, t^2}(0) = \ddot{\mathbf{s}} = \nabla\mathbf{v}\cdot\mathbf{v}. \tag{5.11}$$

Then the local curvatures of path-lines and streamlines are

$$\kappa_{\mathbf{p}} = \frac{\|\dot{\mathbf{p}}\times\ddot{\mathbf{p}}\|}{\|\dot{\mathbf{p}}\|^3} \;\;,\;\; \kappa_{\mathbf{s}} = \frac{\|\dot{\mathbf{s}}\times\ddot{\mathbf{s}}\|}{\|\dot{\mathbf{s}}\|^3} \tag{5.12}$$

and

$$curvDiff = (\kappa_{\mathbf{s}} - \kappa_{\mathbf{p}})^2. \tag{5.13}$$

Figure 5.2b gives an illustration. *curvDiff* is a local geometric measure of how stationary the flow is.

- Local divergence *div* denotes the classical operator in vector algebra which coincides for considering streamlines and path-lines [TWHS04]:

$$div = \mathrm{div}(\mathbf{v}). \tag{5.14}$$

5.1.2 Time series attributes

For time series we have investigated the following attributes:

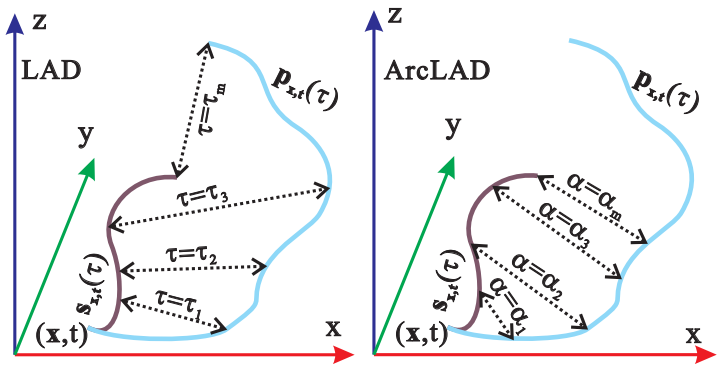

Figure 5.3: (a) LAD that records the Euclidean distance between the point of a path-line the corresponding streamline at the same time t; (b) ArcLAD that records the Euclidean distance between the point of a path-line and the corresponding streamline at the same arc length α from the start point.

Id	Description
DistEu	Euclidean distance to start
LAD	Local acceleration displacement
ArcLAD	Arc local acceleration displacement
Dir	Direction vector
OpeningCone	Opening cone
Curvature	Path-line curvature
Velocity	Velocity magnitude

We will explain these properties as follows:

- Euclidean distance to start point *DistEu* is the non-relative time series extension of the *distSE*. It records the Euclidean distance from the seed point to every point along a path-line.

$$DistEu(t) = \|\mathbf{p}_{\mathbf{x}_0,t_0}(t) - \mathbf{x}_0\| \tag{5.15}$$

- Local acceleration displacement *LAD* is the time series extension of the single scalar *LAD*. It observes the Euclidean distance between the streamline and the path-line over the same integration time as shown in Figure 5.3a.

$$LAD(t) = \|\mathbf{p}_{\mathbf{x}_0,t_0}(t) - \mathbf{s}_{\mathbf{x}_0,t_0}(t)\| \tag{5.16}$$

- Arc local acceleration displacement *ArcLAD* is the arc length adaption of local acceleration displacement. The local acceleration displacement defined

above depends on the flow velocity: in areas of higher velocity, streamlines and path-lines have a bigger chance to move away from each other in a certain time. Therefore, in areas of higher velocity the *LAD* tends to be large. To get a geometric measure of how strong a streamline and a path-line differ, we compare the Euclidean distances of the points with the same arc length from the start point. Figure 5.3b illustrates this.

- Direction vector *Dir* records the direction vector at every time along a path-line. Three components of direction vector forms three corresponding time series.
- Opening cone *OpeningCone* records the opening cone at every time along a path-line. Here we use the bounding box approximation to expedite the calculation without sacrifice the monotonic property of the opening cone series, as shown in Figure 5.1. At each time, we record the volume of the bounding box which covers all the points on the unit sphere where the direction vector maps to [SAE93].
- Path-line curvature *Curvature* records the curvature of a path-line at every time along the integration.
- Velocity magnitude *Velocity* is the velocity magnitude time series considering every time along a path-line.

5.2 System overview

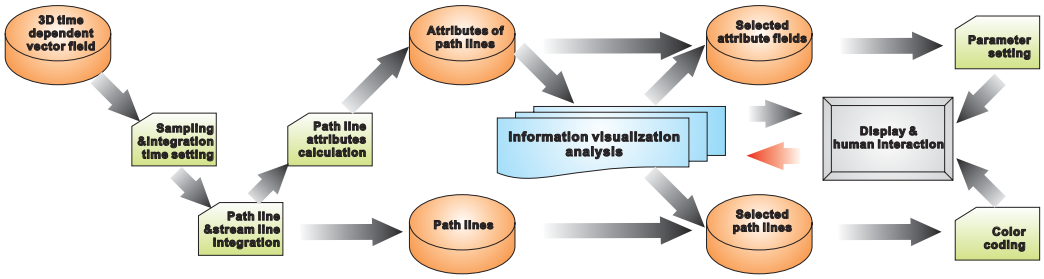

Figure 5.4: Pipeline for analyzing path-line attributes.

Fig. 5.4 shows the pipeline of our path-line attribute analysis approach. We start with a 3D time-dependent flow field $\mathbf{v}$ to be analyzed. As a first step, we apply a *sampling* of the space-time domain to obtain the points for which we compute the path-line attributes. Note that since the data lives in a 4D domain, even a

rather small sampling density may give a high amount of sample points. Therefore, the sampling density should be a compromise between the spatio-temporal accuracy of the analysis and the available computing resources. If the analysis delivers interesting features in certain smaller regions of the domain, this region can be analyzed using a higher sampling density to make sure the sampling rate is above the Nyquist frequency. At this state of the approach we also have to set the *integration time* for the path-lines. Also this setting is a tradeoff between the fact that we want to have the path-lines to be analyzed as long as possible and the property that most of the path-lines should be integrated over the same time without leaving the domain.

The next step of the approach is the integration of the streamlines and path-lines starting from the sampled points over the set integration time. For our examples we have used a 4th order Runge-Kutta integration. From these integrations we compute all path-line attributes introduced in section 5.1.

The set of all path-line attributes is the input of our information visualization core module which will be described in section 5.2.1 in more detail. Interactive visual analysis on the basis of state-of-the-art information visualization techniques and brushing in linked views is used to extract relevant correlations, interesting feature combinations, or general properties of the data. The result of this analysis is used to steering the visualization of the path-lines and their attributes. If the interactive visual analysis delivers interesting features in a certain scalar path-line attribute, we can visualize it using standard volume rendering techniques like direct volume rendering or slicing. Furthermore, the interactive visual analysis delivers a selection of interesting path-lines having a certain combination of properties. They are visualized as 3D line structures with a color coded time component.

Our implementations of the visualization of the selected path-lines and the selected attributes are based on Amira [SWH05b], whereas our information visualization analysis is based on the ComVis system which is described in section 5.2.1.

5.2.1 The ComVis system

ComVis is an interactive visualization tool. It supports conventional information visualization views such as 2D and 3D scatter plots, parallel coordinates, histograms, as well as a special curves view which is used for displaying function graphs (see section 3.3). This combination of views makes it possible to analyze a wide variety of data where in the same row of a multi-variate table some values are scalar (just as it is usual) and others correspond to a function graph (common

in various kinds of scientific data)[MJJ*05]. The tool offers multiple linked views parallel to each other. Each view can be of any of the above mentioned view type. ComVis pays great attention to interaction. Due to advanced brushing and linking proved to be very powerful analytical tool. Users can brush the visualized data in any view, all linked views reflect the data selections by appropriate focus+context visualization. Furthermore, the user can use a simple, yet powerful line brush in the curves view. The line brush selects all curves which intersect the line. All brushes can be scaled and moved interactively. The multiple brush mode makes it possible to flexibly combine various brushes. The user selects brushes and boolean operations between them. AND, OR, and SUB are supported. Furthermore, the tool creates a composite brush in an iterative manner. This means that the user selects a current operation (AND, OR, or SUB) and draws a brush. The previous brushing state is combined with the new brush accordingly. The new state is computed, and it is used when the user draws another brush. In this way the user immediately gets visual feedback, and can very easily broaden the selection (using OR), or can further restrict the selection (using AND or SUB). Once the user is satisfied with a selection (or in the meantime), a tabular representation of the selected data can be shown and exported to file on demand.

5.3 Applications

We applied our approach to a number of data sets. Not surprisingly, not all attributes are interesting in all data sets, and different path-line attributes turn out to be important for different data set. However, we can also identify several interesting coherence between different path-line attributes which seem to hold even for different data sets. Accordingly, we are optimistic that the here described analysis indeed provides a useful basis for future generalization of this approach.

3D time-dependent cylinder flow

Figures 5.5 and 5.6 present some results of analyzing a 3D time-dependent flow behind a circular cylinder. The cylinder is put in the origin with radius 0.5 and height 8.0, while the data set domain D is $[3.15, 19.74] \times [-2.06, 2.06] \times [0.09, 1.89] \times [0, 2\pi]$. This data set was kindly provided by Gerd Mutschke (FZ Rossendorf) and Bernd R. Noack (TU Berlin). We considered path-lines at a $28 \times 14 \times 7 \times 6$ (191MB attribute file to ComVis) sampling and used an integration time of 1.5π (for the data set given in a 2π time slab). Figure 5.5a shows the direct volume rendering of one of the attribute fields *lyapunov*. In figure 5.5b, all path-lines in-

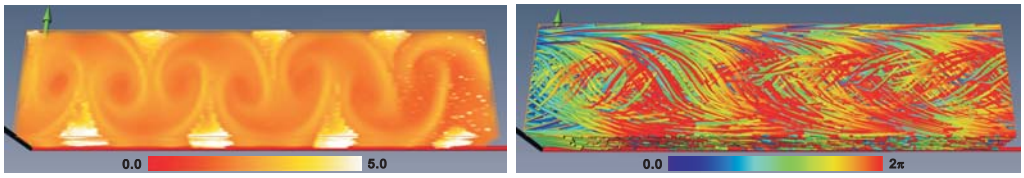

(a) (b)

Figure 5.5: Flow behind a cylinder: a) Direct volume rendering of the *lyapunov* attribute field at time 0; b) All considered path-lines.

tegrated from the sampled points are displayed. As we can see from figure 5.5a, there are certain patterns in the *lyapunov* attribute field. Low *lyapunov* values indicate stability of the path-line. We use the information visualization approach to select the area with low *lyapunov*, as shown in the upper left of figure 5.6a. The visualization of the selected path-lines is shown in figure 5.6b. Figure 5.6c shows the seed area of the selected path-lines at the time 0.

When investigating the visualized result, we can see that there are further different patterns in the low *lyapunov* path-lines. It is obvious when we investigate the ComVis result of time series *LAD*, after choosing the cluster as shown in the upper right of figure 5.6d. We get the path-line cluster whose *LAD* time series have small values at the end of the integration time. Figure 5.6e and 5.6f present the visualization of the selected path-lines and their seed areas. We notice that they stay in the middle of the domain and along the flow direction directly behind the cylinder.

Hurricane Isabel

Figures 5.7– 5.9 show a visual analysis of the hurricane Isabel data set, which has been previously analyzed in a number of papers [GJ04, DMH04]. We sample the domain with path-lines at a resolution of $24 \times 24 \times 6 \times 6$ (253MB attribute file to ComVis), and set the maximum integration time to 30 hours (the whole data set covers 48 hours). Figure 5.7a shows the visualization of all considered path-lines. Figure 5.7b show a direct volume rendering of *nonStraightV* at time 0 (the starting time of the simulation).

For this data set, we start the information visualization analysis, with the observation of the *avParticleV* vs. *distSE* scatter plot (upper right of Figure 5.8a), showing a number of points on the diagonal but also a number scatter points clearly above it. We expect the points on the diagonal to represent path-lines with a rather straight-line-like behavior, whereas the locations of the points above the diagonal

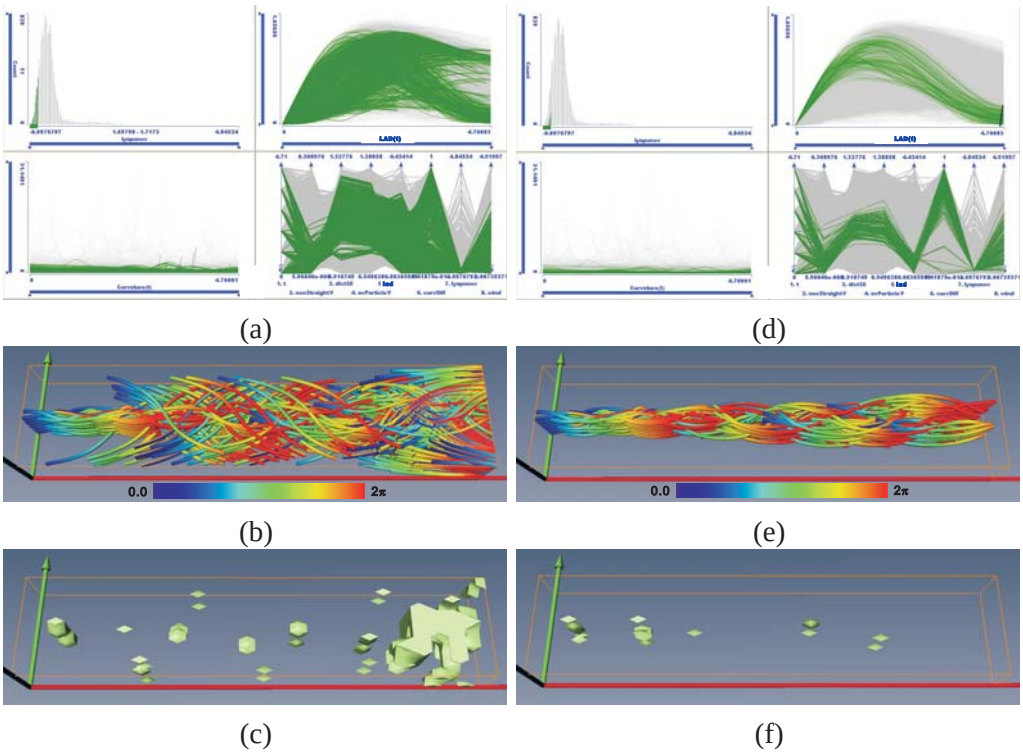

Figure 5.6: Feature low *lyapunov* and *LAD*: a) Selecting low *lyapunov* area in ComVis; b) Visualization of selected path-lines with low *lyapunov*; c) Visualization of the seeding area of the selected low *lyapunov* path-lines at time 0; d) Selecting low *lyapunov* and parabola *LAD* area in ComVis; e) Visualization of selected path-lines with low *lyapunov* and low *LAD*; f) Visualization of the seeding area of the selected low *lyapunov* and low *LAD* path-lines at time 0.

may indicate a swirling behavior. Since *nonStraightV* is equivalent *avParticleV* vs. *distSE*, we selected all points above the diagonal, by considering points with a rather high *nonStraightV* (upper left of Figure 5.8a). The parallel coordinate representation (lower right of Figure 5.8a) shows that the selected path-lines have a rather low *curvDiff*. This indicates that in these regions streamlines and path-lines are locally rather similar. The curvature plot of the selected path-lines doesn't have extreme values (lower left of Figure 5.8a). The selected path-lines are visualized in Figure 5.8b, clearly showing that we have selected the ones swirling around the moving eye of the hurricane. Figure 5.8c shows the areas where the selected path-lines originate at time $t = 0$, while Figure 5.8d shows the starting areas of the selected path-lines for all time steps.

In a second analysis attempt, we select all path-lines with a high value in the curvature plot (upper left of Figure 5.9a). The selected path-lines are shown in

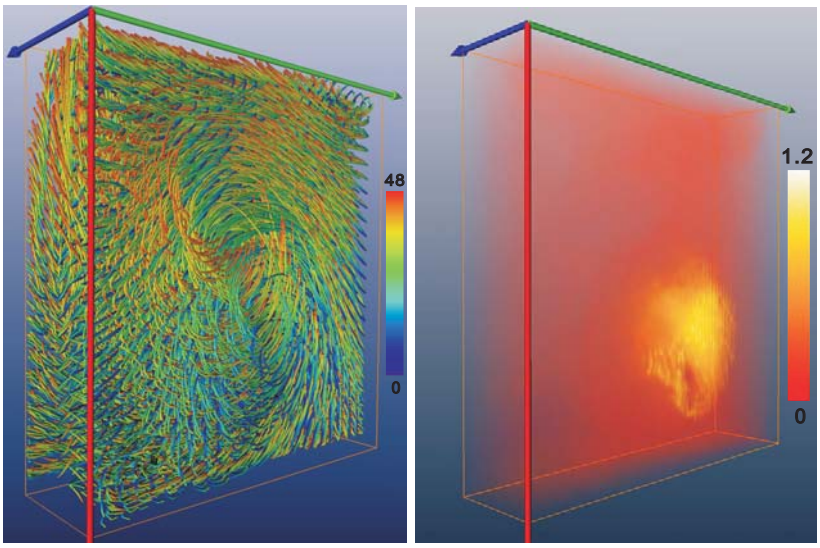

(a) (b)

Figure 5.7: Hurricane Isabel data: (a)All considered path lines; (b) Direct volume rendering of the *nonStraightV* attribute field at time 0.

Figure 5.9b. All of them are rather short and have a rather irregular behavior and they indicate some part of the flow where the velocity is quite small.

Airfoil

Figures 5.3 - 5.12 show a comparative visual analysis of 8 different data sets of a flow around an airfoil. The difference between these 8 data sets are the air injection frequency. The injection frequencies are 0(base), 0.2, 0.44, 0.6, 0.88, 1.0, 1.5 and 2.0. The goal of our analysis is to find the best air injection frequency which contributes the best lift power. It is known that abnormal vortex structures reduce the lift of the airfoil. Therefore, our visual analysis focuses on the areas with vortices where the probability of abnormal flow is high. We reduce our consideration to a small area around the areas with vortices.

We sample the interesting area with path-lines at a resolution of $36 \times 12 \times 8 \times 10$ for each data set, and set the maximum integration time to 30 seconds (the whole data set covers different time domains for different frequencies and the path-line integration will usually leave the domain within 30 seconds for each frequency). Figure 5.3 shows the LIC visualization at starting time for different frequencies and Figure 5.11 shows the visualization of all considered path-lines for different frequencies. We observe that most path-lines behave well showing a rather straight

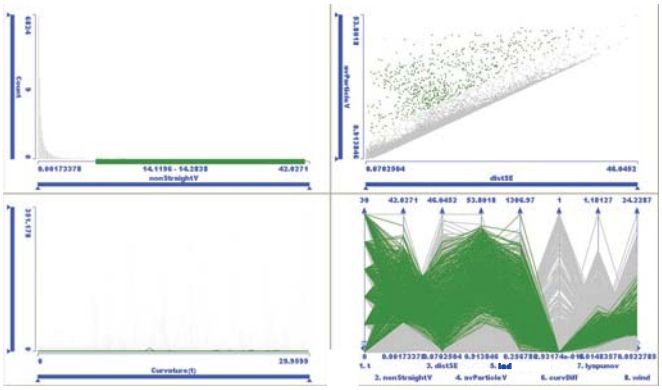

(a)

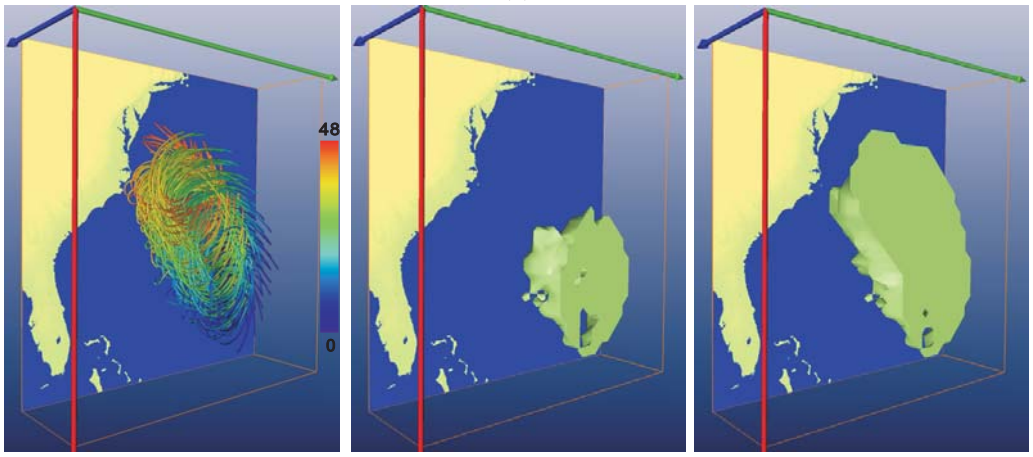

(b) (c) (d)

Figure 5.8: Hurricane Isabel data: (a) Selecting the area with high *nonStraightV* in ComVis; (b) Path-lines of the selected high *nonStraightV*; (c) The seeding area of the selected path-lines at time 0; (d) The seeding area of the selected path-lines at all time steps.

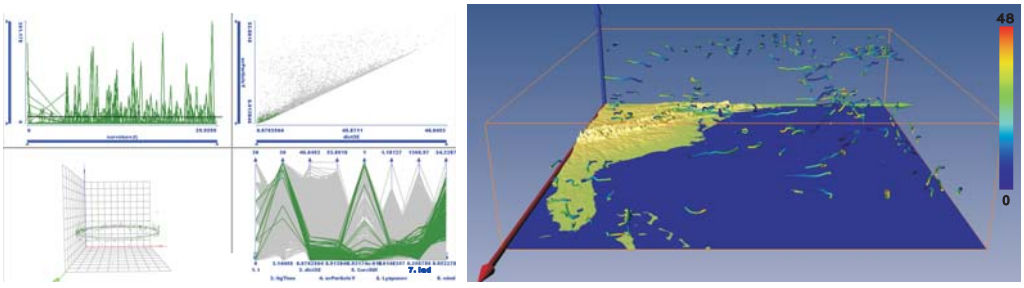

(a) (b)

Figure 5.9: Hurricane Isabel data: a) Selecting the area with peaks in *curvature* plot; b) Selected path-lines of *curvature* plot peaks.

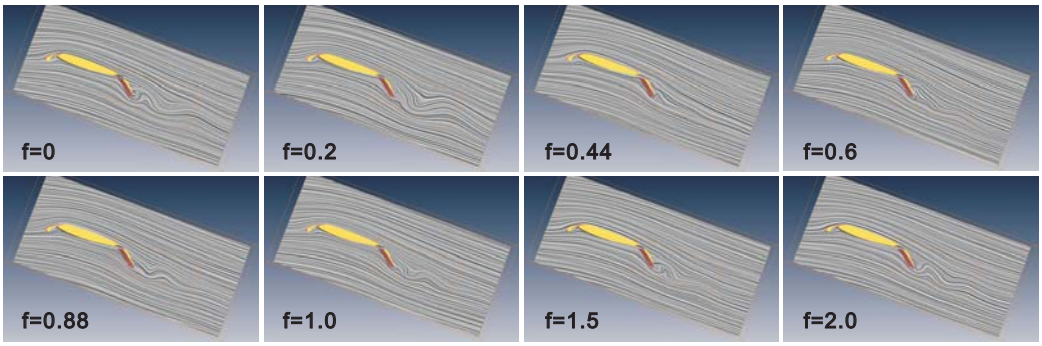

Figure 5.10: The visualization of airfoil flow field at time 0 for different air injection frequency with LIC plane.

behavior. The abnormal flows correspond to those non straight path-lines. As our experience on these attributes, the *nonStraightV* is a good attribute to reflect the characteristics of straightness of path-lines. So we compare this attribute computed at same location and same time for different frequency data sets in ComVis.

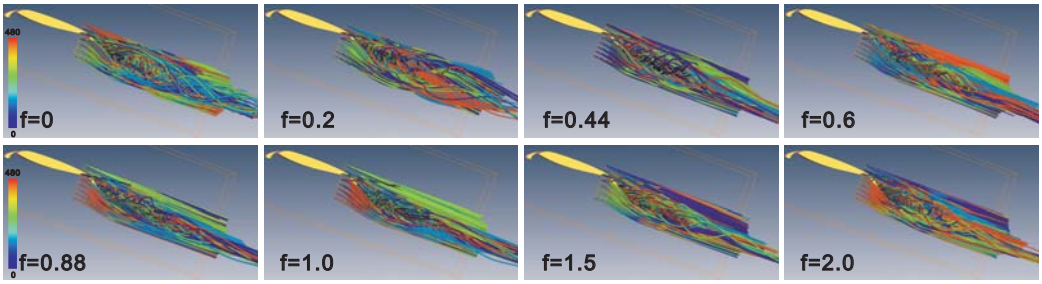

Figure 5.11: The path-lines started from the focus area of the airfoil flow field for different air injection frequency.

Figure 5.12 shows the comparative result of the analysis of the *nonStraightV* for these 8 different frequencies. Relative analysis is popular in airfoil analysis since the relative flow behavior for different parts of an airfoil determines the lift power. We apply a relative selection here and select those path-lines for each data set with 70 percent highest *nonStraightV* attributes. Those selected path-lines and the corresponding seeding areas are visualized. We can see that these selected non straight path-lines are closed to the area with vortices. And we can clearly observe that for a frequency 0.6, there are fewest non straight path-lines and the non straight seeding areas are the smallest. So we find that for frequency 0.6, the probability of abnormal flow is less compared to others. We have tested several other percentage of the highest *nonStraightV*. All the results present the equivalent information. We conclude that 0.6 is the best air injection frequency among the 8

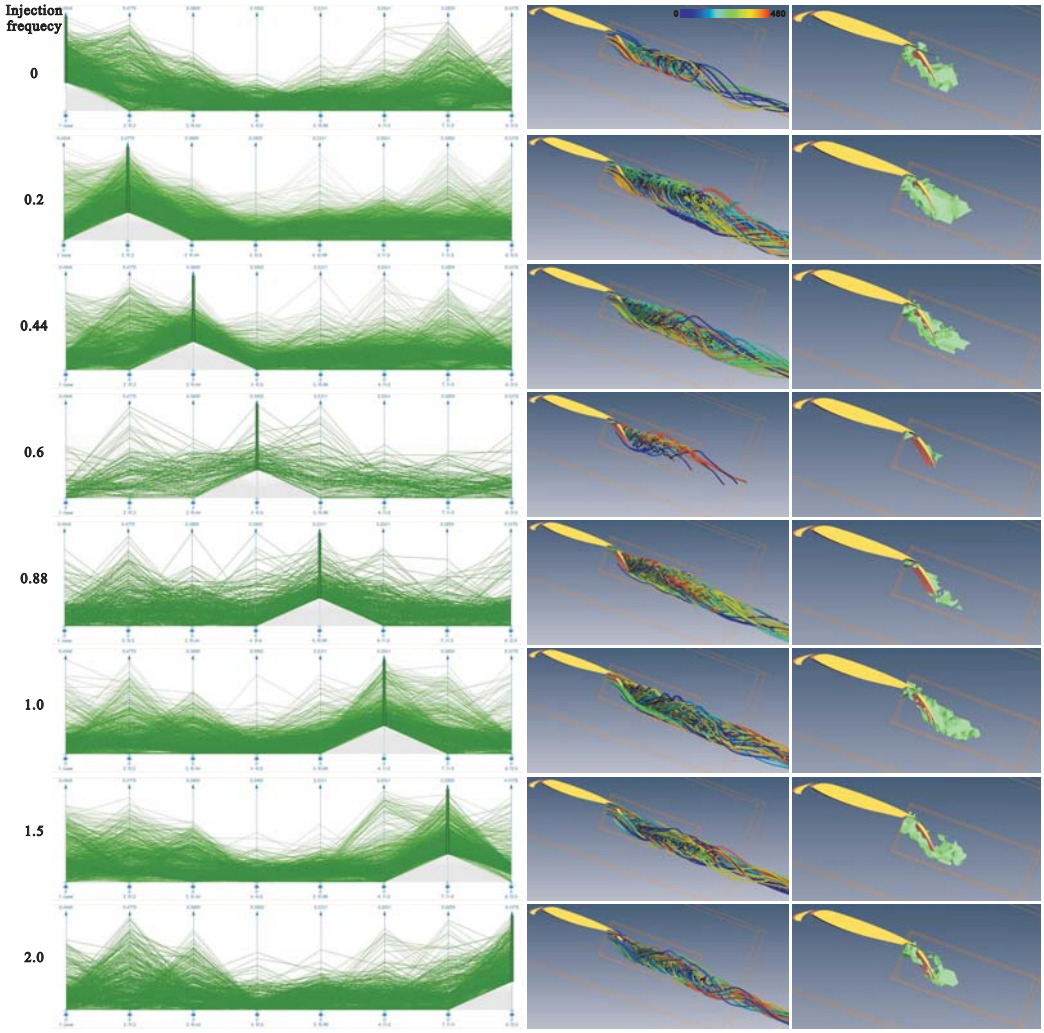

Figure 5.12: The comparative analysis result for the attribute *nonStraightV* of of the airfoil flow field for different air injection frequency. The pictures in the first column depict the selections of 70 percent highest *nonStraightV* for different frequencies in ComVis. The pictures in the second column depict the corresponding selected path-lines for the first column. The pictures in the third column are the corresponding seeding area for the selections in the first column.

tests. The experience from the industry partner confirms this result successfully.

5.4 Conclusion

To getting insights into dynamic behaviors of path-lines of 3D time-dependent flow fields is still a challenging problem for the visualization community. Path-lines elude a straightforward extension from streamline based methods because path-lines can be integrated only over a finite time, and they may intersect each other (at least when only considering their 3D reference locations). This chapter discusses an approach to getting insights into behaviors of path-lines by applying an approach from information visualization. In particular, the following work is done:

- We identified a number of local and global attributes of path-lines which we expect to contain relevant information about the path-line behavior.
- We interactively analyzed these attributes by using an approach from information visualization. The results were used to steering a 3D path-line visualization.
- We applied our approach to a number of data sets, in order to get new insight into the path-line behavior.

During our analysis it turned out that not all path-line attributes gave useful results for all data sets. However, inherent and data independent correlations in the attribute data set can be expected, making a reduction of the attribute set possible. In particular, we have the impression that the investigation of path-line attributes can indeed lead to a useful and practicable way of accessing/segmenting interesting flow features in time-dependent data sets, including swirling/vortical/rotating flow subsets, (e.g., via attributes *wind* and *nonStraightV*) , quasi-steady flow structures, (e.g., via attributes *LAD* and *ArcLAD*, etc.), etc. We are optimistic with respect to these expectations, not at the least because it was, for example, fairly straight forward and quite easy to accomplish to extract the rotating main vortex of hurricane Isabel, which – to the best of our knowledge – cannot so easily be accomplished with any of the previously published vortex extraction methods.

Chapter 6

Finite-time Transport Structures

Transport is an important phenomenon underlying a flow process. Any substance or property such as dye, momentum or heat can be transported in a fluid [KC04]. Modern experimental and computational fluid mechanics are increasingly concerned with the structure nature of fluid transport. Many promising approaches have been developed to depict the dynamical transport behavior of flow fields. However, it has still proved to be inherently difficult to actually comprehend the important characteristics of this complex dynamical phenomenon. Particularly, the property nature of a flow transport phenomenon is usually unclear and hard to interpret. An effective visual analysis of flow transport is still a challenging problem in scientific visualization. In this chapter, we focus on the transport characteristics of physical properties and propose an approach to visualize the finite-time transport structures of the properties.

Classical approaches of dynamical flow analysis tend to extract the transport features in Eulerian perspective and to track these features along time (see section 3.4). Though these approaches generate promising results, the extracted features depend strongly on each instant step and they are not natural for dynamical analysis. Lagrangian coherent structure (LCS) is one highlight in flow transport analysis which identifies the transport barriers during flow advection (see section 3.4.4). In contrast to traditional approaches, LCS gives a different and natural insight into the dynamical processes of fluid transport. However, some important physical properties are not considered and the transport characteristics of these properties are still not clear. To get a better understanding of intrinsic flow transport, the visual analysis of physical property transport for a flow field is necessary. For this analysis, it is not enough to investigate only the fluid motion. The corre-

sponding physical properties need to be included.

One way to visualize the dynamical behavior of fluid transport is to integrate the history of the fluid transport for a certain time-interval. A transport filter is described here to convolute the corresponding physical property field over time and compress the relevant transport information of these properties to a investigating point. The corresponding transport structures can be visualized through the convoluted results. Advection, diffusion and radiation are common transport modes in nature. In a fluid, advection describes the transport by the macroscopic motion of currents in contrast to others. It is generally the major transport mode which characterizes a fluid phenomenon. For an advection process, a fluid is described mathematically as a vector field (see section 2.2). In flow visualization, Line integral convolution (LIC) is one standard technique to access the flow advection nature (see section 3.1.3). It is similar to advect a noise texture field along flow transport trajectories and generate the motion blur of the processing texture field. This texture motion blur reflects the underling substance concentration which figures out the geometrical distribution of the corresponding trajectories.

In this chapter, we focus on the visualization of the advection behavior of a flow field. We propose a transport filter for fluid advection, i. e. an advection filter, which is similar to applying LIC along path-lines. Instead of a noise texture, the advection filter convolutes a correlated physical property field. This is similar to investigate the physical properties along flow transport and record the advection blur of these properties. The result field of the convolution is different from the original physical property field, since it senses the dynamical behavior of the transport and it distinguishes from the traditional LIC result while it captures the property characteristics of the flow field.

6.1 Fluid Transport

Transport is one dominant phenomenon during a flow process. The transport phenomenon considered in fluid dynamics is macroscopic and a fluid is regarded as a continuous medium (see also section 2.1) [Lea07]. Any substance, or property can be transported in a fluid. The conservative transport of the substances or properties can be described with the continuity equations (Equation 2.14). *Reynolds transport theorem* is a fundamental theorem used in formulating the basic laws of fluid dynamics [Kre00]. For a system with a control volume and a control surface. Reynolds' transport theorem states that the rate of change of an extensive property Φ within the system is equal to the rate of change of Φ within the control volume and the net rate of change of Φ through the control surface. For a given flow field

$\mathbf{v}(\mathbf{x},t)$ and a specified property Φ, the transport process can be written in a partial differential form as follows:

$$\frac{\partial \Phi}{\partial t} + \nabla \cdot \mathbf{J}(t,\mathbf{x},\Phi,\mathbf{v},\nabla\Phi) = g(t,\mathbf{x},\Phi) \tag{6.1}$$

where $\mathbf{J}$ represents the flux of the property transport and g specifies the source of the flow. Consider the momentum as the transported property, with the additional assumption Newton's viscosity law, the Navier-Stokes momentum equation (see section 2.3.3) can be derived from Equation 6.1. Further, various transport phenomena underlying a flow process can be expressed by a series of partial differential equations (PDE).

6.1.1 Advection and diffusion

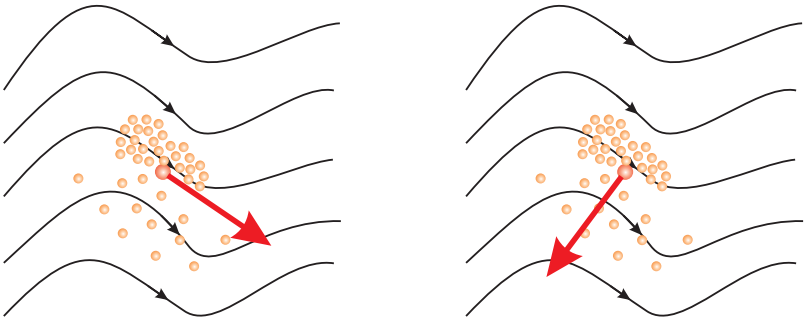

(a) (b)

Figure 6.1: Transport phenomena: (a) Advection; (b) Diffusion.

Advection and diffusion are two common transport modes during a fluid transport [Lea07]. Advection describes the transport by the macroscopic motion of currents as shown in Figure 6.1a. For a pure advection phenomenon without additional source, Equation 6.1 can be modified as follows:

$$\frac{\partial \Phi}{\partial t} + \nabla \cdot (\Phi \mathbf{v}) = 0 \tag{6.2}$$

For incompressible flow (see section 2.1.4), the advection equation can be simplified as

$$\frac{\partial \Phi}{\partial t} + \mathbf{v} \cdot \nabla\Phi = 0 \tag{6.3}$$

In contrast to advection, diffusion is the spontaneous transport of properties from an area of high concentration to an area of low concentration in a given volume

of fluid down the concentration gradient as shown in Figure 6.1b. For an isotropic diffusion process, Equation 6.1 can be modified as follows:

$$\frac{\partial \Phi}{\partial t} = c\nabla^2\Phi \tag{6.4}$$

where c is the diffusion coefficient to characterize the diffusion process. Diffusion is a statical process of random motion and describes the natural tendency to the equilibrium of property distribution.

Note that in the illustration of this chapter, the small particles are abstract distributions of the transporting substances or properties. They are not necessary real particles.

6.2 Transport Filter

Though the physical mechanism of the property transport is clearly revealed through the PDEs in the former section, the PDEs themselves are expressed in Eulerian perspective (see section 2.1.2) and their physical pictures are still not clear. An intuitive visualization of the effects of these PDEs on the transporting properties is helpful to the understanding of the complex phenomenon. To do so, it is critically important to see the patterns concerned with the phenomenon. And it is natural to tracking the property transport to uncover these patterns, i. e. by Lagrangian approaches.

Structure information is essentially important during fluid analysis. However, most flow patterns are invisible to human perception. The art of flow visualization is to make these underlying patterns visible. A common way is to identify some visible distribution field related to the phenomenon and visualize the specified patterns through the corresponding distribution fields. The distribution fields are normally scalar fields either in 2D or 3D, which could be visualized with classical visualization approaches.

Then the problem comes to the identification of such a distribution field which captures the transport behavior. To reflect the dynamical transport behavior, the history of the transport process needs to be represented properly. For a given spatial-temporal point $(\mathbf{x}_0, t_0)$, all the information relevant to the transport behavior happened at the investigating point over a certain time interval needs to be collected. Convolution is a powerful tool to identify the relevant information in a specified domain and to increase the visual depth into a complex phenomenon. Here we apply convolution in spatial-temporal domain as shown in Figure 6.2a.

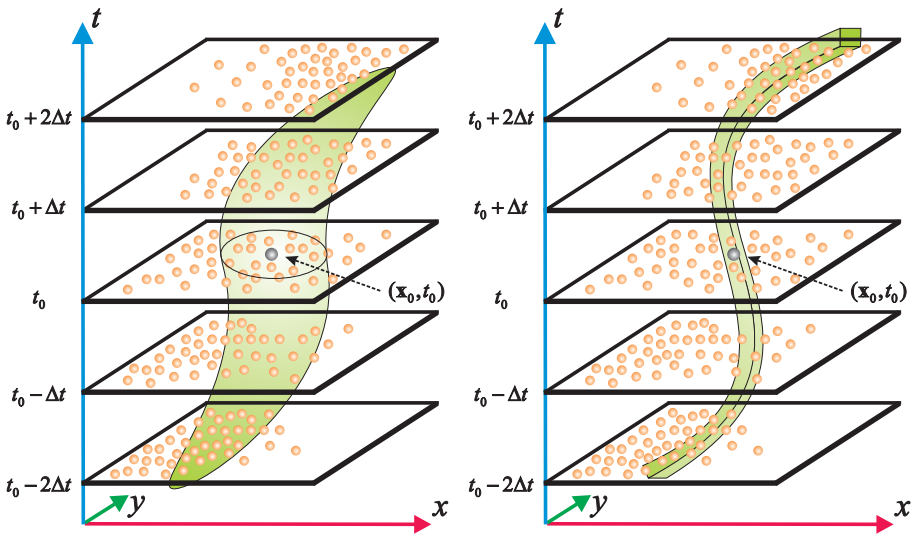

Figure 6.2: An illustration of transport filter for 2D unsteady flow fields: (a) General transport filter; (b) Transport filter for advection.

A *transport filter* is introduced here to identify the neighborhood in the spatial-temporal domain relevant to the transport behavior for a certain time interval at the investigating point and to record all the information within this neighborhood to that point based on the transport mechanism, which is illustrated in Figure 6.2a. The transport mechanisms are based on the theories of theoretical fluid dynamics, which are usually expressed in PDEs. For an isotropic diffusion process described with Equation 6.4, the transport filter can be directly solved through the corresponding PDE, which is expressed as a Gaussian type filter in spatial-temporal domain. The scale of a transport filter is related to the time interval of the investigation and can be specified by the user interests. A transport filter integrates the information of transport history and the results can be interpreted as motion blur of the property transport.

A transport filter integrates the information of transport history and the results can be interpreted as motion blur of the property transport.

6.2.1 Advection filter

Advection is generally the major transport mode underlying a flow process. It describes the transport with the motion of a fluid, which is one fundamental topic in fluid dynamics. Under the advection mode, the transport mechanism is interpreted

as following along the trajectories of fluid elements, i. e. path-lines. This means we use path-lines to design the transport filter for the advection.

As discussed in section 3.1.3, LIC is one standard technique in flow visualization. It imitates the motion blur of substance advection in a fluid and the results describe the substance concentration due to transport behavior of the fluid. Classical LIC puts noise textures into a flow field and advects these textures along the flow currents. A visualization of the streamline structures can be obtained by observing the blurred result of the texture advection, which depicts the geometrical distribution of the advection trajectories.

Similarly, convolution along path-lines (Path-line LIC) tracks the transport evolution in time and provides an effective approach to uncover the dynamical information of flow advection [SJM96]. It is natural to extend the Path-line LIC to property advection phenomenon and the transport filter for advection, i. e. an advection filter, is equivalent to the convolution along path-lines, which is illustrated in Figure 6.2b. Applying to the properties under investigation, an advection filter integrates the history information along the fluid currents and generates the motion blur underlying the advection mechanism.

Given a time-dependent vector field $\mathbf{v}(\mathbf{x},t)$, Equation 5.2 defines a path-line $\mathbf{p}_{\mathbf{x}_0,t_0}(t)$ starting at $(\mathbf{x}_0,t_0)$ in the parametric form. A path-line is a function of time. It depends on the initial position $\mathbf{x}_0$, the initial time t_0 and the integration time t. A path-line integration can be carried out in both forward and backward direction. In real applications, flow data is usually given in a fixed spatial and temporal domain, which means that we could only integrate path-lines for a finite-time. A path-line starting from $(\mathbf{x}_0,t_0)$ can be also parameterized in the form of $\mathbf{p}_{\mathbf{x}_0,t_0}(s)$ with a specific arc length s.

Given a scalar property field, an advection filter consists of calculating an intensity value I by convoluting it along path-lines either for a fixed time:

$$I(\mathbf{x}_0,t_0) = \int_{-T_1}^{T_2} k(\tau)\, f(\mathbf{p}_{\mathbf{x}_0,t_0}(\tau),\tau)\, d\tau \tag{6.5}$$

or for a fixed length:

$$I(\mathbf{x}_0,t_0) = \int_{-S_1}^{S_2} k(\tau)\, f(\mathbf{p}_{\mathbf{x}_0,t_0}(l), t(\mathbf{p}_{\mathbf{x}_0,t_0}(l)))\, dl \tag{6.6}$$

where k denotes a filter kernel. $T_1 > 0$ and $T_2 > 0$ are the kernel lengths which specify the forward integration time and backward integration time. The integration could be restricted to one direction by simply setting the other parameter to

0. Similarly, $S_1 > 0$ and $S_2 > 0$ specify the integration arc length in forward and backward direction.

Note, in real applications, usually the resulting intensity is normalized by dividing either the total integration time or the integration arc length.

6.3 Finite-time Transport Structure

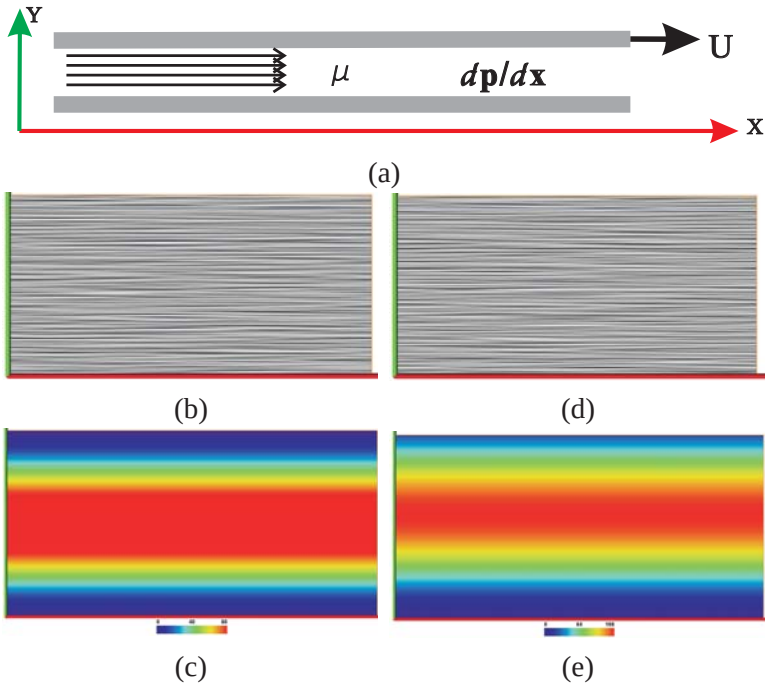

Figure 6.3: Visualization of a steady water flow between parallel plates: (a) Flow configuration; (b) Classical LIC visualization for $U = 0$; (c) Path-line LIC over kinetic energy field for $U = 0$; (d) Classical LIC visualization for $U = 8m/s$; (e) Path-line LIC over kinetic energy field for $U = 8m/s$.

To visualize intrinsic structures of property advection for flow fields, we also try to identify certain distribution fields concerning of flow advection. Through applying advection filter over certain field, we record the advection concentration of this field. A key step for advection filter is to select proper property field for convolution. Classical approaches convolute noise textures to generate a motion blur field for visualization. However, this blurred result field after advection records only the information of geometrical distributions of either streamlines or pathlines. Some characteristic physical information is not well explored during the

convolution. Instead of noise textures, we advect physical properties of interest along flow fields and observe the advection concentration of the corresponding properties, which reveals structure nature of property advection.

A simple example is illustrated in Figure 6.3 which describes an analysis over a well developed 2D water flow between two parallel plates. One plate is moving forward with certain velocity and the pressure gradient is constant for the flow (Figure 6.3a). This is a simple steady flow which can be well solved in flow dynamics [KC04]. Figure 6.3b and d show a visualization using classical LIC approach for two cases with different plate moving velocities. We can see that the results are nearly the same. Geometrical distributions of transport trajectories are not enough to identify the full view of a dynamical behavior. The dynamical information, especially the structure nature of property transport, is also important during flow analysis. Instead of noise texture, we convolute the corresponding kinetic energy along path-lines and visualize the result distribution in Figure 6.3c and d. High values of this field indicate strong kinetic energy advections. This distribution uncovers the structures of the kinetic energy transport of this plate flow. The asymmetry of plate moving is clearly distinguished here.

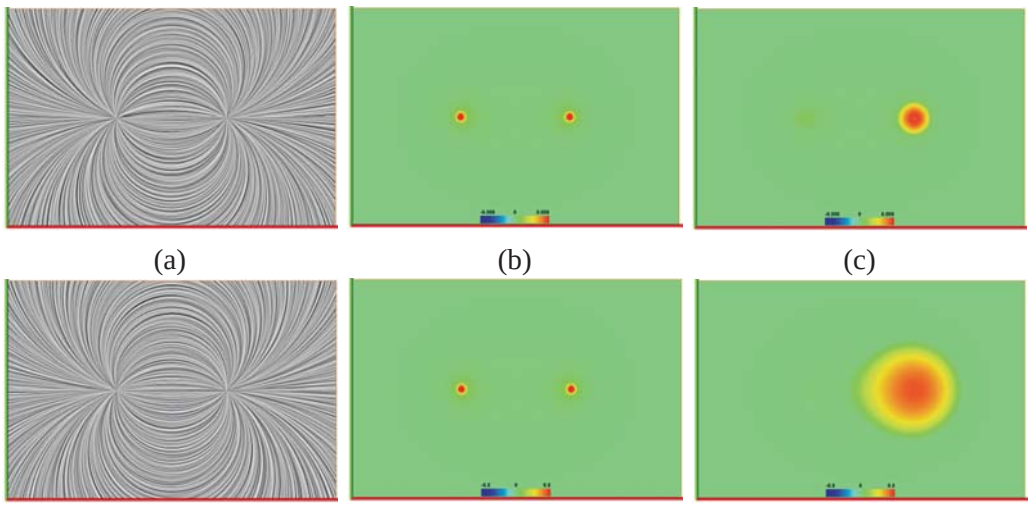

Figure 6.4: (Visualization of a dipole flow, the first row $m = 0.0628$, the second row $m = 0.628$: (a,d) Classical LIC visualization; (b,e) Color coding of kinetic energy field; (c,f) Path-line LIC over kinetic energy field.

Note that for steady flow, path-lines coincide with streamlines. We consider simple 2D steady flow in this section to illustrate some basic ideas.

An extension of LIC by color coding local properties is used to supplement prop-

erty information during flow transport [LHD*04]. However, it still records the local information instead of the dynamical transport nature. Figure 6.4 and 6.5 show an analysis of two dipole flow of different volume flow rate per unit depth m [KC04]. The first two columns of Figure 6.4 show the comparison of the LIC visualization and color coding of local kinetic energy. Structurally, the visualization between the two dipoles are the same. The dynamical transport nature is not fully uncovered with either LIC or local property visualization. We apply advection filter over local kinetic energy field and visualize the result distribution in Figure 6.4c and f. The values of the convoluted field indicate the advection magnitude and the high values point out the concentration trend of the underlying flow advection. Here, high values correspond to the sink area. These distributions reveal the advection nature of kinetic energy under the flow process. The inherent asymmetry is clearly observed in these kinetic energy transport structures. People can distinguish the two dipoles through the difference of the kinetic energy transport structures. Figure 6.5 show the FTLE fields of corresponding dipoles which present the corresponding LCS (see section 3.4.4). It not surprising that the kinetic energy advection structures of dipole follows generally with LCS appearing in the corresponding FTLE fields, since LCS describes purely the barriers of fluid advection.

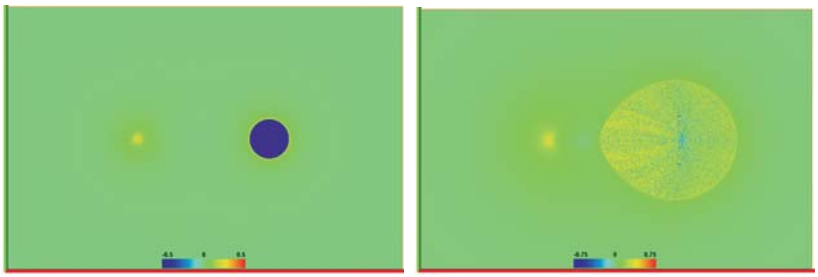

(a) (b)

Figure 6.5: FTLE field the dipole flow, (a) $m = 0.0628$; (b) $m = 0.628$.

6.3.1 Physical properties for investigation

Underlying a fluid phenomenon, there are various interactions and transports of different physical properties. The application of transport filter depends strongly on the investigated physical properties. These properties may be either conservative or not. With the application on different physical properties, the results of transport filter reflect different insights to the dynamical nature of fluid transport. For this chapter, we investigate several common physical properties and identify

some interesting structures on applications. General kinematic properties such as kinetic energy (KE), momentum, acceleration and local shear rate (LSRate)

$$LSRate = Det[\frac{1}{2}(\nabla \mathbf{v} + \nabla \mathbf{v}^T)]$$

which is determinant of the local shear rate tensor [KC04], are widely explored here. For the behaviors relating to vortexes, the properties such as vorticity

$$Vorticity = \nabla \times \mathbf{v}$$

and divergence

$$Div = \nabla \cdot \mathbf{v}$$

are analyzed. The popular Q-criteria and λ_2-critieria are also considered here. They are closely related to the Navier Stokes equations and reflect the amount of strain and vortical motions in the vector field. Due to this fact those quantities are the most popular among fluid mechanicists. Let $\nabla \mathbf{v}$ denote the gradient of the vector field. Then the strain tensor S is defined as its symmetric part $S = \frac{1}{2}(\nabla \mathbf{v} + \nabla \mathbf{v}^T)$. The antisymmetric part $\Omega = \nabla \mathbf{v} - \nabla \mathbf{v}^T)$ is closely related to vorticity. Then the Q-criterion defined by [Hun87], also known as the Okubo-Weiss criterion, is defined by

$$Q = \frac{1}{2}(\|\Omega\|^2 - \|S\|^2)$$

Q has a direct physical interpretation. Where $Q > 0$, vorticity dominates strain, so Hunt identified vortex regions with $Q > 0$. Note that $Q < 0$ indicates that the vector field is dominated by strain, making this criterion valuable in vector fields with distinct areas of strong vortical motions and areas of high strain. λ_2, derived by [JH95], is closely related to Q. Consider the three real eigenvalues $\lambda_1 \leq \lambda_2 \leq \lambda_3$ of the symmetric matrix $S^2 + \Omega^2$. In [JH95] it is deduced from the Navier Stokes equations that for a local pressure minimum two negative eigenvalues of this matrix are necessary. They define a vortex region where $\lambda_2 < 0$. In their work they show that $Q = .\frac{1}{2}(\lambda_1 + \lambda_2 + \lambda_3)$. Despite of this strong link they show that the λ_2-criterion detects vortex regions more reliably especially under a strong external strain. Nevertheless, the l2- criterion, unlike the Q-criterion, lacks a direct interpretation for regions where $\lambda_2 > 0$.

Based on our experience, there are no criteria to assess these properties. The selection of the properties currently depends on the interests of users. For reference, we compare the results of the advection filters with the corresponding LCS and observe the coherence and differences between them.

6.3.2 The Algorithm

Here we formulate the algorithm to visualize the finite-time transport structures of advection for flow fields.

1. Identify the physical properties of interest for investigation.
2. Pick up a certain time of interest and make a sampling in spatial domain.
3. Integrate path-lines from the sampling points in either forward or backward directions over a fixed time T.
4. Specify a convolution kernel and convolute the selected physical property field along path-lines.
5. Visualize the result field of the convolution and characterize the corresponding flow transport structures.

This algorithm needs some remarks:

To 1, this is the most important and flexible part of our approach. We currently select those properties which have been well applied in flow analysis. It can also be extended in future applications. There are no unique criteria for the selection, since different analysis in different applications may require different property fields. We provide users an interface for further exploration.

To 2, we try to make the sampling resolution as high as possible to above the Nyquist frequency, however we need to balance our computation power. During our analysis, we use an adaptive mechanism, if we find some interesting areas, we will zoom into that area with a higher sampling resolution.

To 3, in our approach, we consider only finite-time path-lines. The path-line integration is carried out in one direction within a fixed time T. We use $T > 0$ for the forward integration and $T < 0$ for the backward integration. Our approach shares the same problem as other finite-time approaches on the setting of *integration time* for path-lines. It is a tradeoff between the fact that we want to have the path-lines to be analyzed as long as possible and the property that most of the path-lines should be integrated over the same time without leaving the domain. We have carefully set the integration time during our applications. However, to the best of our knowledge, there is still no guarantee of the optimization of the integration time setting. We use 4th order Runge-Kutta integration for the path-line integration.

To 4, we currently consider a simple box kernel [SJM96] in our applications and restrict the analysis on the advection phenomenon of property transport. Diffusion

or radiation analysis may be added by modifying the convolution kernel.

To 5, typical scalar visualization techniques can be chosen for the visualization of convolution result fields. In this chapter, standard direct volume rendering and color coding are applied.

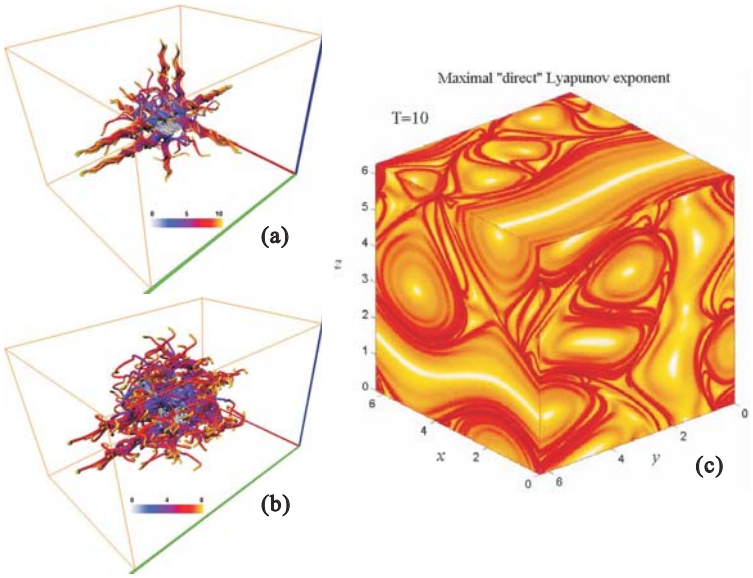

Figure 6.6: ABC flow: (a) Path-lines of steady ABC flow with integration time $T = 10$; (b) Path-lines of an unsteady ABC flow starting at $t = 0$ with integration time $T = 8$; (c) FTLE field of steady ABC flow [Hal01].

6.4 Applications

We applied our approach to a number of data sets. In our current applications, we consider only the physical properties mentioned above for convolution. Nevertheless, we can also identify several interesting flow transport structures from these properties which seem to hold even for different data sets.

Throughout this chapter, we use a temperature color coding to characterize the time information along path-lines.

ABC Flow

Figures 6.6 - 6.12 present results of analyzing two ABC flow fields (see section 4.6, Equation 4.12), which are solutions of Euler equation (Equation 2.24).

They are incompressible and inviscid. Here we set $A = \sqrt{3}, B = \sqrt{2}, C = 1$ for

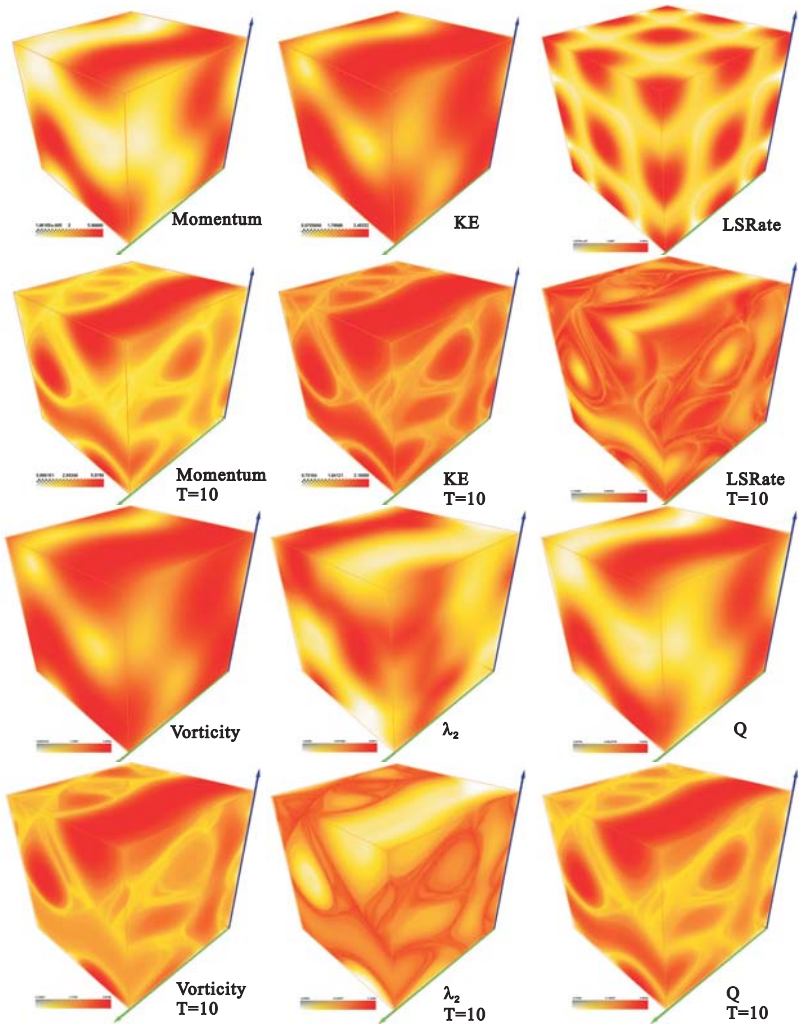

Figure 6.7: Steady ABC flow: the first and the third rows visualize the original property fields; the second and the fourth rows visualize the corresponding results of advection filter with integration time $T = 10$.

steady case and $A = \sqrt{3} + 0.5t\sin(2\pi t), B = \sqrt{2}, C = 1$ for unsteady case. We consider the spatial domain $D = [0, 2\pi]^3$ and used a sampling of $128 \times 128 \times 128$. Since this field is also defined outside the domain, we can integrate every path-line for a full time, even though it leaves the domain.

Figure 6.6a shows some integrated path-lines for the steady ABC field with the integration time $T = 10$ while Figure 6.6b shows some integrated path-lines for the unsteady ABC field with the integration time $T = 8$. Figure 6.6c is one visual-

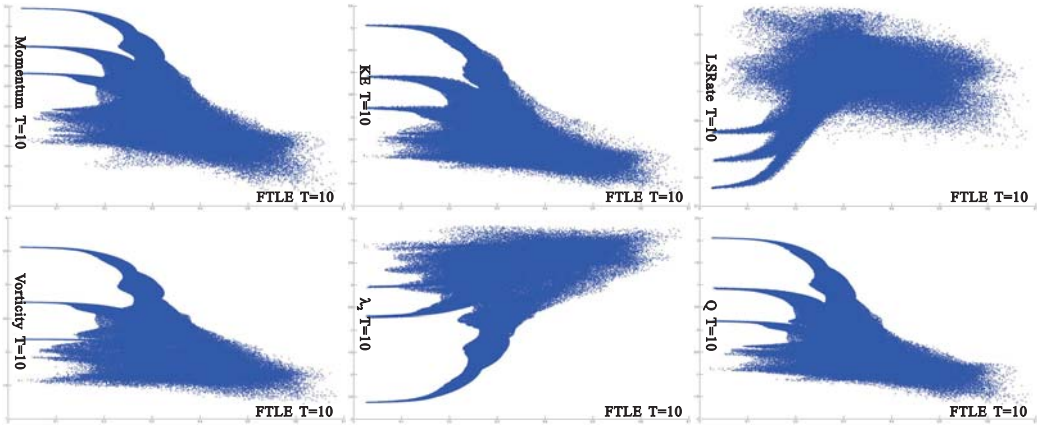

Figure 6.8: Steady ABC flow: Scatter plots of the advection filter convoluted fields of different physical properties and the corresponding FTLE fields.

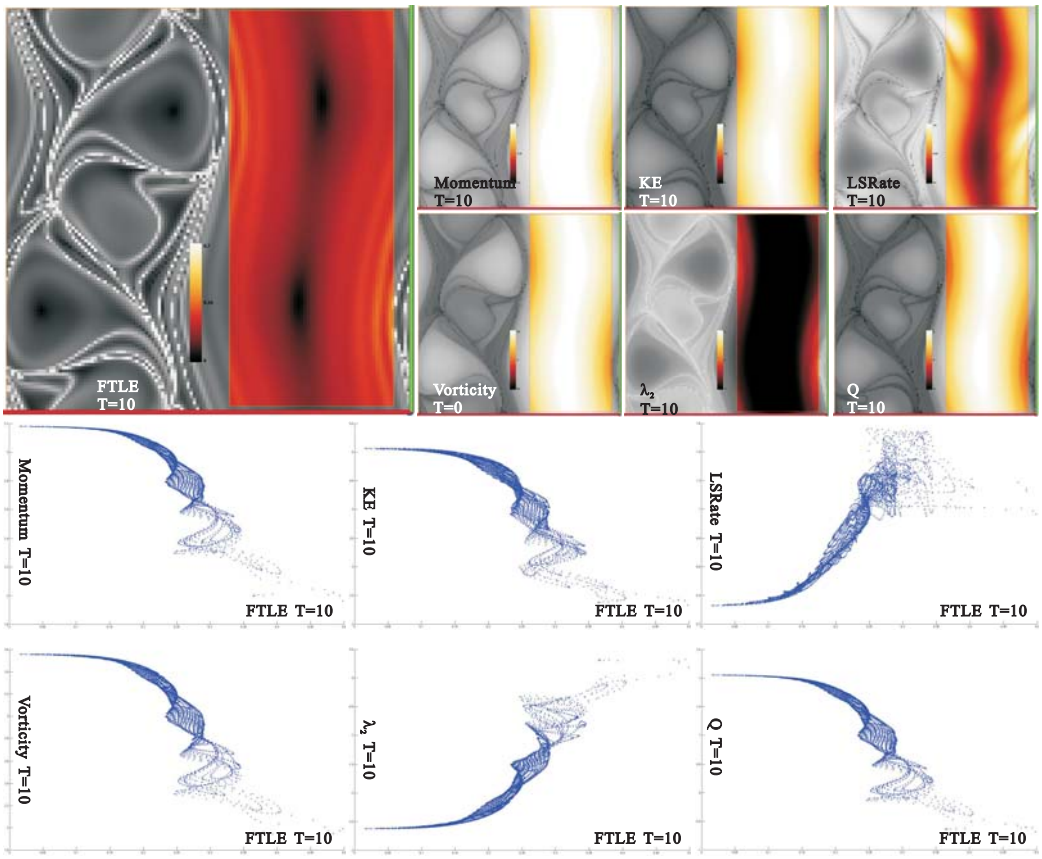

Figure 6.9: Steady ABC flow: select an area at slice $z = 2\pi$, the upper subfigures visualize the fields on that area; The lower subfigures visualize scatter plots of these fields and the corresponding FTLE on that area.

ization of the distribution of the FTLE fields of the steady ABC flow [Hal01]. The corresponding LCS of the steady ABC flow can be visualized through this FTLE field.

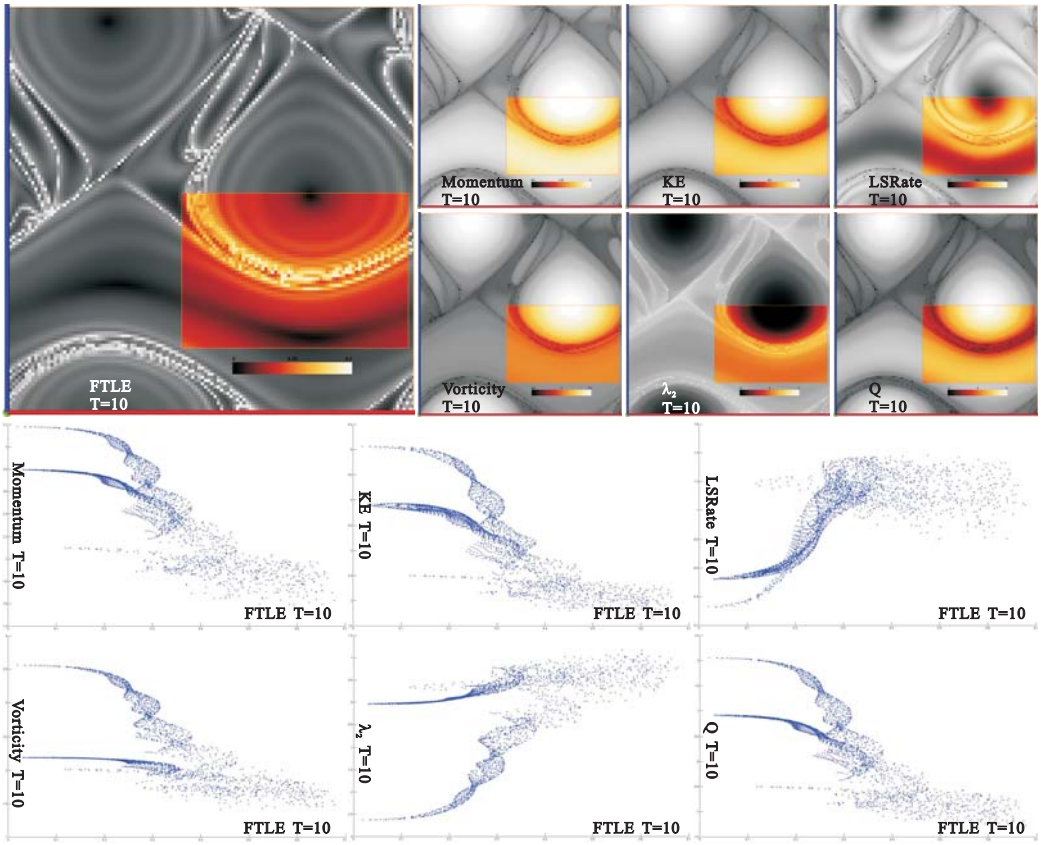

Figure 6.10: Steady ABC flow: select an area at slice $y = 2\pi$, the upper subfigures visualize the fields on that area; The lower subfigures visualize scatter plots of these fields and the corresponding FTLE on that area.

The upper left of Figure 6.7 visualizes the local momentum field. We apply advection filter over momentum and visualize the distribution in the right of the second row of Figure 6.7. It is obvious to see that the advection structures presented in the convoluted momentum field follows strictly with the LCS. We observe that the local maximums in FTLE field corresponds to the local minimums in the convoluted momentum field. It is reasonable that near LCS there is generally weak momentum advection. Similarly, the middle of the first row of Figure 6.7 shows the local kinetic energy field and the middle of the second row of Figure 6.7 shows the convoluted kinetic energy field after applying advection filter. We can observe the strong similarity again between the kinetic energy advection structure and the

LCS.

For the analysis of the correspondence, we make scatter plots of these corresponding fields in Figure 6.8. The upper left shows a scatter plot between the FTLE field and the advection filtered momentum field. Although the relations of these two fields can not be described using simple global functions, we can still see the general inverse mapping between FTLE and convoluted momentum field. Further more, we can see that this mapping is formed with several bundle structures which may indicate local correlations.

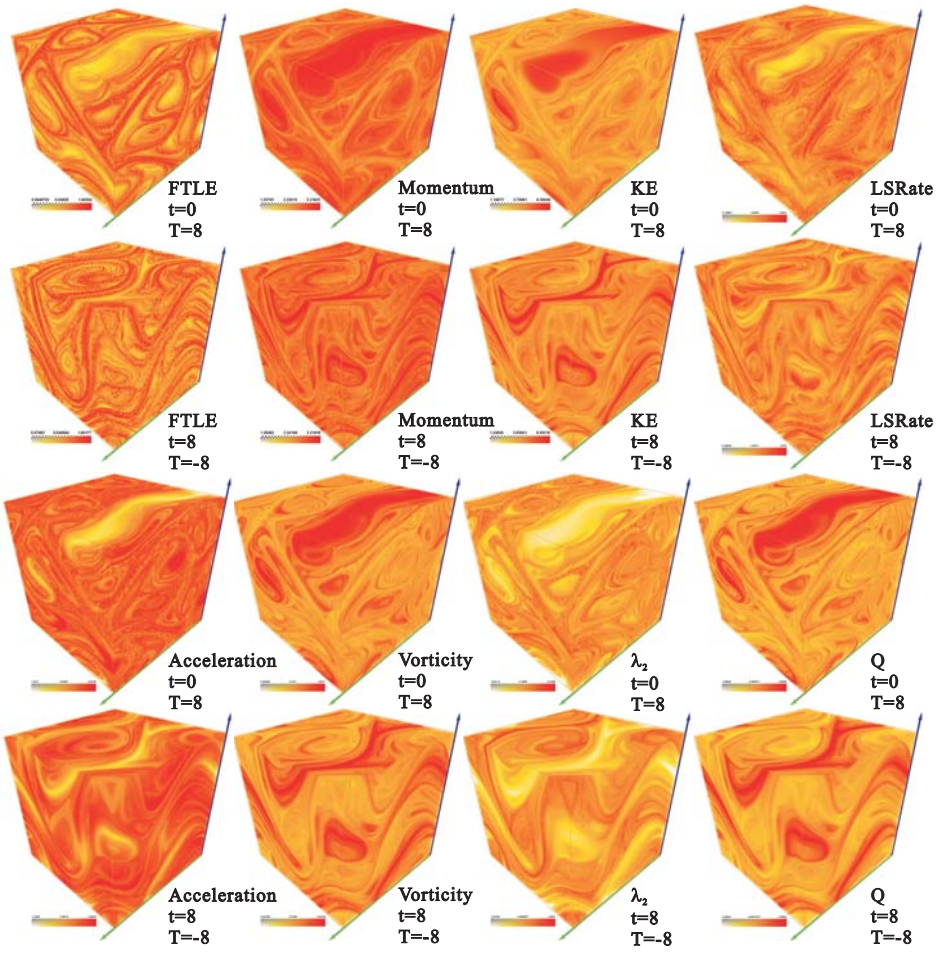

Figure 6.11: Unsteady ABC Flow: The left of the first two rows visualize the FTLE fields while the others visualize the advection filter convoluted results of different properties; Row 1 and 3 start at $t = 0$ with integration time $T = 8$; Row 2 and 4 start at $t = 8$ with integration time $T = -8$.

For the further analysis of these local correlations, we select some areas with

simple obvious patterns and observe the scatter plot of these two fields on the restricted area. Figure6.9 selects an area on an XY slice. From the upper left of the scatter plots in Figure 6.9, we can see clearly that the two fields on the selected areas have strong inverse correlations, though they are not linearly related. In Figure 6.10, an area on an XZ slice is selected. For the selection on Figure 6.10, we can see clearly two types of mappings, which correspond to the two different types of similarities between the momentum advection structure and the LCS on the selected area. As for the case of kinetic energy, we can see the same correlations for the two selected areas.

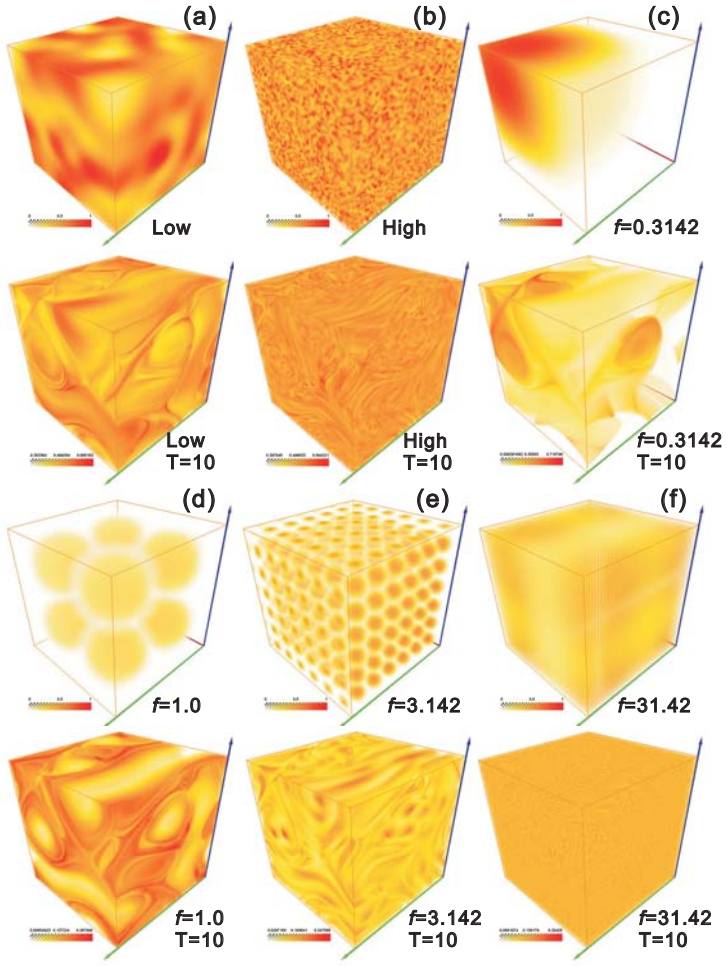

Figure 6.12: Advection filter over generic fields. For each group, the upper visualizes the original field and the lower visualizes the corresponding convoluted result. Group a and b test two random noise field; Group c-f test a normal function field $g(x,y,z)$ of different frequencies f.

Similar analyses of other physical properties (local shear rate, vorticity, λ_2-criteria, Q-criteria) are illustrated in the remaining subfigures of Figure 6.7-6.9. We can see again the similarities between the advection structures and the LCS. Though the relations of these similarities behave differently, the local correlations between the patterns are clear, which agree with the visual observations between the corresponding fields.

In Figure 6.11 we apply our approach to the unsteady ABC field and compared them with the classical FTLE fields. The left of the first two rows of Figure 6.11 visualize FTLE fields computed at time $t = 0$ and $t = 8$ in forward and backward direction with the convolution time $T = 8$ and $T = -8$. LCS can be visualized through these FTLE fields.

We investigated the following properties, momentum, kinetic energy, local shear rate, vorticity, λ_2-criteria, Q-criteria. The corresponding distributions of advection filter over the physical properties are visualized in the rest of Figure 6.11. The transport structures uncovered by these distributions present the same strong similarity with the corresponding LCS as the steady case.

We can see for both steady and unsteady ABC flow, either momentum or kinetic energy transport structures have significant similarity with the LCS. It is reasonable that in this ABC case, the fluids are inviscid and there is no dissipation during the flow advection. Thus the fluid transport is well behaved and structurally there is no difference between material transport, momentum transport or kinetic energy transport.

We observe that for any properties of the ABC flow, either for steady or the unsteady case, the advection structures present significant similarities to the LCS structure. It is interesting that we carry out further analysis for the advection filter over general properties. If we apply our advection filter over generic fields, we may also approach to the structures which have some similarity to LCS. Though they have no obvious physical meaning, they still reveal some intrinsic structures behind the ideal flow. In Figure 6.12, we apply our approach to different generic fields. Figure 6.12a and b compare the results of advection filter over two random noise fields while Figure 6.12c-f compare the results of advection filter over $g(x,y,z) = sin^2(fx)sin^2(fy)sin^2(fz)$ with different frequency f.

The LCS look-like structures appear when the dominant frequency of the generic fields approaching to the inherent frequency of ABC flow. It turns out that the concentration of generic substance advection tends to approaching to the intrinsic structures of flow transport and the more correlation between a flow field and a property field, the better for Path-line LIC to uncover these intrinsic structures.

2D Time-dependent Cylinder Flow

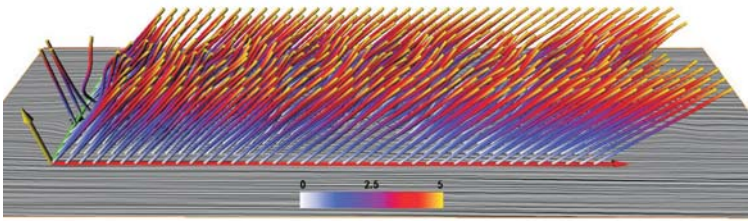

(a)

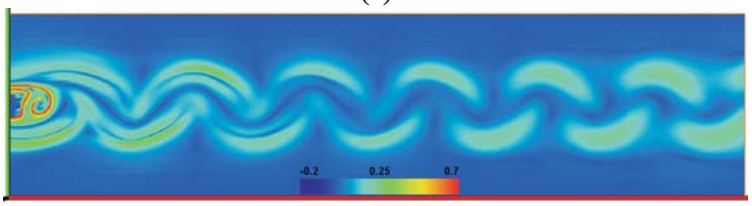

(b)

Figure 6.13: 2D dynamical cylinder flow: (a) Path-lines starting at $t = 0$ with integration time $T = 5$; (b) FTLE field.

Figure 6.13 and 6.14 present some results of analyzing a 2D time-dependent version of the flow behind a circular cylinder (see section 5.3). This is an incompressible laminar viscous flow [TWHS05]. The spatial domain of the data set is $[-9, 49.5] \times [-11, 11]$ and it is temporal periodic flow with one period $[0, 32]$. We focus the consideration on the area behind the cylinder ($[0, 28] \times [-3.5, 3.5]$) and make a sampling of 1000×250. For the result in the figures, we set an integration time $T = 5$. Figure 6.13a shows a visualization of some integrated path-lines starting at $t = 0$. Figure 6.13b shows a color coding of the corresponding FTLE field which visualizes the underlying LCS.

For the advection filter, we also consider the physical properties mentioned above, momentum, kinetic energy, local shear rate, vorticity, λ_2-criteria, Q-criteria. We apply our advection filter over them along path-lines and visualize them using color coding in rows 2, 4 and 6 of Figure 6.14. The upper left shows the original momentum field and the left of the second row visualizes the corresponding result after applying advection filter. We can see that the transport structures are significantly different from local structures. The low values of the result field of advection filter indicate weak flow advections. We can observe that the center area behind the cylinder has strong momentum advection at the beginning while it turns to weak advection as the flow moves forward. Here we note that the momentum advection structures presented in the result fields of advection filter have some similarities with the LCS at the areas near the location of the circular cylin-

der. The similarity decreases when the flow travels forward. This flow is viscous and there exists momentum dissipation during the transport. For the case of kinetic energy, we can see obviously the same similarities as for the momentum case, while for the other properties, the correlations are not so obvious.

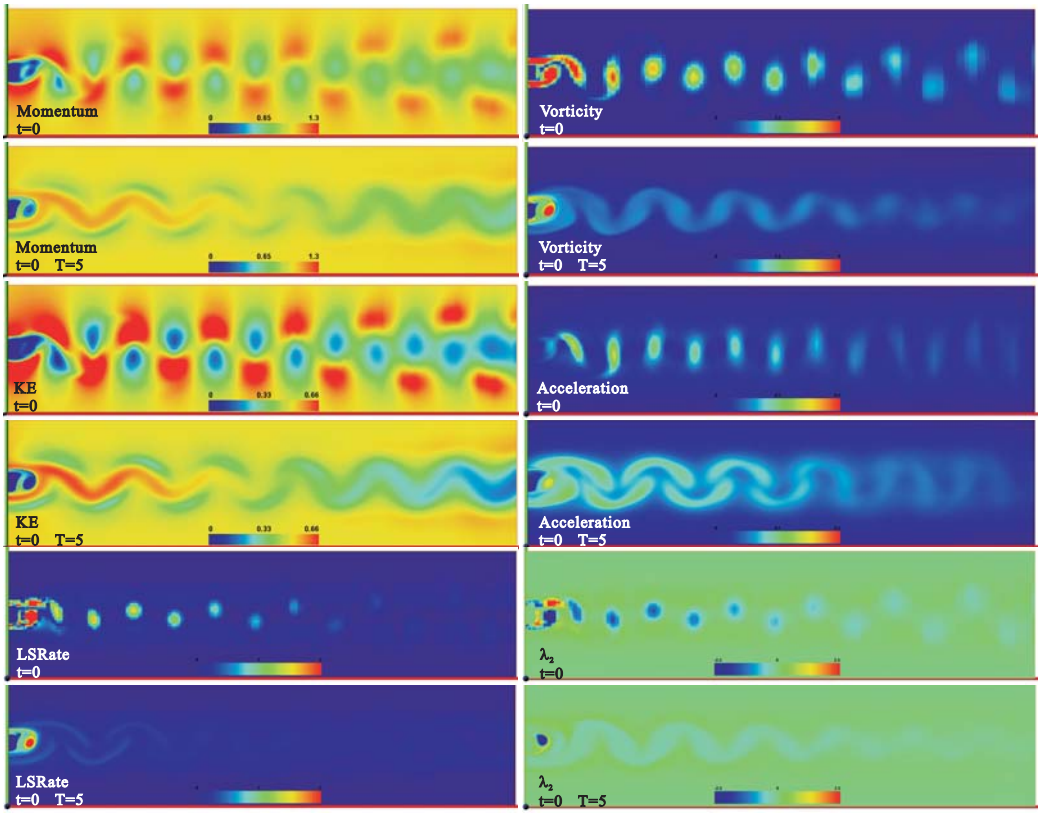

Figure 6.14: 2D dynamical cylinder flow: Rows 1, 3 and 5 visualize the local property fields; Rows 2, 4 and 6 visualize the corresponding advection filter convolution results.

This means that the momentum and kinetic energy advection have similar transport behavior with the material advection at the early stage and these property transport structures diffuse gradually as the increasing of dissipation effects during the flow transport. Compared the two property transport structures, we can also see that the momentum transport structures diffuse slower than the kinetic energy transport structures. It is interesting that these two properties are conservative transport properties and their structures appear strong similarities to the LCS for this cylinder flow.

For the analysis of the similarities, we pick up an area with strong similarity and make the scatter plots in Figure 6.15. We can see again the clear mapping bundles

for momentum and kinetic energy from the scatter plots during the local analysis, while for other properties, the correlations are not so obvious. It doesn't mean that either momentum or kinetic energy is better than other properties. The comparing with LCS is only a reference for our structures, which are not necessarily correlated to LCS. The choosing the properties still depends the interests of the users and an assessment criteria is still leaves for future works. However, it is interesting to compare the similarity or difference of various flow transport structures which contributes better understanding of the complex dynamical phenomena behind a flow.

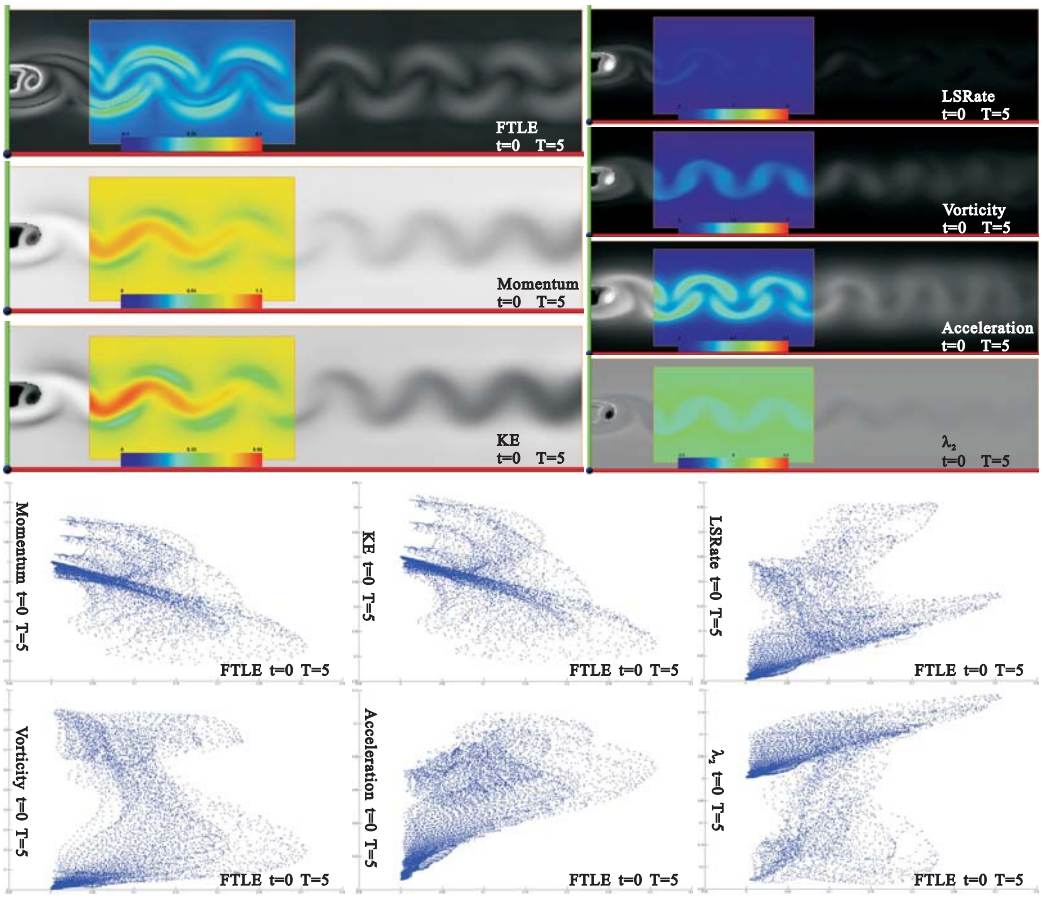

Figure 6.15: 2D dynamical cylinder flow: select an area on slice $t = 0$, the upper subfigures visualize the fields on the selected area; The lower subfigures visualize scatter plots of these fields and the corresponding FTLE on that area.

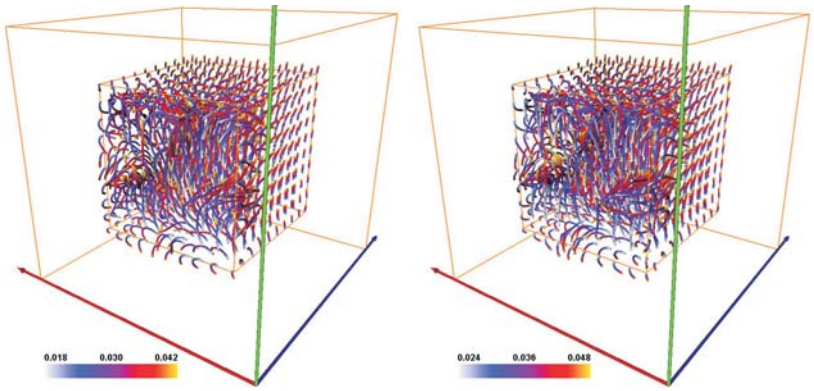

(a) (b)

Figure 6.16: Path-lines of five jet flow starting at: (a) $t = 0.018s$; (b) $t = 0.024s$.

Five Jet Flow

Figure 6.16 and 6.17 show an application of our approach on a 3D time-dependent flow which simulates five jets flying through a domain [FMA05]. The spatial domain of the data set is $[0, 3.81m]^3$ and the temporal domain is $[0, 0.06s]$. The inflow velocity is $100m/s$. This data set is a compressible flow data for which the FTLE fields are not available for LCS. We focus our consideration on the center area ($[0.8m, 3.01m]^3$) where the jets fly through and make a sampling of $100 \times 100 \times 100$. The following result show two analysis starting at $t = 0.018s$ and $t = 0.024s$ with the integration time $T = 0.018s$ and $T = 0.024s$. Figure 6.16 a and b show some integrated path-lines with the integration time $T = 0.024s$.

The first column of Figure 6.17 shows an application of our approach on the density field starting at $t = 0.018s$. The left visualizes the local density field at the starting time. The middle and right visualize the result fields of advection filter with the integration time $T = 0.018s$ and $T = 0.024s$. The structures appeared in the convoluted density result show the structure nature of the mass advection in the flow. The high value area of the result field indicates the region with strong mass advection which describes the trend of mass concentration while the low value area of the result field indicates the region of weak mass advection and the possible separation of mass advection. We can see that these mass transport structures present significant different information than the original local property field and depend little on the integration time when it is integrated long enough to uncover the structure. It is notable that even in a symmetric local setting, the underlying mass transport may behave asymmetrically [KC04, LL87]. Similarly the second column show a advection filter analysis of the density field starting at $t = 0.024s$. We can see again that the mass transport structures differ significantly from local

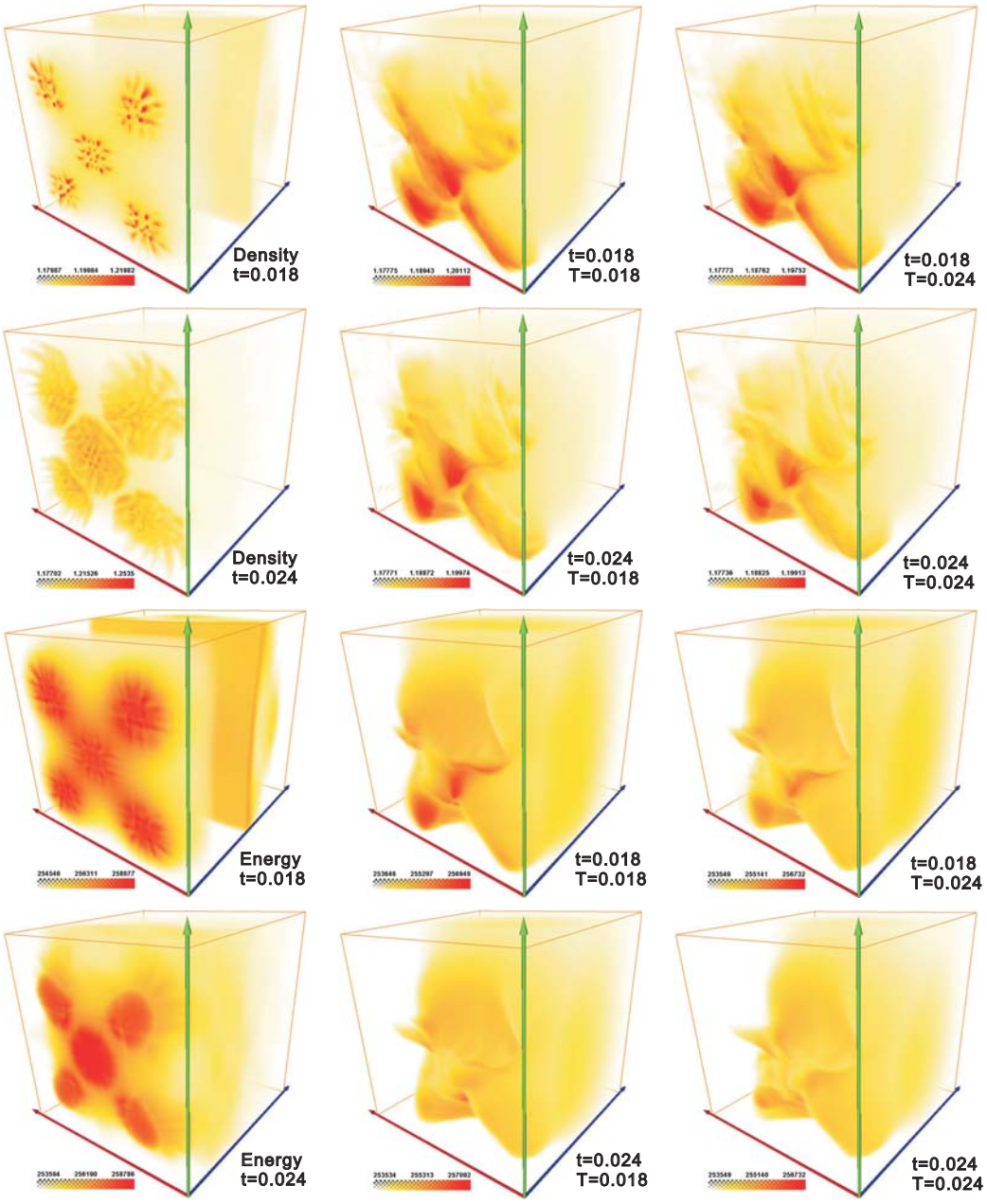

Figure 6.17: Five jet flow: The left visualizes local density field at starting time; The middle visualizes the corresponding result of advection filter with $T = 0.018s$; The right visualizes the corresponding result of advection filter with $T = 0.024s$.

property structures and depend little on the integration time. The asymmetry turns out again during the underlying mass advection. We can also observe some coherency between the two groups of transport structures and these structures reflect the intrinsic transport behavior of the underlying mass advection.

In the third and fourth column of Figure 6.17, we apply our advection filter approach to the corresponding energy field of the five jet data set. The structures appearing in the convoluted result field of advection filter figure out the underlying energy transport behavior. The high value area of the result field indicates the trend of energy concentration while the low value area of the result field indicates weak energy advection and the possible separation of the underlying energy advection. These energy transport structures are inherently asymmetric though the local field is symmetric. They have some coherency and depend weakly on the integration time. Through these structures, we can observe the intrinsic transport behavior of the underlying energy advection.

It is interesting to observe the difference between the mass transport structures and the corresponding energy transport structures. The visualization and comparison of different transport structures significantly improve the understanding of the complex phenomena of dynamical flow transport.

6.5 Conclusion

To getting insights into the dynamical transport behavior of a flow processes is still a challenging problem. Either property or motion provides separate view points towards the dynamical nature. Our approach did a trial to combine the property analysis and the motion analysis, and offers a higher level structure view of the dynamical behaviors underlying flow transport. This combination is constructed by applying certain transport filter over physical property fields. For advection, this transport filter is equivalent to line integral convolution along path-lines. In particular, we contribute the following work:

- We proposed an approach to identify the finite-time flow transport structures for physical properties through transport filters.
- We formulated the transport filter for advection behavior as convoluting a correlated physical property field along finite-time path-lines.
- We applied our approach to a number of data sets and present some new insights into the dynamical behaviors.

However, we are not able to achieve accuracy in both the static information space and the dynamic information space. The observation of dynamical transport behaviors may come to the reduction of static details or even loss of some information. Nevertheless, this dynamical transport information presents different intrinsic view into the transport phenomenon and contributes significantly to visual understanding of fluid dynamics. Besides, in this chapter, we only focus on the visual analysis of the underlying transport structures, the theoretical analysis or proof is beyond our scope. For the future work, we could consider the variant of convolution kernels to include the analysis of non advection transport behaviors. It is also worth to implement the general transport filters directly from partial differential equations. For our computation, we haven't considered any acceleration algorithm for the convolution. It is desired to do a further acceleration for interactive application.

Chapter 7

Conclusions and Future Works

A new picture of a fluid process delivers new information about the complex phenomenon. Path-line oriented visualization techniques provide significantly different insights into the dynamical nature of a flow field and contribute a natural understanding of the important characteristics of fluid motion.

7.1 Conclusions

In this thesis we presented several novel flow visualization approaches for dynamical flow fields. We focused on the behavior of path-lines and developed algorithms to identify new features and structures relating to them. The following points summarize the main results and contributions of this thesis:

1. We introduced a topological approach to analyzing the asymptotic behavior of path-lines by considering a periodic time-dependent vector fields. Critical path-lines are defined, extracted and classified and the basins from which the path-lines converge to the critical path-lines are computed in forward or backward integration.

2. We offered an alternative solution to extract the separation surfaces of the path-line oriented topology. An image analysis method is applied to extract the seeding curves and the separation surfaces are integrated from these seeding curves with step advancing super sampling adjustment.

3. We introduced an information visualization based approach to analyze the behaviors of path-lines. A number of local and global attributes of path-

lines, which we expect to contain relevant information about the path-line behaviors, are identified. These attributes are interactively analyzed by using an approach from information visualization and the results are used to steering a 3D path-line visualization. Particularly, we offered a flexible interface for interactive visual analysis of dynamical flow behaviors.

4. We investigated the transport phenomenon underlying a flow process and proposed an approach to visualize the finite-time transport structures of physical properties. A transport filter is introduced to integrate the transport history of the corresponding properties. For advection behavior, the transport filter is constructed as a path-line integral convolution with the correlated physical property fields. The finite-time transport structures of property advection is identified from the convoluted results of advection filters.

5. We applied our approaches to a number of data sets and proved that these path-line oriented visualization results present significantly different information of the dynamical flow behavior and contribute new insights into the complex nature of unsteady flow fields.

7.2 Future Works

The research described in this thesis raised several questions which would wait for further research. We sketch several ideas for future works:

1. The current topological method based on asymptotic path-line behavior is limited only to periodic flow fields. A general asymptotic topological segmentation based on path-line for non-periodic flow fields is still a difficult topic. Besides, our current segmentation is only specified for periodic 2D time-dependent vector fields, it is also an open topic to extend this to 3D time-dependent vector fields.

2. The image analysis approach for current separation surface extraction is limited to the regular basin structures. If the basins are quite irregular and discontinuous, the seeding curve extraction will fail. A robust surface extraction algorithm is desired for further research. Also the efficiency needs to be improved for the separation surface integration.

3. We only proposed an interactive interface for visual analysis of path-lines behaviors. In practice, not all path-line attributes gives useful information. It is still difficult to identify proper path-line attributes for the visualization

of different data sets. More attributes need to be identified for real application. Besides, the information visualization techniques still needs to be assessed for different attribute sets. Which needs more practical support for this approach.

4. We only focus on the visual analysis of the underlying transport structures, the theoretical analysis or proof of these transport structures are still left for theoretical fluid analysis. Our current approach only consider advection transport behavior. The variant of convolution kernels needs to be considered to include non advection transport behaviors. Also it is worth to doing a further acceleration for interactive application.

5. An implementation of general transport filter directly from the partial different equations is desired. A flexible analysis of fluid transport with different mechanisms may contribute a better understanding of the complex dynamical phenomena underlying a flow process.

Bibliography

[And95] ANDERSON J. D.: *Computational Fluid Dynamics. The Basics with Applications*. McGraw-Hill, 1995.

[AS92] ABRAHAM L., SHAW K.: *Dynamics, The Geometry of Behaviour*. Addison-Wesley, 1992.

[Bak91] BAKKER P. G.: *Bifurcations in Flow Patterns (Theory and Applications of Transport in Porous Media)*. Kluwer Academic Publishers, 1991.

[Bat67] BATCHELOR G. K.: *An Introduction to Fluid Dynamics*. Cambridge University Press, 1967.

[BD14] BLACK N. H., DAVIS H. N.: *Practical Physics*. The Macmillan Company, 1914.

[BMH01] BISCHI G.-I., MROZ L., HAUSER H.: Studying basin bifurcations in nonlinear triopoly games by using 3d visualization. *Journal Nonlinear Analysis 47*, 8 (2001), 5325–5341.

[BPR00] BECKER J., PREUSSER T., RUMPF M.: PDE methods in flow simulation post processing. *Computing and Visualization in Science 3*, 3 (2000), 159–167.

[BS95] BANKS D., SINGER B.: A predictor-corrector technique for visualizing unsteady flow. *IEEE Transactions on Visualization and Computer Graphics 1*, 2 (1995), 151–163.

[CL93] CABRAL B., LEEDOM L.: Imaging vector fields using line integral convolution. *Computer Graphics 27* (1993), 263–272.

[CLRS01] CORMEN T. H., LEISERSON C. E., RIVEST R. L., STEIN C.: *Introduction to Algorithms*. MIT Press, 2001.

[CSJ] CARABALLO E., SAMIMY M., J D.: Low dimensional modeling of flow for closed-loop flow control. AIAA Paper 2003-0059.

[DGH03] DOLEISCH H., GASSER M., HAUSER H.: Interactive feature specification for focus+context visualization of complex simulation data. In *VISSYM '03: Proceedings of the symposium on Data visualisation 2003* (2003), pp. 239–248.

[DH02] DOLEISCH H., HAUSER H.: Smooth brushing for focus+context visualization of simulation data in 3D. In *Proc. WSCG* (2002), pp. 147–154.

[dLvL99] DE LEEUW W., VAN LIERE R.: Visualization of global flow structures using multiple levels of topology. In *Data Visualization 1999. Proc. VisSym 99* (1999), pp. 45–52.

[dLvW93] DE LEEUW W., VAN WIJK J.: A probe for local flow field visualization. In *Proc. IEEE Visualization '93* (Los Alamitos, 1993), IEEE Computer Society Press, pp. 39–45.

[DMG*05] DOLEISCH H., MAYER M., GASSER M., PRIESCHING P., HAUSER H.: Interactive feature specification for simulation data on time-varying grids. In *Simulation and Visualization (SimVis '05)* (2005), pp. 291–304.

[DMH04] DOLEISCH H., MUIGG P., HAUSER H.: Interactive visual analysis of hurricane isabel. *VRVis Technical Report 2004-058* (2004).

[Dyk82] DYKE M. V.: *An Album of Fluid Motion*. Parabolic Press, 1982.

[FC95] FORSSELL L. K., COHEN S. D.: Using line integral convolution for flow visualization: Curvilinear grids, variable-speed animation, and unsteady flows. *IEEE Transactions on Visualization and Computer Graphics 1*, 2 (1995), 133–141.

[Flu02] FLUENT: Formula 1 external aerodynamics, 2002.

[FMA05] FOUT N., MA K.-L., AHRENS J.: Time-varying multivariate volume data reduction. In *Proc. ACM Symposium on Applied Computing* (March 2005), pp. 1224–1230.

[FvDFH96] FOLEY J., VAN DAM A., FEINER S., HUGHES J.: *Computer Graphics, Principles and Practice*. Addison-Wesley Publishing Company, Reading Massachusetts, 1996.

[GGTH07] GARTH C., GERHARDT F., TRICOCHE X., HAGEN H.: Efficient computation and visualization of coherent structures in fluid flow

applications. *IEEE Transactions on Visualization and Computer Graphics* (2007).

[GJ04] GRUCHALLA K., J. M.: Immersive visualization of the hurricane isabel dataset.

[GLT*07] GARTH C., LI G., TRICOCHE X., HANSEN C. D., HAGEN H.: Visualization of coherent structures in transient flow. In *TopoInVis 07* (2007).

[GTS04] GARTH C., TRICOCHE X., SCHEUERMANN G.: Tracking of vector field singularities in unstructured 3D time-dependent datasets. In *Proc. IEEE Visualization '04* (2004), pp. 329–336.

[GW92] GONZALEZ R. C., WOODS R. E.: *Digital Image Processing*, 3rd ed. Addison-Wesley, 1992.

[Hal00] HALLER G.: Finding finite-time invariant manifolds in two-dimensional velocity fields. *Chaos 10*, 1 (2000), 99–108.

[Hal01] HALLER G.: Distinguished material surfaces and coherent structures in three-dimensional fluid flows. *Physica D 149* (2001), 248–277.

[Hal02] HALLER G.: Lagrangian coherent structures from approximate velocity data. *Physics of Fluids 14* (6 2002), 1851–1861.

[Hau04] HAUSER H.: *Generalizing Focus+Context Visualization*. Habilitation Thesis, 2004.

[Hau06] HAUSER H.: Interactive visual analysis - an opportunity for industrial simulation. In *SimVis* (2006), Schulze T., Horton G., Preim B., Schlechtweg S., (Eds.), SCS Publishing House e.V, pp. 1–6.

[HH89] HELMAN J., HESSELINK L.: Representation and display of vector field topology in fluid flow data sets. *IEEE Computer 22*, 8 (August 1989), 27–36.

[HJ05] HANSEN C. D., JOHNSON C. R.: *The Visualization Handbook*. Academic Press, 2005.

[HLD*02] HAUSER H., LARAMEE R. S., DOLEISCH H., POST F. H., VROLIJK B.: The state of the art in flow visualization, part 1: Direct, texture-based, and geometric techniques, 2002.

[HMBG01] HAUSER H., MROZ L., BISCHI G.-I., GRÖLLER E.: Two-level volume rendering. *IEEE Transactions on Computer Graphics 7*, 3 (2001), 242–252.

[Huc94] HUCHO W.-H.: *Aerodynamik des Automobils. Eine Brücke von der Strömungsmechanik zur Fahrzeugtechnik*. Springer, 1994.

[Hun87] HUNT J.: Vorticity and vortex dynamics in complex turbulent flows. *Proc CANCAM, Trans. Can. Soc. Mec. Engrs 11* (1987), 21.

[HY00] HALLER G., YUAN G.: Lagrangian coherent structures and mixing in two-dimensional turbulence. *Physica D 147*, 3-4 (2000), 352–370.

[JEH01] JOBARD B., ERLEBACHER G., HUSSAINI M. Y.: Lagrangian-eulerian advection for unsteady flow visualization. In *Proceedings of the Conference on Visualization 2001 (VIS-01)* (Piscataway, NJ, Oct. 21–26 2001), Ertl T., Joy K., Varshney A., (Eds.), IEEE Computer Society, pp. 53–60.

[JEH02] JOBARD B., ERLEBACHER G., HUSSAINI M. Y.: Lagrangian-eulerian advection of noise and dye textures for unsteady flow visualization. *IEEE Transactions on Visualization and Computer Graphics 8*, 3 (2002), 211–222.

[JH95] JEONG J., HUSSAIN F.: On the identification of a vortex. *J. Fluid Mechanics 285* (1995), 69–94.

[JKS95] JAIN R. C., KASTURI R., SCHUNCK B. G.: *Machine Vision*. McGraw-Hill, 1995.

[Joh04] JOHNSON C.: Top scientific visualization research problems. *IEEE Comput. Graph. Appl. 24*, 4 (2004), 13–17.

[KC04] KUNDU P. K., COHEN I. M.: *Fluid Mechanics*. Academic Press, 2004.

[Kre00] KREITH F.: *Fluid Mechanics*. CRC Press, 2000.

[LDS90] LEVY Y., DEGANI D., SEGINER A.: Graphical visualization of vortical flows by means of helicity. *AIAA Journal 28*, 8 (1990), 1347–1352.

[Lea07] LEAL L. G.: *Advanced Transport Phenomena: Fluid Mechanics and Convective Transport Processes*. Cambridge University Press, 2007.

[LH99] LOVELY D., HAIMES R.: Shock detection from computational fluid dynamics results, 1999.

[LHD*04] LARAMEE R. S., HAUSER H., DOLEISCH H., VROLIJK B., POST F. H., WEISKOPF D.: The state of the art in flow visualization: Dense and texture-based techniques. *Comput. Graph. Forum 23*, 2 (2004), 203–222.

[Lia66] LIAPUNOV A. M.: *Stability of Motion*. Academic Press, New York, 1966.

[LJH03] LARAMEE R. S., JOBARD B., HAUSER H.: Image space based visualization of unsteady flow on surfaces. In *IEEE Visualization* (2003), Turk G., van Wijk J. J., II R. J. M., (Eds.), IEEE Computer Society, pp. 131–138.

[LKG98] LÖFFELMANN H., KUČERA T., GRÖLLER E.: Visualizing poincaré maps together with the underlying flow. In *Proc. VisMath '97* (1998), pp. 315–328.

[LL87] LANDAU L. D., LIFSHITZ E. M.: *Fluid Mechanics*. Butterworth-Heinemann, 1987.

[Löf98] LÖFFELMANN H.: *Visualizing Local Properties and Characteristic Structures of Dynamical Systems*. PhD thesis, Vienna Univserity of Technology, 1998.

[Mer74] MERZKIRCH W.: *Flow Visualization*. Academic Press, 1974.

[MJJ*05] MATKOVIC K., JELOVIC M., JURIC J., KONYHA Z., GRACANIN D.: Interactive visual analysis end exploration of injection systems simulations. In *IEEE Visualization 2005* (Oct. 2005), C. T. Silva E. Gröller H. R., (Ed.), IEEE, pp. 391–398.

[MRV96] MA K.-L., ROSENDALE J. V., VERMEER W.: 3d shock wave visualization on unstructured grids. In *VVS '96: Proceedings of the 1996 symposium on Volume visualization* (Piscataway, NJ, USA, 1996), IEEE Press, pp. 87–ff.

[NHM97] NIELSON G. M., HAGEN H., MÜLLER H. (Eds.):. *Scientific Visualization, Overviews, Methodologies, and Techniques* (1997), IEEE Computer Society.

[Oer02] OERTEL H.: *Prandtl - Führer durch die Strömungslehre. Grundlagen und Phänomene*. Vieweg Verlag, 2002.

[PH99] POJE A. C., HALLER G.: Geometry of cross-stream lagrangian mixing in a double gyre ocean model. *J.Phys.Oceanogr. 29* (1999), 1649–1665.

[PR99a] PEIKERT R., ROTH M.: The parallel vectors operator - a vector field visualization primitive. In *Proc. IEEE Visualization 99* (1999), pp. 263–270.

[PR99b] PREUSSER T., RUMPF M.: Anisotropic nonlinear diffusion in flow visualization. In *IEEE Visualization* (1999), pp. 325–332.

[PS93] PAGENDARM H. G., SEITZ B.: An algorithm for detection and visualization of discontinuities in scientific data fields applied to flow data with shock waves. *Computer Graphics Forum* (1993), 161–177.

[PVH*03] POST F. H., VROLIJK B., HAUSER H., LARAMEE R. S., DOLEISCH H.: The state of the art in flow visualisation: Feature extraction and tracking. *Comput. Graph. Forum 22*, 4 (2003), 775–792.

[PvW93] POST F., VAN WALSUM T.: Fluid flow visualization. In *Focus on Scientific Visualization*, Hagen H., Müller H., Nielson G., (Eds.). Springer, Berlin, 1993, pp. 1–40.

[PWPS95] POST F. J., WALSUM T. V., POST F. H., SILVER D.: Iconic techniques for feature visualization. In *Proc. IEEE Visualization '95* (Washington, DC, USA, 1995), IEEE Computer Society, p. 288.

[Rob91] ROBINSON S.: Coherent motions in the turbulent boundary layer. *Ann. Rev. Fluid Mech. 23* (1991), 601–639.

[RP96] ROTH M., PEIKERT R.: Flow visualization for turbomachinery design. In *Proc. Visualization 96* (1996), pp. 381–384.

[RSHTE99] REZK-SALAMA C., HASTREITER P., TEITZEL C., ERTL T.: Interactive exploration of volume line integral convolution based on 3D-texture mapping. In *Proc. IEEE Visualization '99* (Washington - Brussels - Tokyo, Oct. 1999), IEEE, pp. 233–240.

[SAE93] SHIRMAN L. A., ABI-EZZI S. S.: The cone of normals technique for fast processing of curved patches. *Comput. Graph. Forum 12*, 3 (1993), 261–272.

[SH95a] STALLING D., HEGE H.: Fast and resolution independent line integral convolution. *ACM Siggraph '95* (1995), 249–256. Los Angeles.

[SH95b] SUJUDI D., HAIMES R.: *Identification of swirling flow in 3D vector fields*. Tech. rep., Department of Aeronautics and Astronautics, MIT, 1995. AIAA Paper 95-1715.

[SHK*97] SCHEUERMANN G., HAGEN H., KRÜGER H., MENZEL M., ROCKWOOD A.: Visualization of higher order singularities in vector fields. In *Proc. IEEE Visualization '97* (1997), Yagel R., Hagen H., (Eds.), pp. 67–74.

[SJM96] SHEN H.-W., JOHNSON C. R., MA K.-L.: Visualizing vector fields using line integral convolution and dye advection. In *Proc. Symposium on Volume Visualization* (New York, Oct. 1996), ACM Press, pp. 63–70.

[SK97] SHEN H., KAO D.: Uflic - a line integral convolution algorithm for visualizing unsteady flows. In *Proc. IEEE Visualization '97* (1997), Yagel R., Hagen H., (Eds.), pp. 317–323.

[SKMR98] SCHEUERMANN G., KRÜGER H., MENZEL M., ROCKWOOD A.: Visualizing non-linear vector field topology. *IEEE Transactions on Visualization and Computer Graphics 4*, 2 (1998), 109–116.

[SLM05] SHADDEN S. C., LEKIEN F., MARSDEN J. E.: Definition and properties of lagrangian coherent structures from finite-time lyapunov exponents in two-dimensional aperiodic flows. *Physica D 212* (12 2005), 271–304.

[SML98] SCHROEDER W., MARTIN K., LORENZEN B.: *The Visualization Toolkit*, 2nd ed. Prentice Hall PTR, 1998.

[SP07a] SADLO F., PEIKERT R.: Efficient visualization of lagrangian coherent structures by filtered amr ridge extraction.

[SP07b] SADLO F., PEIKERT R.: Visualizing lagrangian coherent structures and comparison to vector field topology. *IEEE Transactions on Visualization and Computer Graphics 13*, 6 (2007).

[SS96] STALLING D., STEINKE T.: *Visualization of Vector Fields in Quantum Chemistry*. Tech. rep., ZIB Preprint SC-96-01, 1996. ftp://ftp.zib.de/pub/zib-publications/reports/SC-96-01.ps.

[SS05] SALZBRUNN T., SCHEUERMANN G.: Streamline predicates as flow topology generalization. In *Topo-In-Vis 2005* (2005). (submitted).

[STH*07] SHI K., THEISEL H., HAUSER H., WEINKAUF T., MATKOVIC K., HEGE H.-C., SEIDEL H.-P.: Path line attributes - an information vi-

sualization approach to analyzing the dynamic behavior of 3d time-dependent flow fields. In *TopoInVis 07* (2007).

[STW*06] SHI K., THEISEL H., WEINKAUF T., HAUSER H., HEGE H.-C., SEIDEL H.-P.: Path line oriented topology for periodic 2D time-dependent vector fields. In *Data Visualization 2006. Proc. EuroVis '06* (2006), pp. 139–146.

[STW*07] SHI K., THEISEL H., WEINKAUF T., HAUSER H., HEGE H.-C., SEIDEL H.-P.: Extracting separation surfaces of path line oriented topology in periodic 2D time-dependent vector fields. *Journal of WSCG 15*, 1-3 (2007), 201–227.

[STW*08a] SHI K., THEISEL H., WEINKAUF T., HEGE H.-C., SEIDEL H.-P.: Finite-time transport structures of flow fields. In *Proc. IEEE Pacific Visualization Symposium* (2008), IEEE.

[STW*08b] SHI K., THEISEL H., WEINKAUF T., HEGE H.-C., SEIDEL H.-P.: Visualizing transport structures of time-dependent flow fields. *IEEE Comput. Graph. Appl. 28*, 5 (2008), 24–36.

[SWH05a] SAHNER J., WEINKAUF T., HEGE H.-C.: Galilean invariant extraction and iconic representation of vortex core lines. In *Proc. EuroVis 2005* (2005), pp. 151–160.

[SWH05b] STALLING D., WESTERHOFF M., HEGE H.-C.: Amira: A highly interactive system for visual data analysis. *The Visualization Handbook* (2005), 749–767.

[TB96] TURK G., BANKS D.: Image-guided streamline placement. In *Proc. Siggraph '96* (1996), pp. 453–460.

[The98] THEISEL H.: Visualizing the curvature of unsteady 2D flow fields. In *Proceedings 9th Eurographics Workshop on Visualization in Scientific Computing* (1998), pp. 47–56.

[The01] THEISEL H.: *CAGD and Scientific Visualization*. Habilitation Thesis, 2001.

[TS03] THEISEL H., SEIDEL H.-P.: Feature flow fields. In *Data Visualization 2003. Proc. VisSym 03* (2003), pp. 141–148.

[TSH00] TRICOCHE X., SCHEUERMANN G., HAGEN H.: A topology simplification method for 2D vector fields. In *Proc. IEEE Visualization 2000* (2000), pp. 359–366.

[TSH01] TRICOCHE X., SCHEUERMANN G., HAGEN H.: Topology-based visualization of time-dependent 2D vector fields. In *Data Visualization 2001. Proc. VisSym 01* (2001), pp. 117–126.

[Tso92] TSONIS A.: *Chaos - From Theory to Applications*. Plenum Press, 1992.

[TSW*05] THEISEL H., SAHNER J., WEINKAUF T., HEGE H.-C., SEIDEL H.-P.: Extraction of parallel vector surfaces in 3d time-dependent fields and application to vortex core line tracking. In *Proc. IEEE Visualization '05* (2005), pp. 631–638.

[TvW03] TELEA A., VAN WIJK J.: 3D IBFV: Hardware-accelerated 3D flow visualization. In *Proceedings of IEEE Visualization 2003* (Oct. 2003), van Wijk G. T. J. J., Moorhead R. J., (Eds.), IEEE Computer Society, IEEE Computer Society Press, pp. 233–240.

[TWHS03] THEISEL H., WEINKAUF T., HEGE H.-C., SEIDEL H.-P.: Saddle connectors - an approach to visualizing the topological skeleton of complex 3D vector fields. In *Proc. IEEE Visualization 2003* (2003), pp. 225–232.

[TWHS04] THEISEL H., WEINKAUF T., HEGE H.-C., SEIDEL H.-P.: Stream line and path line oriented topology for 2D time-dependent vector fields. In *Proc. IEEE Visualization 2004* (2004), pp. 321–328.

[TWHS05] THEISEL H., WEINKAUF T., HEGE H.-C., SEIDEL H.-P.: Topological methods for 2D time-dependent vector fields based on stream lines and path lines. *IEEE Transactions on Visualization and Computer Graphics 11*, 4 (2005), 383–394.

[TWSH02] TRICOCHE X., WISCHGOLL T., SCHEUERMANN G., HAGEN H.: Topology tracking for the visualization of time-dependent two-dimensional flows. *Computers & Graphics 26* (2002), 249–257.

[VKP00] VERMA V., KAO D. T., PANG A.: A flow-guided streamline seeding strategy. In *IEEE Visualization* (2000), pp. 163–170.

[vW91] VAN WIJK J.: Spot noise: Texture synthesis for data visualization. *Computer Graphics 25*, 4 (1991), 309–318.

[vW02] VAN WIJK J. J.: Image based flow visualization. *ACM Transactions on Graphics 21*, 3 (July 2002), 745–754.

[vW03] VAN WIJK J. J.: Image based flow visualization for curved surfaces. In *IEEE Visualization* (2003), Turk G., van Wijk J. J., II R. J. M., (Eds.), IEEE Computer Society, pp. 123–130.

[Wal00] WALLISCH B.: Internet-based visualization of basin boundaries for three-dimensional dynamical systems, 2000.

[WE04] WEISKOPF D., ERTL T.: GPU-based 3D texture advection for the visualization of unsteady flow fields. In *WSCG (Short Papers)* (2004), pp. 259–266.

[WEE03] WEISKOPF D., ERLEBACHER G., ERTL T.: A texture-based framework for spacetime-coherent visualization of time-dependent vector fields. In *Proc. IEEE Visualization '03* (2003), pp. 107–114.

[WEHE02] WEISKOPF D., ERLEBACHER G., HOPF M., ERTL T.: Hardware-accelerated langrangian-eulerian texture advection for 2D flow visualization. In *VMV* (2002), Greiner G., (Ed.), Aka GmbH, pp. 77–84.

[Wei98] WEICKERT J.: *Anisotropic Diffusion in Image Processing*. Teubner, 1998.

[WTS*05] WEINKAUF T., THEISEL H., SHI K., HEGE H.-C., SEIDEL H.-P.: Topological simplification of 3d vector fields by extracting higher order critical points. In *Proc. IEEE Visualization 2005* (2005), pp. 559–566.

[Yan89] YANG W.: *Handbook of Flow Visualization*. Hemisphere Publishing Corporation, 1989.

[ZBP*91] ZABUSKY N. J., BORATAV O. N., PELZ R. B., GAO M., SILVER D., COOPER S. P.: Emergence of coherent patterns of vortex stretching during reconnection: A scattering paradigm. *Phys. Rev. Lett. 67*, 18 (Oct 1991), 2469–2472.